

MODIFIED PWA 1483 NICKEL-BASED SUPERALLOY
FOR INDUSTRIAL GAS TURBINE APPLICATIONS

By

BRENDAN C. COLLINS

A DISSERTATION PRESENTED TO THE GRADUATE SCHOOL
OF THE UNIVERSITY OF FLORIDA IN PARTIAL FULFILLMENT
OF THE REQUIREMENTS FOR THE DEGREE OF
MASTER OF SCIENCE

UNIVERSITY OF FLORIDA

2007

Copyright 2007

by

Brendan C. Collins

This work is dedicated to those who came before and allowed us to stand on their shoulders, those who will follow and carry on the legacy which we have built, and especially to those who put themselves in harm's way to give the rest of us a chance to follow our dreams.

ACKNOWLEDGMENTS

First, I would like to thank Dr. Gerhard Fuchs for his support and guidance throughout this project. The obvious love he holds for his profession and the integrity which he brings to it served as inspiration, and his approachable nature made it a pleasure to come to work each day. I would also like to thank my committee members – Dr. Robert DeHoff and Dr. Paul Holloway – for their expertise and support.

I would like to acknowledge those who provided support for the work itself. This includes Dr. Allister James and Siemens Power Generation, Inc., who provided the means by which this project was completed; the fine people at Precision Cast Components Airfoils, Joliet Metallurgical Laboratories and Dirats Laboratories, who provided the casting, machining and thermal analysis of the material used for the work; Dr. Amelia Dempere and the staff at the Major Analytical Instrumentation Center at the University of Florida, who maintained the sample preparation and imaging equipment used in the analysis; and especially to my fellow research group members – Erin Sidwell, Elyssa Cutler, Brandon Wilson, Krishnaprakash Ganesan and Andrew Wasson – who not only provided assistance at various times, but who put up with me and all my opinions to a greater or lesser degree over the years.

Special thanks go to Jennifer Horton, Martha McDonald and Dr. Richard “Doc” Connell, for without their efforts, I might never have attended the University of Florida, and to Dr. Elliot Douglas, who probably still thinks I should have chosen the Polymers discipline in MSE, but whose support never wavered when I chose Metallurgy instead. Additionally, special thanks go out to my friends, who have kept me sane in spite of referees’ best efforts to do otherwise.

Finally, I would like to express my great thanks and love for my family, who always knew I could do homework, but have waited several decades to see it actually happen.

TABLE OF CONTENTS

	<u>page</u>
ACKNOWLEDGMENTS	4
LIST OF TABLES	7
LIST OF FIGURES	8
ABSTRACT	12
CHAPTER	
1 INTRODUCTION	14
Applications	14
Superalloys	17
Background	17
Strengthening	18
Composition	20
Processing	22
Candidate Alloys	24
Objective	24
2 MATERIALS AND EXPERIMENTAL PROCEDURES	25
Materials	25
Development of Heat Treatment	26
Mechanical Testing	28
Tensile Testing	30
Creep Testing	33
Characterization	39
Fracture Surface Analysis	39
Sample Cross-Section Analysis	40
3 RESULTS	44
Mechanical Testing	44
Tensile Testing	44
Creep Testing	51
Characterization	62
Fracture Surface Analysis	62
Tensile samples	63
Creep samples	70
Cross-Section Analysis	76
Optical imaging	76
SEM imaging	79

4 DISCUSSION.....	82
Casting.....	82
Mechanical Testing.....	84
Tensile Testing.....	84
Creep Testing.....	85
Characterization.....	86
Fracture Surface Analysis.....	86
Tensile samples.....	86
Creep samples.....	88
Cross-Section Analysis.....	95
Optical imaging.....	95
SEM imaging.....	100
Conclusions.....	111
Future Work.....	113
LIST OF REFERENCES.....	114
BIOGRAPHICAL SKETCH.....	118

LIST OF TABLES

<u>Table</u>	<u>page</u>
1-1. Effect of Various Alloying Additions on Ni-base Superalloys	21
1-2. Effect of Various Alloying Additions on Ni-base Superalloys.....	21
2-1. Defects found in cast alloy samples.	25
2-2. Measured Compositions of Baseline and modified samples of PWA 1483.....	26
2-3. Differential Thermal Analysis results for PWA 1483 samples.....	28
2-4. Tensile Testing Matrix.....	32
2-5. Creep Testing Matrix.....	38
3-1. Tensile Testing Results.....	44
3-2. Sequence of Creep Testing	52
3-3. Creep Testing Results.....	61
3-4. Quantitative Analysis of Features in Figure 3-15 (E).....	64
3-5. Quantitative Analysis of Features in Figure 3-22 (F).....	71
4-1. Defects found in cast alloy samples.	82
4-2. Measured Compositions of Baseline and modified samples of PWA 1483.....	83
4-3. Quantitative Analysis of Features in Figure 4-2 (B).	90

LIST OF FIGURES

<u>Figure</u>	<u>page</u>
1-1. Cross-Section of Turbofan Engine	15
1-2. GE LM2500 Gas Turbine Engine; Cross-Sectional View.....	16
1-3. Crystal Structure of A) Gamma Phase (γ) B) Gamma Prime Phase (γ').....	19
1-4. Al-Ni Phase Diagram Showing Gamma Phase and Gamma Prime Phase.....	19
1-5. Creep Damage in Turbine Blade.....	23
2-1. Microstructure of As-Received Baseline PWA 1483.....	27
2-2. Microstructure of As-Cast A) Mod I sample B) Mod II sample C) Mod III sample.....	27
2-3. Tensile/Creep Sample Design.....	29
2-4. Instron test frame with clam-shell shut and insulated for tensile test.....	30
2-5. Instron Model 2630-100 Static Extensometer with Stainless Steel Clips.....	31
2-6. Instron M3 Creep Frames with A) SF-16 2230 Power Positioning Furnace B) KSF 2-8-18 Power Positioning Furnace.....	34
2-7. Satec Model 9234 LVDT Displacement Transducer Used in Creep Testing.....	35
2-8. JEOL JSM 6400 SEM.....	39
2-9. LECO VARI/POL VP-50 Polishing Machine.....	41
2-10. LECO Neophot 21 Optical Microscope.....	42
3-1. Room Temperature Tensile Testing Results.....	45
3-2. 750°C Tensile Testing Results.....	46
3-3. 850°C Tensile Testing Results.....	47
3-4. 950°C Tensile Testing Results.....	48
3-5. Magnified Portions of Tensile Testing Curves at A) 850°C and B) 950°C.....	49
3-6. Modification II Tensile Testing Results.....	50
3-7. Modification III Tensile Testing Results.....	50

3-8. Larson-Miller Plot.....	55
3-9. 750°C Creep Testing Results for A) 831.5 MPa B) 724 MPa.....	56
3-10. Magnified Portion of Creep Testing Curves at 750°C.....	57
3-11. 850°C Creep Testing Results.....	58
3-12. Magnified Portion of Creep Testing Curves at 850°C.....	59
3-13. 950°C Creep Testing Results.....	59
3-14. Magnified Portion of Creep Testing Curves at 950°C.....	60
3-15. Fracture Surface of Tensile Sample (40-1; <i>Modification III</i>) at A) 25x B) 100x C) 500x D) 1000x E) 5000x.....	63
3-16. EDS Spectra of Sample 40-1 features: A) Carbide B) Surrounding Area.....	65
3-17. Fracture Surface of Tensile Sample (40-1; <i>Modification III</i>) at A) 25x B) 100x.....	66
3-18. Fracture Surface of Tensile Sample (40-1; <i>Modification III</i>) at A) 500x B) 1000x.....	66
3-19. Fracture Surface of Tensile Sample (40-1; <i>Modification III</i>) at 5000x.....	67
3-20. Fracture Surface of Tensile Sample (24-1; <i>Modification II</i>) at 5000x.....	68
3-21. Fracture Surface of Creep Sample (41-1; <i>Modification III</i>) at 1000x.....	69
3-22. Fracture Surface of Creep Sample (39-2; <i>Modification III</i>) at A) 25x B) 100x C) 500x D) 1000x E) 1000x F) 5000x.....	70
3-23. EDS Spectra of Sample 39-2 features: A) Carbide B) Surrounding Area.....	72
3-24. Carbide A) Morphology B) EDS Spectrum on Fracture Surface of Creep Sample (40-1; <i>Modification III</i>) at 5000x.....	74
3-25. Carbide A) Morphology B) EDS Spectrum on Fracture Surface of Creep Sample (13-1; <i>Modification I</i>) at 5000x.....	74
3-26. Fracture Surface of Creep Sample (40-2; <i>Modification III</i>) at 1000x.....	75
3-27. Casting Pores on Fracture Surface of Creep Sample (7-1; <i>Modification I</i>) at 5000x.....	76
3-28. Cross-Section of Creep Sample (7-1; <i>Modification I</i>) A) Upper Left B) Upper Right C) Lower Left D) Lower Right.....	77
3-29. Composite Cross-Section of Creep Sample (7-1; <i>Modification I</i>).....	78

3-30. Imaging Points for SEM Analysis of Cross-Section Samples.....	80
3-31. Imaging Points for Cross-Section of Creep Sample (7-1; <i>Modification I</i>) A) F B) L1 C) C1 D) R1 E) C2.....	81
4-1. Fracture Surface of Creep Sample (7-1; <i>Modification II</i>) at 1000x.	88
4-2. A) SE B) BSE Image of Carbide Cavity on Fracture Surface of Creep Sample (41-1; <i>Modification III</i>) at 5000x.....	89
4-3. <i>Stringer</i> Carbide on Surface of Creep Sample (12-1; <i>Modification II</i>) at 5000x.....	92
4-4. Script Carbide on Surface of Creep Sample (43-1; <i>Modification III</i>) at 5000x.	92
4-5. Carbide Surface Morphology for A) 750°C Creep Test (7-1; <i>Modification I</i>) B) 950°C Creep Test (26-1; <i>Modification II</i>).	93
4-6. Carbide Face Crack Morphology (43-1; <i>Modification III</i>) at A) 5000x B) 15000x.	94
4-7. Composite Cross-Section of Creep Sample (4-10A2; <i>Baseline</i>).....	96
4-8. Composite Cross-Section of Creep Sample (23-2; <i>Modification II</i>).....	97
4-9. Composite Cross-Section of Creep Sample (39-2; <i>Modification III</i>).....	97
4-10. Cross-Section of Creep Sample (39-2; <i>Modification III</i>) – Upper Left Portion.	98
4-11. Composite Cross-Section of Creep Sample (24-2; <i>Modification II</i>).....	99
4-12. Composite Cross-Section of Creep Sample (13-1; <i>Modification I</i>).....	99
4-13. Imaging Points for SEM Analysis of Cross-Section Samples.....	100
4-14. C2 Image Point of Creep Sample Cross Section (7-1; <i>Modification I</i>) at 5000x.....	102
4-15. C2 Image Point of Creep Sample Cross Section (23-2; <i>Modification II</i>) at 5000x.....	102
4-18. Cracks in Carbide Particles on Creep Sample Cross-Sections A) (7-1; <i>Modification I</i>) B) (25-2; <i>Modification II</i>).....	106
4-19. Cracks in Casting Pore on Creep Sample Cross Section (23-2; <i>Modification II</i>) at 5000x.....	107
4-20. Cracks in Casting Pore on Creep Sample Cross Section (26-1; <i>Modification II</i>) at 5000x.....	107
4-21. Partially Rafted Structure at F Image Point of Creep Sample Cross Section (4-10B2; <i>Baseline</i>) at 5000x.....	109

4-22. Partially Rafted Structure at F Image Point of Creep Sample Cross Section (26-1; <i>Modification II</i>) at 5000x.....	109
4-23. Partially Rafted Structure at F Image Point of Creep Sample Cross Section (24-2; <i>Modification II</i>) at 5000x.....	110
4-24. Structure at F Image Point of Creep Sample Cross Section (40-2; <i>Modification III</i>) at 5000x.....	110

Abstract of Thesis Presented to the Graduate School
of the University of Florida in Partial Fulfillment of the
Requirements for the Degree of Master of Science

MODIFIED PWA 1483 NICKEL-BASED SUPERALLOY
FOR INDUSTRIAL GAS TURBINE APPLICATIONS

By

Brendan C. Collins

May 2007

Chair: Gerhard E. Fuchs
Major Department: Materials Science and Engineering

For years, nickel-based superalloys have been utilized in aircraft engines and industrial gas turbines (IGT). One such alloy is PWA 1483 – an alloy with excellent castability, but lacking somewhat in mechanical properties, most importantly its creep strength. In addition, PWA 1483 was developed for IGT applications and has excellent resistance to environmental degradation. Throughout the development of nickel-based superalloys, the emphasis has been on understanding the effects of alloying additions on mechanical properties. Improvements made to IGTs in recent years to make them more efficient – in terms of both power production and emissions standards – have created a demand for alloys which would meet these needs.

The purpose of this project was to increase the strength of PWA 1483 while maintaining its castability and corrosion resistance such that it would be suitable for the demands in improved IGTs. To that end, three modifications have been made to the original composition of PWA 1483 and the resultant alloys have been studied. The modifications are as follows:

- Modification I increased γ' formers (Al, Ti, Ta) in an effort to increase γ' volume fraction and anti-phase boundary (APB) energy.
- Modification II increased the level of solid solution strengtheners (added Re and increased W) and increased the level of structural stabilizers (decreased Mo and Cr, increased Co).
- Modification III was a combination of Modifications I and II.

A heat treatment was developed in order to fully solution the cored structure which resulted from directional solidification. Once this was completed, samples were solution heat-treated, machined, and subsequently mechanically tested to determine the tensile and creep properties. Tensile testing was performed at room temperature (RT), 750°C, 850°C and 950°C and creep testing was performed at 750°C, 850°C and 950°C.

Fracture surfaces of the creep samples were analyzed by scanning electron microscopy (SEM) and cross sections along the tensile axis of the creep samples were analyzed by optical microscopy (OM) and SEM. Analysis of specimen defects from casting revealed that the Modification II and III alloys had good castability whereas the Modification I alloy did not. The Baseline PWA 1483, Modification II and III alloys had γ' with a cuboidal/rectangular shape, and the Modification I alloy exhibited spherical γ' . There were a few samples which showed that the onset of rafting of γ' had begun, but in no sample was this rafting fully developed.

The Modification I alloy outperformed the Baseline alloy in some cases during mechanical testing, but only by a slight amount. The Modification II and III alloys both outperformed the Baseline alloy by a more significant amount. Overall, it appeared that there was some synergistic effect of adding the γ' formers and concurrently adjusting the level of solid solution strengtheners/structural stabilizers, and that this effect resulted in the increase in mechanical properties. For this reason, the Modification III alloy represented the best of the three alloying methods.

CHAPTER 1 INTRODUCTION

Applications

Nickel-based superalloys are used in a wide variety of applications: heat exchangers in nuclear power plants; structural materials for solid oxide fuel cells; components in rocket motors and turbines. These turbines are mostly in the commercial flight and power generation industries, but they can also be found in military applications, which include fighter jets, helicopters, ships and even tanks. As such, a demand is placed on these materials not just from the perspective of tensile, creep and fatigue strength, but the surrounding environment presents demands as well. The varying environmental conditions create the necessity for materials which can resist degradation while still maintaining the strength characteristics demanded by the applications themselves. In particular, the advances in aircraft and industrial gas turbine (IGT) technology in recent years have driven a great deal of research for these alloys.

The turbines in such applications work in a similar fashion. The basic process and components of a turbofan engine – typically used in aeronautical applications – are illustrated in Figure 1-1 (*following page*). One point that should be made is that the nomenclature of *turbine* is often confused with that of *turbine engine*. The former is a section of the latter, which is described along with the rest of the process as follows:

An engine takes incoming air and compresses it. The compressed air is then fed into a combustor, which has nozzles for the injection of fuel. The compressed air/fuel mixture is then ignited, creating a gaseous product which is very high in stored energy and which exists at a very high temperature. These gases are directed to the blading in the actual turbine section, which convert the stored energy in the gas to rotational mechanical energy of the turbine rotor. The gases necessarily become less energetic, but not so much that it cannot be further utilized. In

aircraft engines, these gases can be fed through another set of nozzles in the exhaust of the turbine to convert even more energy to thrust, and the use of an afterburner can increase thrust even further in military applications. Clearly, increased thrust is not the goal in a stationary turbine like the IGTs used in power generation settings, but the exhaust gases can also be used for auxiliary heating applications within the power generation cycle to increase the overall efficiency of the process.

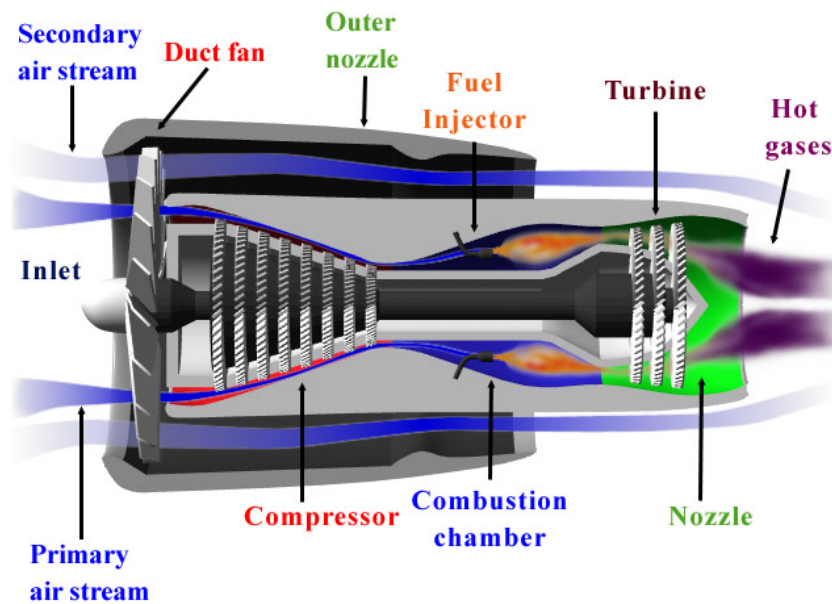


Figure 1-1. Cross-Section of Turbofan Engine [1].

The two major concerns in such a cycle from a metallurgy standpoint are:

- The size and shape of the blades, which determine the characteristics of the gas and the resulting transfer of stored energy to rotational energy, and
- The materials used, which determine the heat generation capacity within the combustor and exhaust portions of the turbine.

The demands which drive the size and shape of the blading are based upon many factors, but in general, the size of the blading in an IGT is significantly larger than that of the blading in its aeronautical counterpart. This creates conditions of higher stress which must be taken into account when designing an alloy for use in these applications.

The heat within a gas turbine – aircraft, IGT or otherwise – has been of chief concern in the development of these alloys. The critical for all gas turbines is the higher the turbine inlet temperature, the higher the efficiency. A higher inlet temperature entails a higher combustor exhaust temperature, and therein lies the problem: the tolerance of the turbine inlet temperature is based on limitations imposed by materials used in the combustor section and the blading for the turbine section. For this reason alone, superalloys represent the best material for these applications, and as the demand for higher efficiency engines continues, the need for further research of superalloys will become more and more essential [2,3]. Looking at even a short list of IGT models available and the companies which provide them illustrates just how essential this research is from a financial point of view:

- Siemens SGT-600/700/800
- Rolls Royce 501/RB211/Trent 60
- Pratt & Whitney FT8/ST6/ST18/ST40
- GE LM1600/LM2000/LM2500/LM6000/LMS100[®]

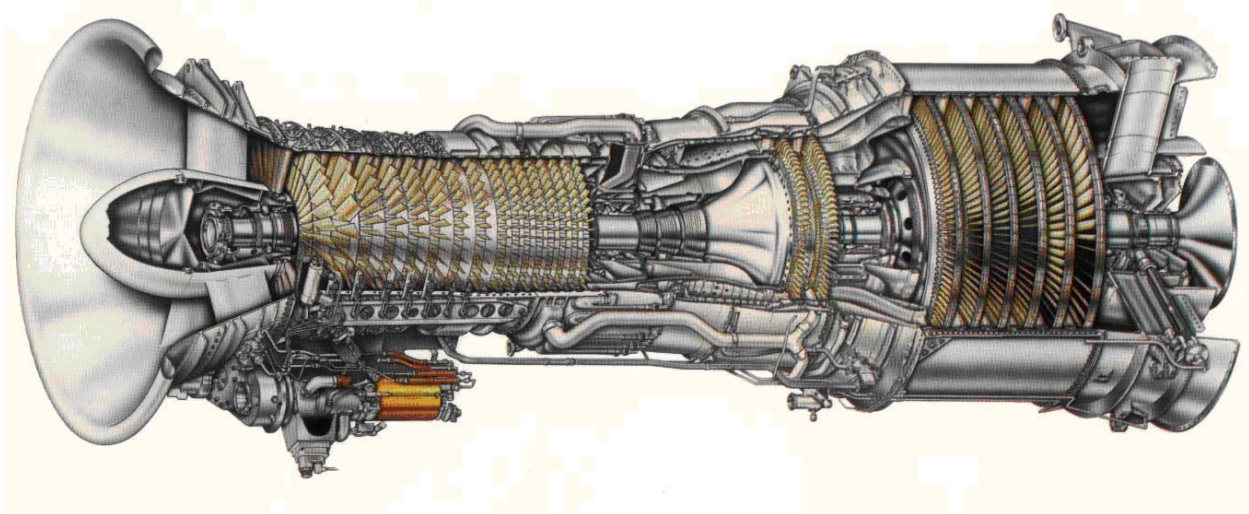


Figure 1-2. GE LM2500 Gas Turbine Engine; Cross-Sectional View [4].

But the increase in temperature is but one issue driving the need for superalloy research. While the demand for power generation technology is certainly high, it pales in comparison to the attention that these multi-billion dollar companies are giving to the ‘green engineering’ aspect of these turbines. The need for, development and implementation of regulations on emissions from these turbines has resulted in a reformation of sorts within the industry, and as a result, research has been done in search of new fuels which can be used in these turbines [5,6,7]. From an environmental standpoint alone, this dictates that alloys will have to be developed which can continue to resist degradation under the harsh conditions of the combustion of these new fuels. In addition, mechanical advances are being made as well, changing the designed stress conditions the components in the turbines will have to endure. For these reasons, the IGT inlet temperature and blade operating temperatures – as well as strength requirements – will begin to approach those seen in aircraft engines.

Superalloys

Background

The use of superalloys is dictated primarily by the high-temperature nature of the application. Usually, high-temperature is defined from an aspect of the material, rather than that of the application itself. For this reason, the fraction of the melting temperature (T_m) – also known as the homologous temperature – of such alloys is used. Superalloys are those which operate in excess of $0.5T_m$, and often in environments approaching $0.9T_m$. The temperatures in the exhaust of the combustor section and the inlet of the turbine section can approach 1400°C , which represents $0.96 T_m$ of pure Ni, and $0.84 T_m$ of pure Ti. Alloying additions usually lead to a decrease in the T_m of these materials, and as such, material selection constitutes only a part of the solution to the problem of heat in the engine.

Other solutions to limit material temperature have been developed, such as internal cooling channels which are created directly into the blade as it is cast. Air from the secondary air stream seen in Figure 1-1 previously – also known as bypassed air – is passed through these cooling channels. This air is at a significantly lower temperature than the gases surrounding the blade, and as such, it cools the blade as it passes through. Another technology used to maintain the blades at lower temperatures is the use of various ceramic coatings, which provide a thermal barrier between the hot gases and the blade material. Often, both technologies are used, but the end result is that the cost of the blades goes up. Engineering around issues arising from the complexity of the cooling channels and the continual issues of quality control and cost of thermal spray processes both lead to this increased overall cost. This only further emphasizes the importance of developing an alloy which might be able to withstand such temperatures without needing these alternate cooling methods.

Strengthening

The ability of these alloys to resist deformation under such extreme conditions of stress and temperature is due to their microstructure, which is a product of their constituents and processing. In this project, the most significant of these microstructural features are [8]:

- The gamma phase (γ): any number of elements partition to this phase, but it is primarily composed of Ni, Cr, Mo, Co, W and Re in a solid-solution, face-centered cubic (fcc) structure, shown in Figure 1-3 (A) (*following page*).
- The gamma prime phase (γ'): some elements also partition to this phase, but it is considered to be strictly Ni_3Al in an ordered fcc structure, shown in Figure 1-3 (B) (*following page*). Ti and Ta also readily substitute for Al to form this phase with Ni.
- Carbides: these can take on many forms, both morphologically- and compositionally-speaking. The most common is the MC carbide (where M represents a metallic element atom), which can appear in blocky, nodular or script morphologies. The MC carbides form at temperatures between the liquidus and solvus of the alloy. At higher carbon levels, higher temperatures and long exposure times, these can decompose to M_{23}C_6 or M_6C carbides, often called *secondary carbides*.

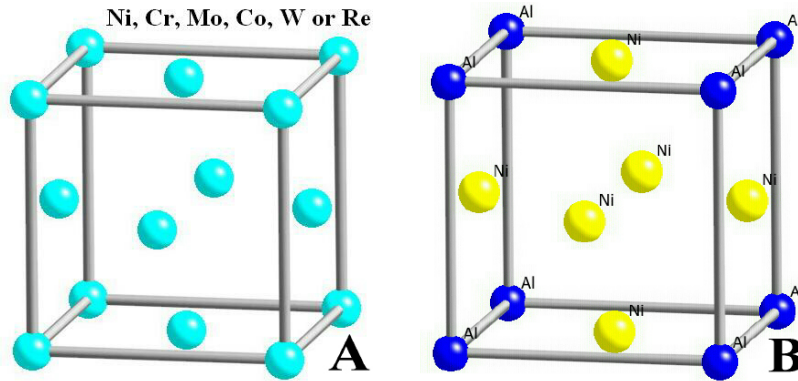


Figure 1-3. Crystal Structure of A) Gamma Phase (γ) B) Gamma Prime Phase (γ') [9].

One very important fact should be noted here: these γ and γ' phases exist over a range of compositions. This might seem obvious for the γ phase, but the same is true for the γ' phase, shown in Figure 1-4 (*below*) in orange and blue (respectively):

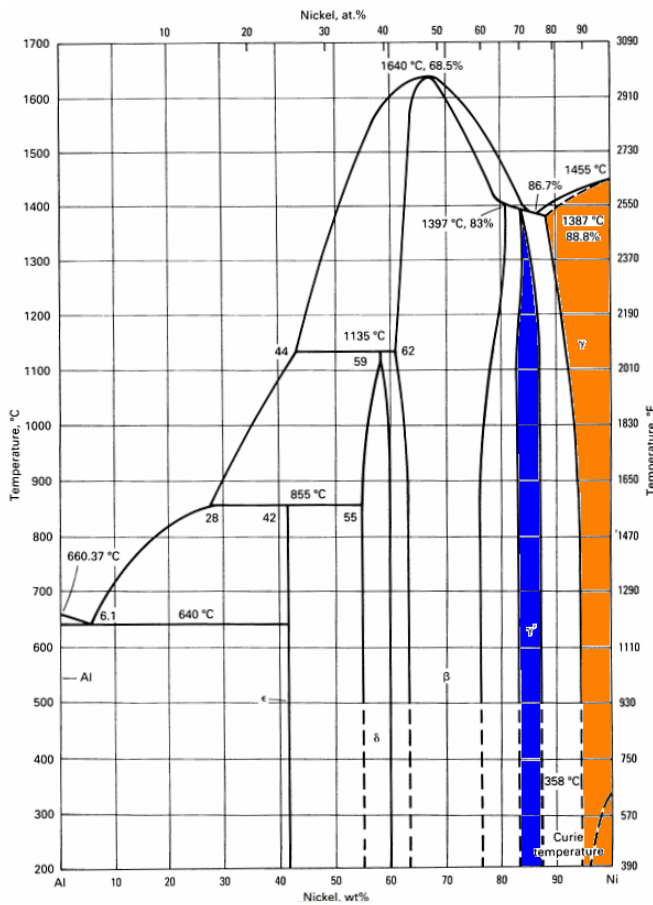


Figure 1-4. Al-Ni Phase Diagram Showing Gamma Phase (orange) and Gamma Prime Phase (blue) [10].

The importance of each of these features from a strengthening standpoint depends largely upon the conditions to which they are subjected. Usually, the most important strengthening mechanism is attributed to that which arises from the slight structural difference between the γ and γ' phases, i.e.: long range order and lattice misfit. Dislocations move through γ' precipitates in pairs, called *superdislocations*. The energy required for the superdislocation to pass through a γ' precipitate is called the *anti-phase boundary (APB) energy*, and it is a direct result of the differing slip systems between the two phases [11]. Alloying can raise or lower this energy by changing the structure of the γ or γ' , thus affecting the APB and raising or lowering the strength of the material. In any case, the ordered γ' particles usually make up anywhere from 50% to 70% volume fraction of the material, and they are coherent with the surrounding matrix.

This discussion represents only the most fundamental principles of strengthening in such alloys. For a more detailed description, there are many references available, either on the web [8,9] or in print [11,12,13].

Composition

From the previous discussion of strengthening, it follows that slight changes in the composition of these alloys dictate microstructural changes, which then affect the mechanical properties of these alloys. While this certainly follows standard theory in any materials science discipline, it makes the problem no less complicated. In the case of these alloys, no fewer than 21 elements have been added, 12 of which are almost always added in varying amounts. The complexity of the problem does add to the value of computational models, such as ThermoCalc and JMatPro software, but these would be useless without a growing supply of information which can be added to their respective databases.

In any case, there has been enough alloy development to give a wide range of existing alloys from which to choose, even if the goal is to design a completely new alloy. The process is

simple enough: an alloy which seems to have properties close to the desired properties of the new alloy is chosen, the composition is adjusted slightly, the resulting material is produced and tested, and finally, the results are analyzed to establish the effect of the compositional change. Such was exactly the methodology used in this study.

In order to make effective changes to the composition of the alloy, it is important to rely on the published literature on general alloying addition trends in superalloys. Such information for Ni-base superalloys has been developed for years, as summarized in Tables 1-1 and 1-2 (*below*):

Table 1-1. Effect of Various Alloying Additions on Ni-base Superalloys [12].

Phase relation/property	Effect
Solid solution strengthening of γ	W, Mo, Ti, Al, Cr strengthen Fe, Co, Cu strengthen slightly
Solid solution strengthening of γ'	Mo, W, Si, Ti, Cr strengthen Mn, Fe, Cu strengthen slightly V, Co weaken
γ' volume fraction	Cr, Ti, Al, Nb, Mo, Co, Ta, V, Fe increase
APB energy	Ti, Co, Mo, Fe increase Al, Cr decrease
$\gamma - \gamma'$ misfit	Ta, Nb, C, Ti increase Cr, Mo, W, Cu, Mn, Si, V decrease Al, Fe, Co negligible effect
Coarsening rate of γ'	Ti, Mo, Nb, Co, Fe decrease Cr increases Zr, B no effect
Oxidation and hot corrosion resistance	Cr improves Other elements variable

Table 1-2. Effect of Various Alloying Additions on Ni-base Superalloys [14].

Effect	Addition to Nickel-base Superalloy
Solid-solution strengtheners	Co, Cr, Fe, Mo, W, Ta, Re
Forms MC carbides	W, Ta, Ti, Mo, Nb, Hf
Forms $M_{23}C_6$ carbides	Cr, Mo, W
Forms M_6C carbides	Mo, W, Nb
Forms $\gamma' Ni_3(Al, Ti)$	Al, Ti
Raises solvus temperature of γ'	Co
Hardening precipitates and/or intermetallics	Al, Ti, Nb
Oxidation resistance	Al, Cr, Y, La, Ce
Improves creep properties	B, Ta
Retard γ' coarsening	Re

These are obviously only two examples of such information, and more are developed and presented in nearly every paper published in the literature [15,16,17]. All this information is taken into account when deciding what changes should be made to the existing alloy composition, and care should be taken to properly balance the changes such that a detrimental side effect does not occur with the desired effect.

An example of this would be raising the level of Cr in the alloy. This would possibly raise the oxidation and hot corrosion resistance of the alloy, but at the same time, it would result in a higher γ' coarsening rate. Depending on the conditions dictated by the application for which the alloy is being developed, the higher γ' coarsening rate might be above tolerable limits, and would therefore render the compositional change useless. Or, the Cr content could be raised, but to offset the increased γ' coarsening rate effect, an increase in Re would have to be made as well.

Processing

The final variable to be taken into account for this study goes back to the discussion of critical issues within the turbine engine itself, specifically to the issue of the size and shape of the turbine blades. It was noted previously that the size of the blading in an IGT is significantly larger than that of the blading in its aeronautical counterpart and that this results in higher stresses within the blade. The problem of stress is not the only problem resulting from the size of these blades, but it is an important one, to be sure.

Addressing this problem has driven several advances within the field. At first, the development of superalloys focused on methods to make polycrystalline superalloys more creep resistant. This resulted in many advancements, most notably the addition of grain boundary strengtheners (C, B, Zr) [18]. The process of directional solidification was then developed. This process not only significantly reduced the number of grains, but also grew them in a columnar orientation such that the boundaries would be parallel to the stress axis, thereby greatly

increasing the creep and thermal-mechanical fatigue (TMF) resistance of the blade. As illustrated in Figure 1-5 (*below*), creep progresses in a direction perpendicular to the stress axis. Finally, the process of growing single crystal blades was developed. This process – as the name would suggest – produces a single grain, which can be oriented in a manner to minimize the effects of creep. These single crystal alloys represent the best the industry currently has to offer where strength is concerned. For that reason, the applications which are most demanding in terms of temperature and stress usually employ single crystal alloys, and as the demands within the IGT increase, these alloys will be of more and more interest.

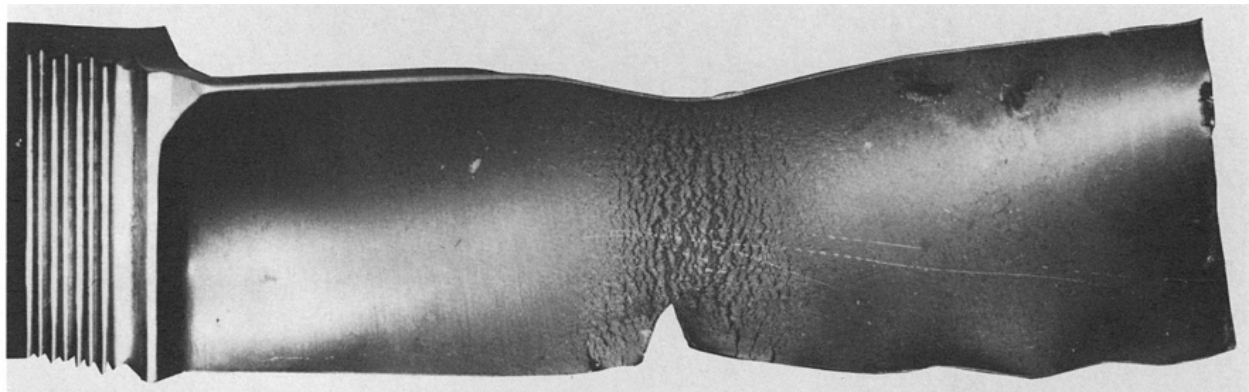


Figure 1-5. Creep Damage in Turbine Blade [19].

The problem, however, is that while the process of producing single crystals is moderately efficient for smaller blades, the same does not hold true for the larger blades seen in IGT applications. The issue is one of control – specifically, controlling the thermal gradient at the solid-liquid interface during solidification [20,21]. For the smaller blades (5 – 15 cm) used in aeronautical applications, achieving this control is not a problem. But for the larger blades in IGT applications (50+ cm), controlling this gradient has proven more difficult, and issues of defects have been a significant problem. The addition of small amounts of C to the alloy has been reported to reduce the number of casting defects [22], but the influence of the resultant carbides on mechanical properties is not well understood and is the subject of current studies.

Candidate Alloys

The two alloys which show the most promise for the advanced IGT applications are CMSX-4 and PWA 1483, but for contrasting reasons. CMSX-4 is a higher-strength, second-generation single crystal alloy which seems suitable for the application, but has a low hot corrosion resistance and somewhat limited castability, both of which must be improved first. PWA 1483 is a first-generation single crystal alloy which already has excellent hot corrosion resistance and excellent castability, but before it can be used in the desired role, its strength must be improved. The choice, then, is whether it is best to approach the problem from a strength perspective or a hot corrosion resistance perspective.

There are two reasons why the latter makes more sense. First, alloying to change properties is a complicated process, and it is always best to make changes to elements whose effects are better understood. There has been much more work done to understand the effect of alloying additions on the strength of these materials, and as such, making changes to the composition to improve the hot corrosion resistance of CMSX-4 would be based upon less data. Second, programs have already been established to study the problem from that perspective on CMSX-4 with only limited success. Further study of CMSX-4 would seem to be of little value, so it only makes sense to broaden the research from a global perspective instead.

Objective

The purpose of this project was to modify the composition of PWA 1483 Ni-based, single crystal superalloy in an attempt to develop a stronger alloy while maintaining the characteristics of high resistance to hot corrosion and good castability. Three modifications were made. Solution heat treatments were developed, and these modified alloys were tested to determine tensile and creep properties, and then analyzed using optical and scanning electron microscopy techniques to characterize the microstructural effects of the alloying changes.

CHAPTER 2
MATERIALS AND EXPERIMENTAL PROCEDURES

Materials

The materials for all samples were provided by and were cast into single-crystal bars at Precision Cast Components Airfoils (PCC Airfoils, Minerva, OH). A commercial directional solidification (DS) furnace was used with high gradient investment casting techniques used to develop a [001] orientation in the alloys. A helical-type grain selector was used to produce the single crystal samples. The withdrawal rate was initially set at 15 cm per hour until the grain selector was reached, at which point the rate was changed to 20 cm per hour. The bars were cast as cylinders with a diameter of 1.25 cm and a length of 20 cm. One mold was processed for each modification (I, II, III), and each mold contained fifteen bars and one blade. After casting, the [001] orientation was verified by Laue backscattered x-ray technique to identify multi-grain boundaries, slivers and low-angle grain boundaries. These are types of defects which would result in rejected castings in production of single crystal components. Any incidence of multiple grains, sliver defects on the surface of the casting, or grain boundaries misoriented greater than 10° are considered failing. The results of this analysis are shown in Table 2-1 (*below*):

Table 2-1. Defects found in cast alloy samples*.

Alloy	Multi-grain	Sliver	Low-Angle Grain Boundary
Modification I	15 (3 usable)	0	0
Modification II	0	4 (4 usable)	0
Modification III	0	2 (2 usable)	2 (2 usable)
Modification I blade	Yes	No	No
Modification II blade	Yes	No	No
Modification III blade	No	No	Yes (<i>start</i>)

*The color coding used for all data tables throughout this document shall be color coded as follows:

- Baseline = dark red
- Modification II = blue
- Modification I = green
- Modification III = orange

The Baseline samples were provided by Siemens Power Generation, Inc., but in a vacuum heat-treated condition. This heat treatment entails a relatively short soak from 0.5 – 2 hours between 1200°C and 1300°C.

The compositions chosen for the modifications were based upon the following principles:

- Modification I increased γ' formers (Al, Ti, Ta) in an effort to increase γ' volume fraction and anti-phase boundary (APB) energy.
- Modification II increased the level of solid solution strengtheners (added Re and increased W) and increased the level of structural stabilizers (decreased Mo and Cr, increased Co).
- Modification III is a combination of the alloying schemes in Modifications I and II.

The specific levels chosen to accomplish these are shown in Table 2-2 (*below*):

Table 2-2. Measured Compositions of Baseline and modified samples of PWA 1483*.

Alloy	Ni	Cr	Co	Mo	W	Re	Ta	Al	Ti	C
Baseline	Bal.	12.8	9.0	1.9	3.8	0.0	4.0	3.6	4.0	0.07
Mod I	Bal.	12.5	9.0	1.9	3.8	0.0	6.2	4.6	2.5	0.07
Mod II	Bal.	10.0	12.0	0.6	4.9	3.0	3.9	3.5	3.9	0.07
Mod III	Bal.	10.0	12.0	0.6	4.9	3.0	6.0	4.5	2.4	0.07

*Elements with adjusted levels from Baseline are shown in bold. All values in weight %.

The 0.07 wt. % C addition to all samples is for the reduction of the number of casting defects.

Because of the relatively low refractory metal content – consistent within most first-generation superalloys – the alloy is already relatively castable, but the C addition was maintained in the hope that it would minimize defects from the addition of Re and increased levels of W and Ta, and to minimize the number of variables evaluated. The high levels of Cr are maintained in an effort to maintain corrosion resistance.

Development of Heat Treatment

All work discussed here which was performed in the development of the heat treatment was completed by Leonard J. Grant and Erin A. Sidwell, as previously unpublished research. It

is discussed here to provide a timeline of this project, as well as to provide the information necessary to describe the condition of the samples that were tested mechanically. The discussion here reflects only the major steps of the work done, rather than the details of the entire process.

PWA 1483 was chosen because of its relatively good castability and its excellent resistance to environmental degradation. Because of its low refractory composition, solution heat treatments usually are significantly shorter than those of second- and third-generation superalloys. When the decision was made to add these elements in an effort to strengthen the alloy, it was understood that this would also likely increase the solution heat treatment time, and thus, a new heat treatment schedule would have to be developed. The segregation in the as-received (heat-treated) Baseline sample can be seen in Figure 2-1 (*below*) and in the as-cast Modification samples in Figures 2-2 (A-C) (*below; all images from L.J. Grant*):

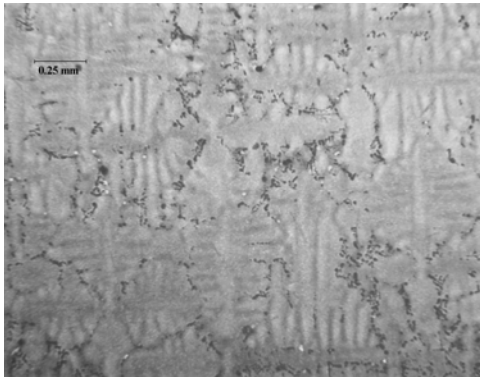


Figure 2-1. Microstructure of As-Received Baseline PWA 1483.

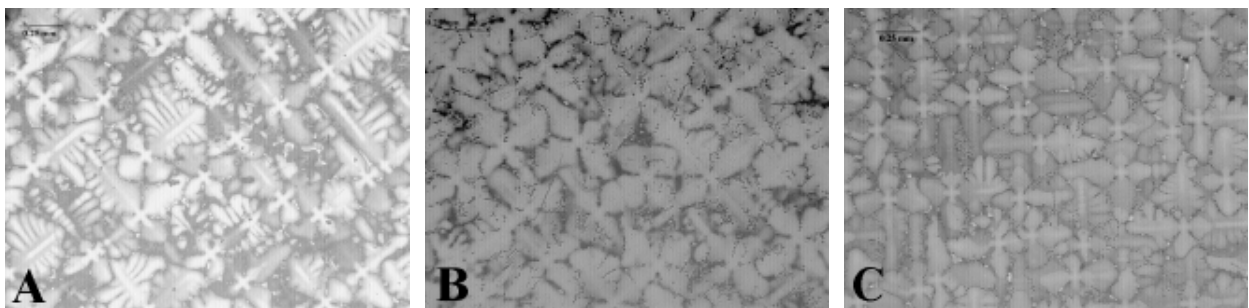


Figure 2-2. Microstructure of As-Cast A) Mod I sample B) Mod II sample C) Mod III sample.

Grant and Sidwell [23] developed a solution heat treatment which was nearly 100% effective: 5 hours at 1250°C, followed by 5 hours at 1265°C, and included a simulated coating cycle of 4 hours at 1080°C – all under vacuum. Some very small traces of eutectic remained in Modification III only, but it was thought that it would not be enough to significantly affect the properties measured in testing, and not enough to merit postponing mechanical testing. The work was based on differential thermal analysis (DTA) of the Baseline and all three modifications in a heat-treated condition, the results of which are shown in Table 2-3 (*below*):

Table 2-3. Differential Thermal Analysis results for PWA 1483 samples*.

Alloy	Solidus Temperature	γ' Solvus temperature	Liquidus Temperature
Baseline	1282	1220	1332
Mod I	1280	1220	1361
Mod II	1287	1220	1341
Mod III	1287	1220	1364

*All temperatures in °C.

Once developed, the heat treatment was performed on 4 bars of Baseline alloy, 3 bars of Modification I alloy, 7 bars of Modification II alloy and 7 bars of Modification III alloy. These bars were chosen for heat treatment and testing since they were acceptable for mechanical testing based on original casting defect analysis.

Mechanical Testing

The bars which had been solution heat treated were sent to Joliet Metallurgical Laboratories, Inc. (Joliet, IL) for machining, using low-stress grinding techniques. Thirty-four samples were machined according to Figure 2-3 (*following page*), with the following dimensions: gauge section 4.5 mm (0.177 in) in diameter and 26.0 mm (1.025 in) in length. Holes were drilled in the shoulder of the samples, so the extensometer frame could be attached to

the sample via mounting screws. These holes are shown in the 3D rendition of the sample in Figure 2-3 (below):

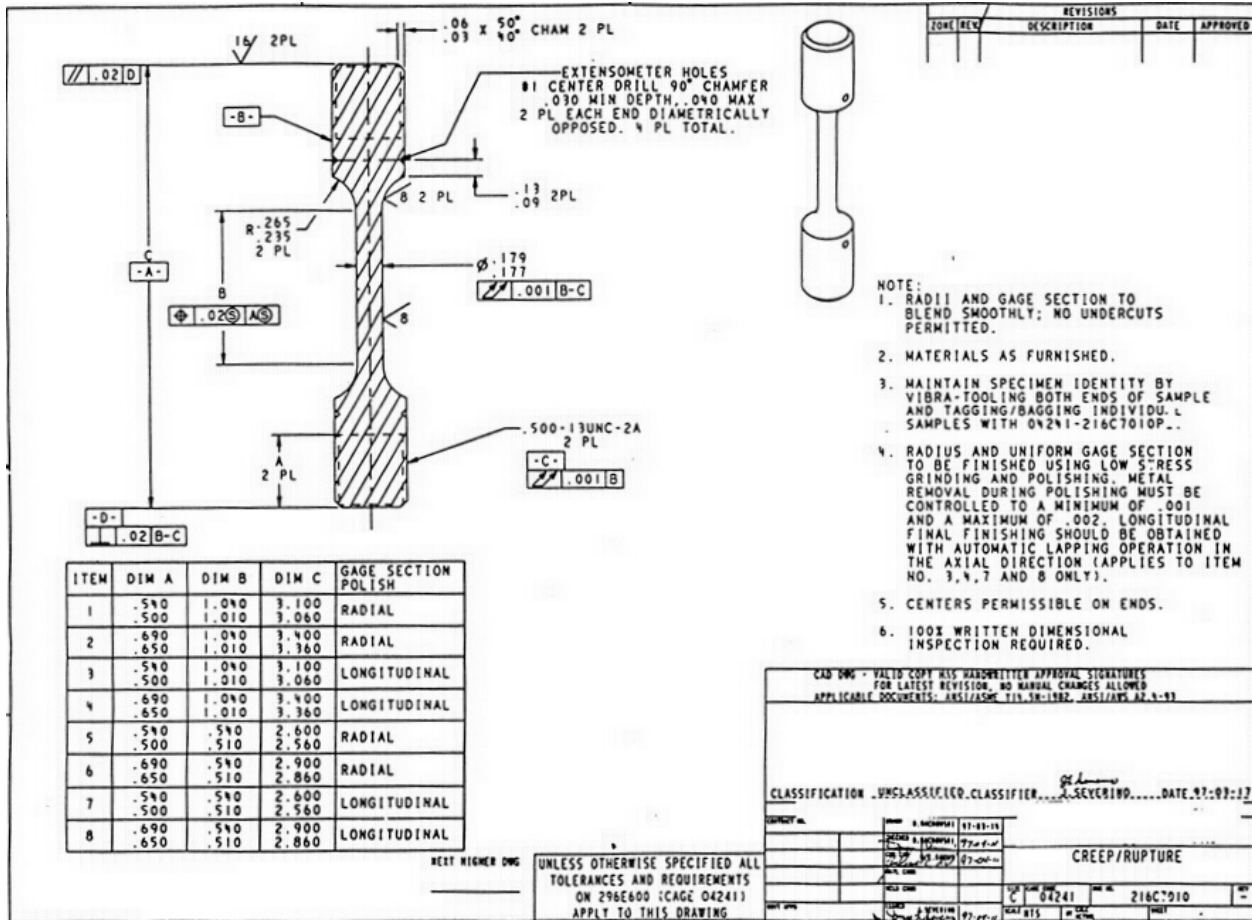


Figure 2-3. Tensile/Creep Sample Design. All dimensions shown are in inches.

Another 8 samples were machined from the Baseline sample bars, with the only deviation from the design in Figure 2-3 being shoulder diameter, which was 0.9525 cm (0.375 in) rather than the 1.27 cm (0.500 in) called for. Of the 34 samples, 28 were used for testing – 23 successfully. Two tests proved to be unsuccessful due to erroneous data collected by the extensometer and its associated software. Most likely, this was caused by the extensometer frame slipping on the sample as a test was in progress. Two others were unsuccessful because the data was lost. One test was unsuccessful as a result of damage to the sample threads caused

by using improperly-sized grips. Of the 23 samples successfully used, 14 were used for creep testing and 9 were used in tensile testing.

Tensile Testing

Tensile testing was performed using an Instron Model TC 25 servo-hydraulic frame in the High Temperature Alloys Laboratory at the University of Florida, shown in Figure 2-4 (*below*):



Figure 2-4. Instron test frame with clam-shell shut and insulated for tensile test.

The frame has an actuator with six inches of travel and is capable of loads up to 9500 Kg (21000 lbs). The frame is attached to an Instron Fast Track 8800 computer, which is then attached to a desktop computer. An integral Satec Model SF-12 2230 clam-shell Power Positioning Furnace with Kanthal elements was used to heat the samples. Two type K

thermocouples with Nextel sheathing were tied to the gauge section of the sample with 26 AWG 80Ni-20Cr wire. One of these was attached to an Instron TCS1000 controller, which provided precise control and monitoring of temperature from heatup to the completion of the test. The second thermocouple was connected to an independent hand-held unit which was used to verify temperatures on the Instron controller unit.

The sample was fixed into the extensometer frame by means of two pairs of 6.4 mm (0.25 in) diameter knife-edge inserts. The extensometer frame and inserts were fabricated from Haynes 214 alloy. An Instron model 2630-100 static extensometer – shown in Figure 2-5 (*below*) – with a 25.4 mm (1.0 in) gauge length and 25.4 mm (1.0 in) of travel was used for measuring strain, and attached to the sample by means of two 6.4 mm (0.25 in) stainless steel clips (also shown in Figure 2-5). Once the sample was fixed into the extensometer frame and loaded into the testing frame with the thermocouples attached, the test was commenced.

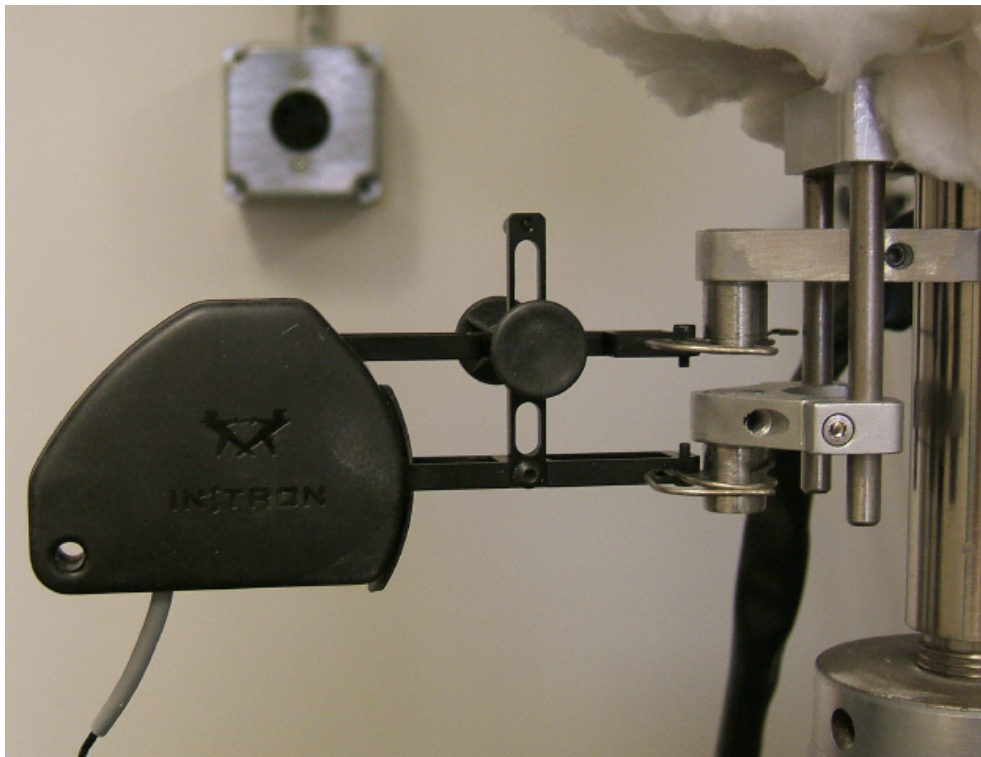


Figure 2-5. Instron Model 2630-100 Static Extensometer with Stainless Steel Clips.

For room temperature tests, the clam-shell was not used since no heating was required. Thus, the extensometer frame was not required, since the extensometer could be attached directly to the sample. For all other tests, once the sample was mounted, the clam shell was closed and heatup was commenced. Once the sample reached the test temperature, a 15-minute soak was used to ensure thermal equilibrium was achieved prior to commencing the test.

The testing was conducted using the Merlin module of the Fast Track software on the desktop computer. The Merlin software recorded the data from the extensometer which was then exported as raw data and imported into an Excel file from which key properties could be assessed – specifically: yield strength (YS), ultimate tensile strength (UTS), Young’s modulus (E) and total elongation. A standard 0.2% offset was used for the determination of the YS, and the UTS was determined from utilizing the MAX function in Excel on the column of measured stress values. All tensile testing was conducted at an initial strain rate of 2.5 mm/min (0.1 in/min). The tensile testing matrix is shown in Table 2-4 (*below*).

Table 2-4. Tensile Testing Matrix*.

Bar ID	Alloy	Sample ID	Temperature
7	Mod I	7-2	RT
28	Mod II	28-2	RT
37	Mod III	37-1	RT
22	Mod II	22-2	750
40	Mod III	40-1	750
24	Mod II	24-1	850
39	Mod III	39-1	850
25	Mod II	25-1	950
37	Mod III	37-2	950

*All temperatures in °C.

The limited availability of Baseline and Modification I samples did not allow for testing samples at all test conditions. Therefore, no tensile testing on the Baseline samples, and only one tensile test was performed on the Modification I samples at first. The following reasons explain that choice:

- Tensile data for the Baseline PWA 1483 could be estimated (if not gleaned directly) from published literature, therefore testing would be for verification only.
- The emphasis of this research is on creep properties, driven by the industrial gas turbine application for which it is designed. As such, it was more important to conduct creep testing on these alloys, and use of samples was prioritized accordingly.
- Once creep testing was successfully completed, if data warranted further tensile testing on the Baseline and/or Modification I samples, it would be performed on any remaining samples at that time.

The reasoning behind the temperatures chosen for the tensile testing is discussed in the next section.

Creep Testing

Creep testing was performed using Satec Model M3 creep frames shown in Figure 2-6 (*following page*). A total of four frames are located in the High Temperature Alloys Laboratory at the University of Florida, and three of the four were used for the testing. Two frames – like the one shown in Figure 2-6 (a) – are fitted with Satec Model SF-16 2230 Power Positioning Furnaces. These furnaces have three different hot zones (top, middle and bottom) of independently-controlled Kanthal heating elements. This allows more precise control of heat input, providing a more even heating of the entire gauge section of the sample being tested. The other two frames – like the one shown in Figure 2-6 (b) – are fitted with Satec Model KSF 2-8-18 Power Positioning Furnaces. These furnaces have a single hot zone, and utilize MoSi₂ heating elements which are capable of testing temperatures up to 1500°C (2732°F).



Figure 2-6. Instron M3 Creep Frames with A) SF-16 2230 Power Positioning Furnace B) KSF 2-8-18 Power Positioning Furnace..

All of the furnaces on the creep frames were controlled by NuVision Mentor software supplied by Satec, which is installed on an attached standard desktop computer. Three type K thermocouples were attached to the gauge section of each sample being tested using 26 AWG 80Ni-Cr wire. The thermocouples were evenly-spaced, and were approximately 1 cm (0.39 in) apart, all on the same side of the sample opposite the extensometer. This arrangement served to provide good indication of temperature in all three zones along the gauge length, as well as to keep the thermocouple wires away from the extensometer itself. In some cases, the Mentor software had a difficult time controlling temperature with all three thermocouples giving input. In these cases and at all times for the creep frames with single hot zones, only one thermocouple was used to control temperature, while the other two were monitored to verify the temperature in

the other two zones manually. Once this adjustment was made, no further problems were noted, and all zones were well within the 5°C differential set as the limit to conduct the test.

An extensometer frame similar to the one used in tensile testing was used. There are only three significant differences between them, as follows:

- Their length, which is due to the size of the furnace on each type of frame. The larger-sized creep furnaces require longer extensometer frame arms than those required by the smaller clam-shell furnace on the tensile unit.
- The manner in which the sample is mounted in the extensometer frame. For the creep tests, the samples were held in place by using screws which engaged the holes machined into the shoulders of the samples (as discussed and shown previously in Figure 2-3), whereas knife-edges were used for the frames in the tensile tests.
- The type of strain-measurement device used. The clip-type design used for tensile testing was shown previously in Figure 2-5, and the threaded-type design used for creep testing is shown in Figure 2-7 (*below*):

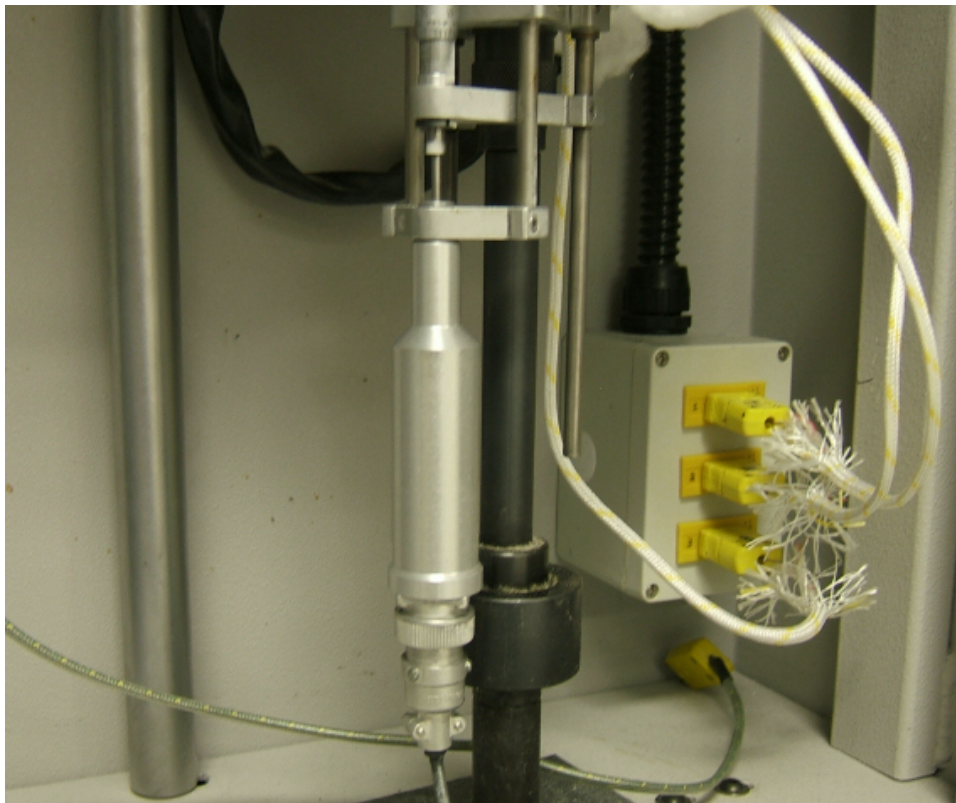


Figure 2-7. Satec Model 9234 LVDT Used in Creep Testing.

Once the sample was fixed into the extensometer frame and loaded into the testing frame with the thermocouples attached, heatup of the sample was commenced. Once the sample was within 3°C of testing temperature, an automatic soak was imposed as was programmed into the Mentor software. In cases where all three thermocouples were used to control power input, an additional 5°C differential limit was imposed prior to commencing the soak as well. Upon completion of the soak – meaning one continuous hour without exceeding the temperature differentials listed previously – the LVDT was zeroed. The sample was then loaded in steps, which allowed the Mentor software to calculate the Young’s modulus for the sample. This – along with the data gathered by the software during the test – was exported as raw data and then imported into an Excel file from which key properties could be assessed – specifically: time to 0.1% creep, time to 0.2% creep, creep rupture life, minimum creep rate and total elongation. These values could be calculated by the Mentor software, but the use of Excel offered more detailed analysis. In addition, use of Excel allowed the opportunity to plot both the standard creep curves as well as Larson-Miller time-temperature parameter graphs.

The testing matrix for the creep samples was based on the available creep data for PWA 1483. Unfortunately, since PWA 1483 is a proprietary alloy developed by Pratt & Whitney years ago, detailed creep data were extremely limited in quantity. This made it difficult to fully develop a test matrix, but it was decided to do the testing in sequential steps, with only the first step based upon the available data. Conditions for subsequent steps would be determined in a method similar to that described below, using data from previous steps to refine the required conditions. The details of how each step progressed are discussed in Chapter 3.

The available data were used to calculate Larson-Miller parameters (LMP) which could be used to reverse-engineer the desired testing conditions. To do this, the calculated LMP data was

used to develop a Larson-Miller plot, and from that, a logarithmic regression was performed to derive an initial LMP equation. The standard Larson-Miller equation is:

$$LMP = T(\text{LOG}t_f + 20)$$

where T is the temperature (in Kelvins) and t_f is the time to failure (in hours), but the standard plot utilizes a scaled-down version of this equation, so the following equation was used:

$$LMP_{plot} = \frac{T(\text{LOG}t_f + 20)}{1000}$$

The initial LMP equation derived from the available data was as follows:

$$\sigma = \text{LOG}^{-1}[-2.8732 \cdot \ln(LMP) + 11.887]$$

where σ is the stress used in the creep test. Substitution of the previous LMP_{plot} equation for LMP resulted in the following equation:

$$\sigma = \text{LOG}^{-1}\left[-2.8732 \cdot \ln\left(\frac{T(\text{LOG}t_f + 20)}{1000}\right) + 11.887\right]$$

Use of this equation indicated that at a desired time to failure of 144 hours, the required stress would be 831.5 MPa (120.6 Ksi) at 750°C. The Mentor software automatically converted the stress to load, using the dimensions of each sample, which were input manually prior to the test, and all four creep frames utilize a lever-arm with a 16:1 ratio between applied load on the sample and actual weights required on the machine. The arm and weights are visible in Figure 2-6 (a-b).

As described earlier, problems with the Mentor control software led to three tests having to be stopped and restarted due to the inability of the software to reach the proper conditions to even complete the one-hour soak. In all three cases, a similar pattern was observed. At first, the zones would control properly during the heatup process, taking the sample to the proper temperature. The soak would begin, but immediately, a drop in the temperatures of all three

zones was observed, and for some reason, the rate seemed to be too low for the Mentor software to compensate. When the temperatures reached a 50°C differential from the programmed test temperature, the Mentor software did take the appropriate action and was shut down. One case was exacerbated by a failed heating element, which was replaced. As mentioned previously, it was in these three cases where only one thermocouple was used to control temperature, and the other two were used as a manual verification method. Once this was done, all three tests were completed with no further issues.

The complete creep testing matrix is shown in Table 2-5 (*below*).

Table 2-5. Creep Testing Matrix*.

Bar ID	Alloy	Sample ID	Temperature	Stress
4-10A	Baseline	4-10A2	750	831.5
7	Mod I	7-1	750	831.5
23	Mod II	23-2	750	831.5
39	Mod III	39-2	750	831.5
25	Mod II	25-2	750	724
41	Mod III	41-1	750	724
4-10A	Baseline	4-10A1	850	448.9
12	Mod I	12-1	850	448.9
24	Mod II	24-2	850	448.9
40	Mod III	40-2	850	448.9
4-10B	Baseline	4-10B2	950	344.5
13	Mod I	13-1	950	344.5
26	Mod II	26-1	950	344.5
43	Mod III	43-1	950	344.5

*All temperatures in °C; all stresses in MPa; samples with control problems in bold.

Characterization

After completing mechanical testing, the samples were analyzed to correlate microstructural features with the results developed in testing. The samples usually failed slightly off-center from end-to-end, and the ‘short’ piece was used in the first type of analysis described, while the second piece was used for further characterization, discussed subsequently.

Fracture Surface Analysis

Fracture surfaces of all samples used in tensile and creep rupture testing were evaluated. Prior to observation, each sample was cleaned in a LECO ultrasonic bath with acetone and dried with compressed air to remove any particulate matter. The samples were then put in a plastic container with individual compartments for each sample. This ensured the fracture surfaces remained free of damage which could have been sustained in transport to and from the imaging systems. Just prior to actual observation, each sample was cleaned again using compressed air.

Each sample was then placed into a JEOL JSM 6400 Scanning Electron Microscope (SEM) – shown in Figure 2-8 (*below*) – for analysis.



Figure 2-8. JEOL JSM 6400 SEM.

The SEM being used had a standard desktop PC attached, and the Link ISIS software package from Oxford Instruments was utilized to take images and energy dispersive spectrometry (EDS) spectra, as well as the quantitative analysis of various surface features. The JEOL unit was used to select between secondary electron (SE) image mode and backscattered electron (BSE) image mode. All images were taken at 15KV accelerating voltage, as this was acceptable for resolving the microstructural effects being studied. A higher accelerating voltage could have been used (up to 40KV) for the EDS and quantitative analyses, but this was not required as indicated by the actual spectra taken. For every fracture surface analyzed, a series of images and spectra were taken at a high and low point on the surface for comparison. These images were taken at 100x, 500x, 1000x and 5000x for each high and low point. Then the entire surface was viewed to ensure the images taken were representative of all features on each sample. An image was also taken at 25x to show the general character of each surface.

Sample Cross-Section Analysis

The longer portion of each fractured sample was cut approximately 1.25 cm (0.49 in) from the fracture surface, perpendicular to the tensile axis. These portions – which included the fracture surface – were then placed into sample clips, which were then put into metallographic sample molds such that the diameter of the mold was concentric to the diameter of the sample. These molds were 3.175 cm (1.25 in) in diameter. The molds were coated with a thin coat of lubricating jelly. Two-part epoxy from Allied High Tech Products, Inc. was mixed and poured over the samples, placed into a ventilated hood and allowed to cure overnight. The samples were then removed from the mounts, washed in a solution of Dawn[®] brand dish detergent and tap water, and dried with paper towels.

These samples were then sectioned in half – parallel to the tensile axis – in a TechCut 4[™] low-speed saw with 6" x .020" x ½" high-concentration, metal bond diamond wafering blades.

Each of these was then polished by hand using a LECO VARI/POL Model VP-50 polishing wheel – shown in Figure 2-9 (*below*) – at 200RPM.



Figure 2-9. LECO VARI/POL VP-50 Polishing Machine.

This was done in successive steps with a combination of varying grits of SiC paper and varying sizes of alumina (Al_2O_3) powder suspended in water on a Hudson Selvyt cloth. The sequence of SiC papers was 400, 600, 800 and 1200 (all in U.S. Industrial Mesh Size), and the sequence of alumina powder was $1.0 \mu\text{m}$ (3.9×10^{-5} in) followed by $0.3 \mu\text{m}$ (1.2×10^{-5} in). For each polishing step, the sample was held in one direction until all scratches from the previous step were gone, and until all scratches from the current step were observed to be in the same direction. This was accomplished by rotating the sample 90° each time a new grit or mesh size was used. Between each step, the samples were washed with Dawn[®] brand dish detergent and tap water, rinsed vigorously with tap water, soaked with isopropyl alcohol and dried with a hairdryer. In addition, the polishing wheels were rinsed thoroughly and new media was put on

for each sample. Each sample was etched with Pratt & Whitney Etchant #17 (25 mL HCl, 25 mL HNO₃, 25 mL H₂O and 0.75 g molybdic acid), using a swipe method with cotton swabs. The etched samples were rinsed with tap water, dried with compressed air, and put into a plastic container with individual compartments like the one described previously, wrapped in tissue paper to protect the surface during transport.

These polished samples were then evaluated using a LECO Neophot Model 21 optical microscope – shown in Figure 2-10 (*below*) – with SPOT advanced software from Diagnostic Instruments, Inc. on an attached standard desktop computer. A series of 4 images were taken at 50x and then merged into one larger image using the Microsoft Paint program. This was done to show the general character of the microstructure in the vicinity of the fracture surface.



Figure 2-10. LECO Neophot 21 Optical Microscope.

The same JEOL JSM 6400 SEM as that described in the Fracture Surface Analysis section was used to image the etched samples. Like the ones taken for that analysis, all images of the cross-sectioned samples were taken at 15KV accelerating voltage, which proved to be effective.

A series of images were taken of these cross-sections in the following manner:

- Images at 200x to show the general character of the sample beneath the fracture surface, such as development of sub-surface cracks and concentration of carbides.
- Images at 1000x, 2500x and 5000x. An image at each of these magnifications was taken for the following points:
 - ✓ Just below the fracture surface along the vertical axis of the sample.
 - ✓ 1 mm (0.04 in) below the fracture surface along the tensile axis.
 - ✓ 1 mm (0.04 in) below the fracture surface at the left and right edges of the sample.
 - ✓ 2 mm (0.08 in) below the fracture surface along the tensile axis.

All images were used to compare the microstructure of the samples to that of other samples, and the second set of images at higher magnification were used to compare the microstructure of each area on an individual sample to other areas at the same magnification.

CHAPTER 3
RESULTS

Mechanical Testing

Tensile Testing

Since the emphasis of the project was to develop a creep-resistant alloy which would perform well under high-temperature and relatively high stress conditions, the tensile properties were not considered the most critical information for the success of this project. Due to the limited number of samples, only a few tensile tests were performed. Thus, the tensile testing was performed at room temperature – approximately 23°C (74F) – 750°C (1382°F), 850°C (1562°F) and 950°C (1742°F). All tests were conducted at a crosshead speed of 2.5 mm/min (0.1 in/min). The number of samples for the Baseline and Modification I alloys were very limited. Thus, it was decided not to perform any tensile testing on the Baseline alloy – as property data could be gleaned from the literature – and only one test was performed on the Modification I alloy at room temperature to ensure that the alloy modification did not result in embrittlement.

Numerical results from the tensile testing are shown in Table 3-1 (*below*):

Table 3-1. Tensile Testing Results.

Mod #	Sample ID	T (°C)	YS (MPa)	UTS (MPa)	E (MPa)	Elongation (%)
I	7-2	RT	870.8	1077.0	431.6	23.2
II	28-2	RT	870.1	1010.1	481.3	26.5
III	37-1	RT	906.0	972.2	459.2	28.3
II	22-2	750	937.7	1079.8	368.9	9.8
III	40-1	750	904.6	1066.7	392.3	13.8
II	24-1	850	981.2	1032.2	346.8	9.5
III	39-1	850	977.0	1071.5	341.3	12.4
II	25-1	950	433.0	732.9	310.3	11.3
III	37-2	950	508.9	735.0	352.3	18.2

From this data, the following are evident:

- The sample elongation for each sample dropped markedly from the RT tests to those performed at higher temperatures, as would be expected.
- The UTS for each sample was – to a lesser or greater degree – higher than the YS of the sample, indicating that there was at least some work hardening occurring, even if slight.
- There appears to be no general trend where T vs. YS or where T vs. UTS are concerned for each alloy. There is an increase in these values from RT to 750°C, and then again from 750°C to 850°C, but then a sharp drop between the values at 850°C and 950°C.
- There is little difference between the values for YS for the Modification II and III alloys except at 950°C.
- There is little difference between the values of UTS for the Modification II and III alloys at any temperature.

The data from Table 3-1 was obtained from graphs of the raw data from the tests, which was imported into an Excel spreadsheet and graphed. These graphs are shown in Figures 3-1 through 3-4 (*below and subsequent pages*):

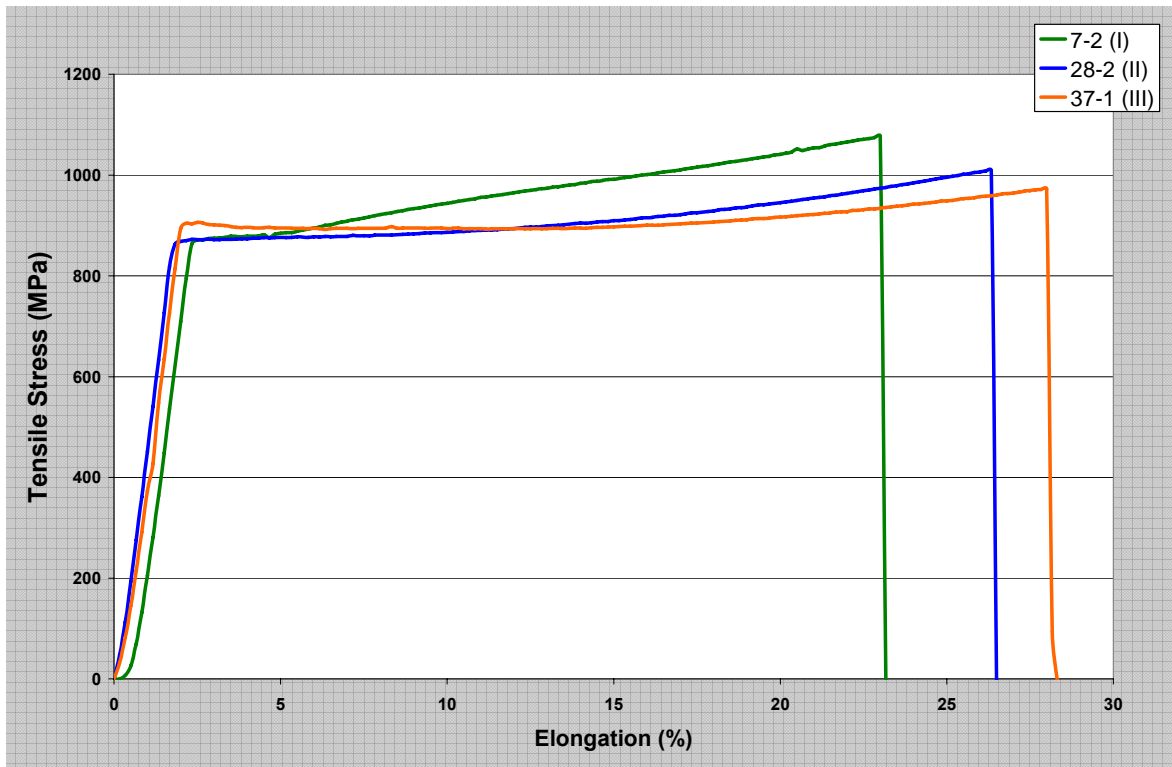


Figure 3-1. Room Temperature Tensile Testing Results.

In all three alloys, a fairly sharp yield is indicated. Additionally, the YS for all three alloy modifications were similar. It should be noted that there is a slight change in slope toward the bottom of the tensile curve for all tests except those at 950°C. This is a result of a small amount of slack in the initial setup and was therefore ignored when considering the 0.2% offset. Modification II and III alloys undergo less work hardening and are more ductile than the Modification I alloy. The slight drop in strength with increasing strain seen on the Modification II and III alloys indicate the occurrence of a slight amount of necking in the sample, which is consistent with what is observed on the samples themselves. The amount of work hardening of these alloys was approximately 206 MPa (30Ksi), 138 MPa (20Ksi) and 69 MPa (10Ksi) for Modifications I, II and III (respectively).

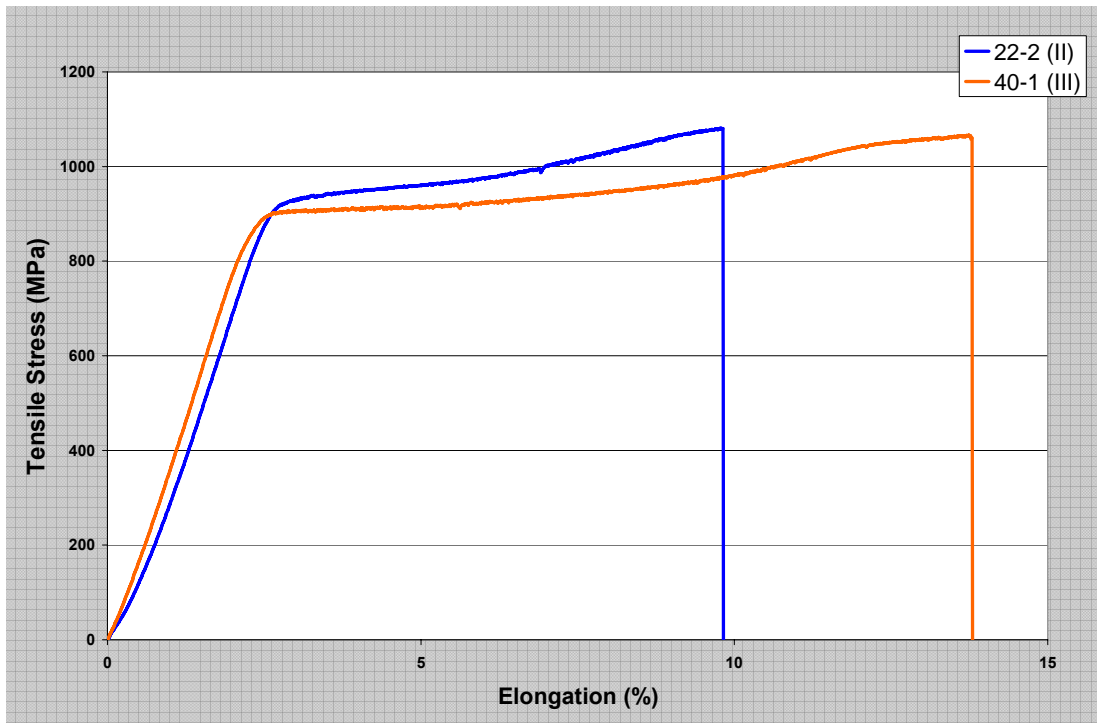


Figure 3-2. 750°C Tensile Testing Results.

For the remaining tests (750°C, 850°C and 950°C), Modification I alloy was not tested at the outset of mechanical testing due to the limited number of available samples.

Similar to the results of the tests at room temperature, the 750°C tests indicate only a slight amount of work hardening in the two alloys – approximately 145 MPa (21Ksi) and 165 MPa (24Ksi) for Modifications II and III (respectively). And, like the previous tests, Modification II and III have similar values of YS and UTS. The Modification III alloy exhibited a greater amount of elongation than did the Modification II alloy. The yield points appear to be slightly less sharp than those for the previous test, but this is actually a result of the difference in x-axis scale rather than an actual change in behavior.

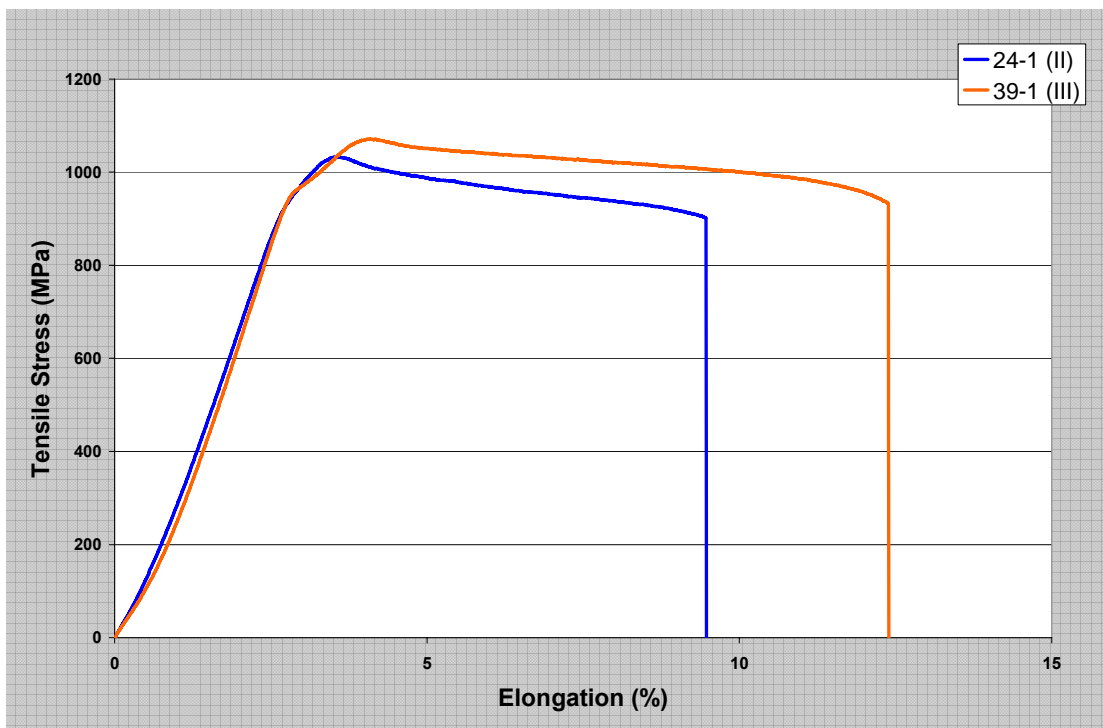


Figure 3-3. 850°C Tensile Testing Results.

The results of the 850°C testing were similar to those of the 750°C testing, however, the stress-strain curves exhibited very different behavior. A sharp yield point was not observed and flow softening was observed at the higher test temperature. Rather than a steady work hardening at a relatively low rate as noted in the 750°C tests, the samples tested at 850°C undergo an immediate increase in strength following the yield point. This is followed by a dropoff in

strength – indicating some necking has occurred, which is consistent with what was observed on the samples. As with previous tests, the YS of both alloys is similar, but in this case, the YS of the Modification III alloy is higher, contrary to previous results. However, consistent with previous results, the Modification III alloy displays a greater amount of ductility than the Modification II alloy.

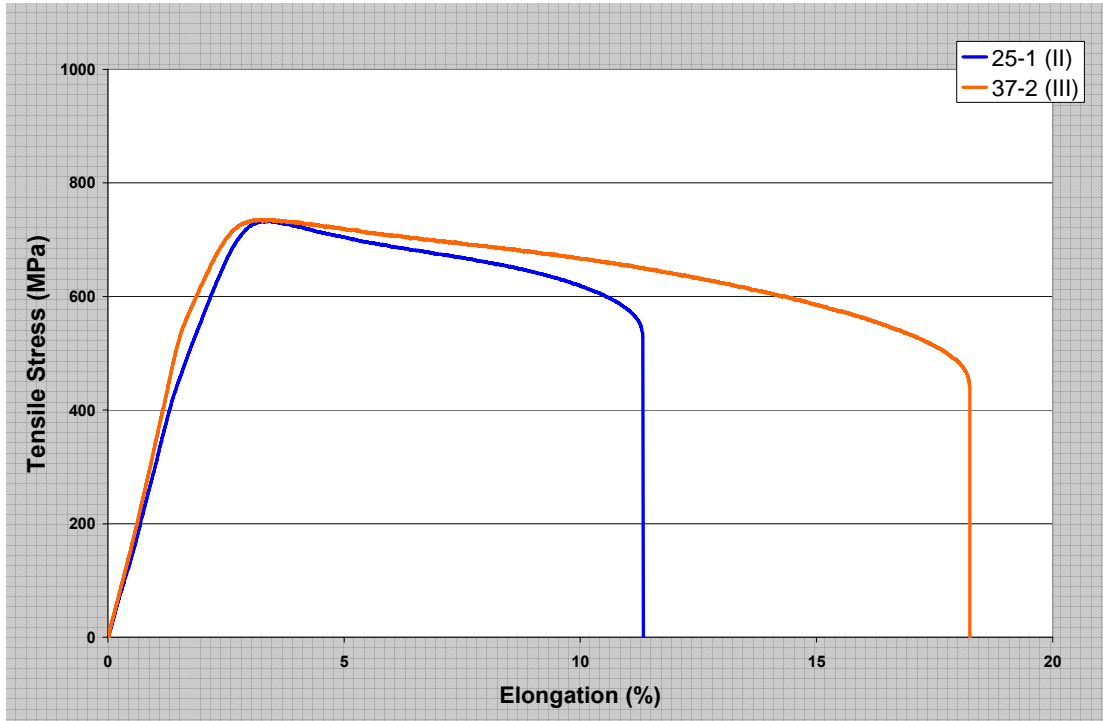


Figure 3-4. 950°C Tensile Testing Results.

The results of the 950°C tensile testing are similar to those at 850°C: a smooth yield point, then a significant immediate work hardening of the alloy, followed by a dropoff in strength until failure – indicating necking occurred, which is again consistent with what was seen on the samples. The YS of the two alloys are again similar, with Modification III having a slightly higher value. In these tests, however, the UTS values are almost identical for the two alloys, whereas in the tests at 850°C, Modification III showed a slightly higher value than Modification II. Modification III again shows a significantly higher ductility than does Modification II.

Closer examination of these curves indicates an bending point along the elastic portion of the curves, which can be seen more clearly in Figure 3-5 (A-B) (*following page*). Existence of such a bending point suggests that there is some change in deformation mechanism, which is why the YS values were based upon this point, rather than the upper point on each curve. It is highly unlikely that this behavior was due to slippage of the extensometer, because the other tests did not exhibit such behavior, and the behavior was consistent within each set of conditions.

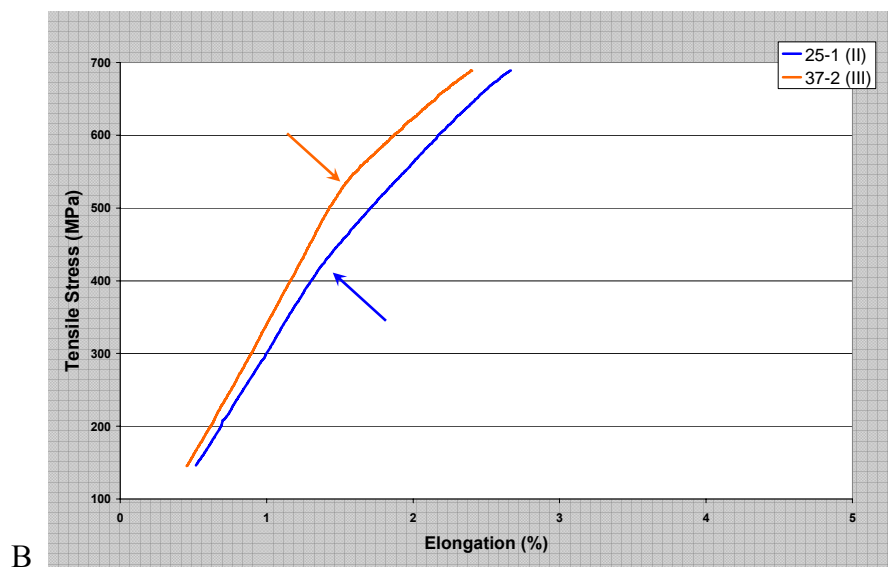
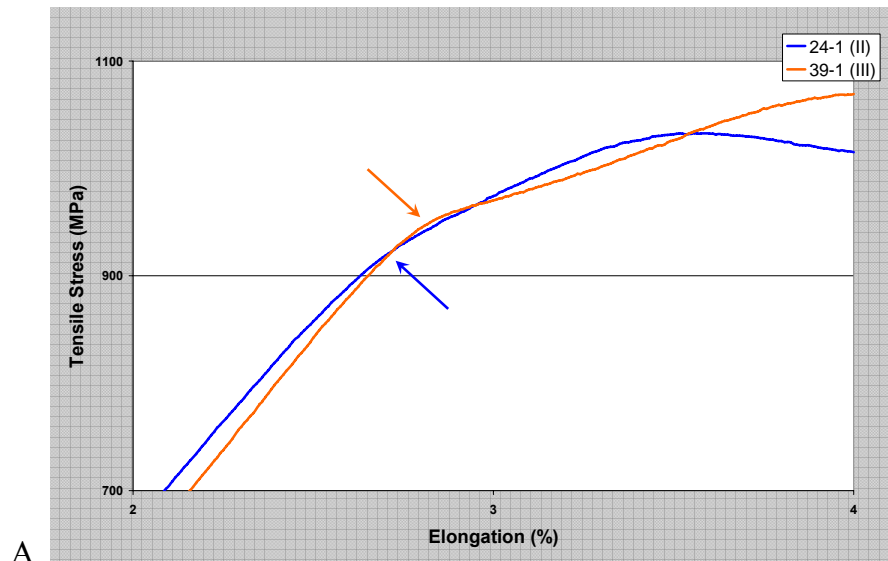


Figure 3-5. Magnified Portions of Tensile Testing Curves at A) 850°C and B) 950°C. Bending points identified by arrows.

Figures 3-6 and 3-7 (below) illustrate the changing behavior of each alloy with temperature:

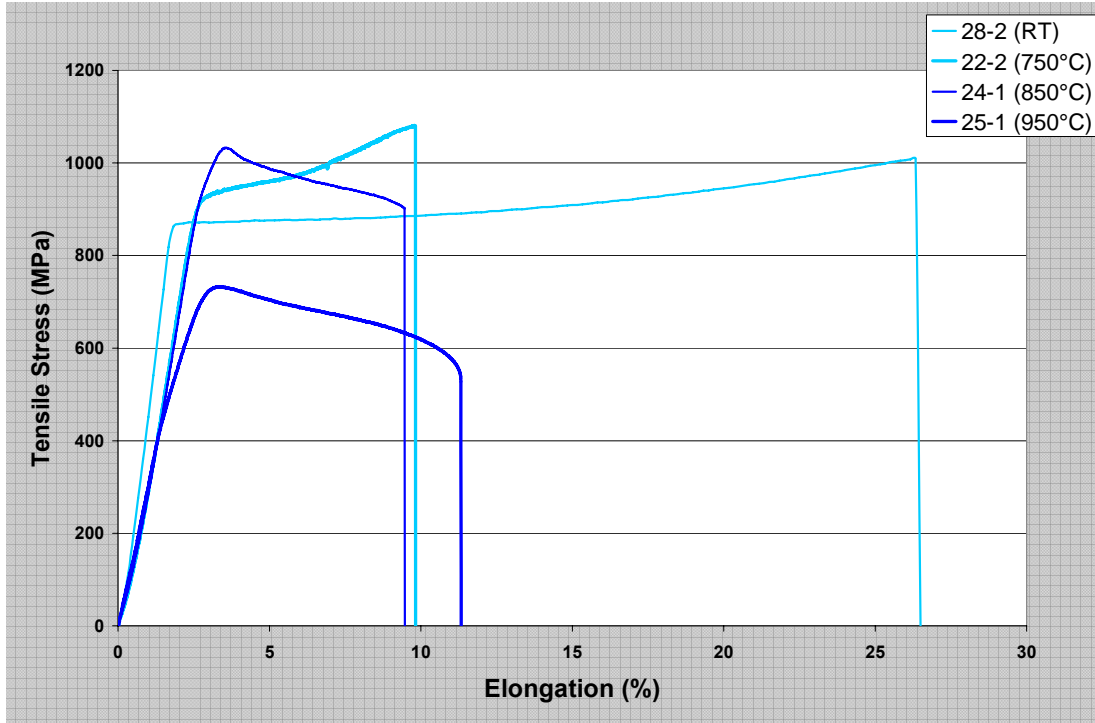


Figure 3-6. Modification II Tensile Testing Results.

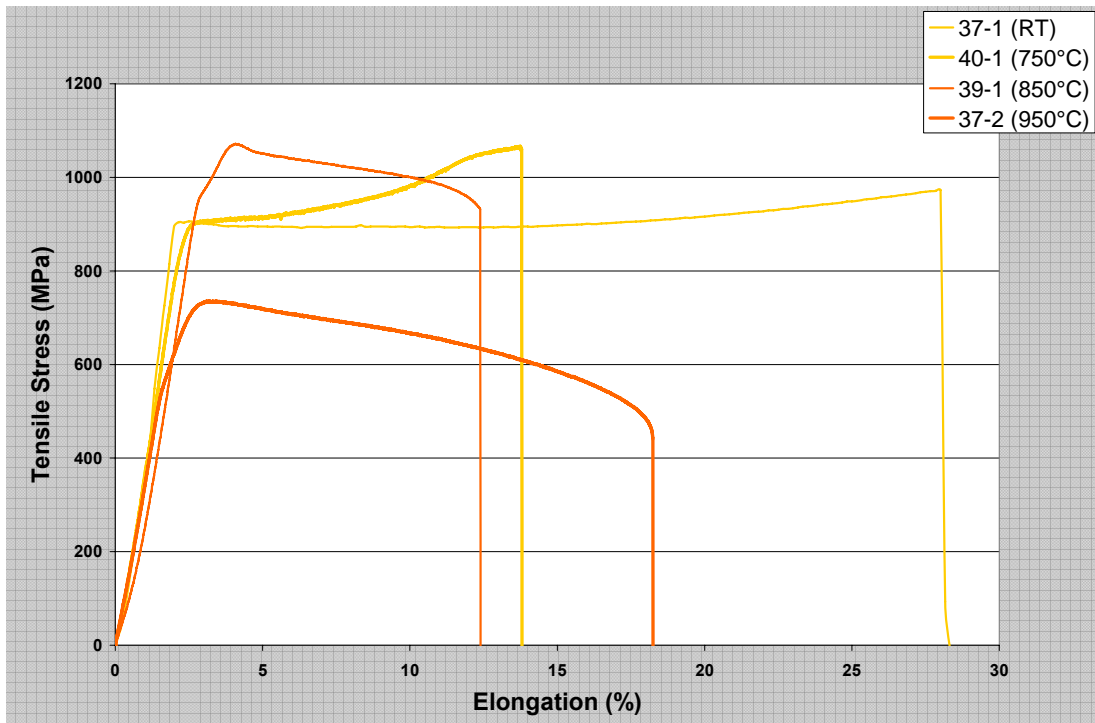


Figure 3-7. Modification III Tensile Testing Results.

The data shown in Figures 3-6 and 3-7 suggests that temperature has a similar effect on the tensile properties of both Modification II and III alloys. In general:

- Stress vs. Strain curves for RT testing were characterized by a sharp yield point, a relatively long period of plastic deformation with a limited amount of work hardening and finally failure.
- Stress vs. Strain curves at 750°C also exhibit a sharp yield point, but undergo a more significant degree of work hardening, particularly at strains close to the fracture strain.
- Stress vs. Strain curves at 850°C have bending points at their YS values, rather than a sharp yield, followed by a marked degree of immediate work hardening, and then a moderate amount of flow softening.
- Stress vs. Strain curves at 950°C also have bending points and undergo immediate work hardening, the degree of which is more significant than at 850°C. This work hardening is followed by a moderate amount of flow softening, as in the samples tested at 850°C.

Creep Testing

Creep testing provided a much more difficult scenario, due to the extremely limited availability of detailed data regarding the creep properties of PWA 1483 in the literature [24]. Although the literature data was not directly applicable to the current work, the results were used to develop a Larson-Miller time-temperature parameter. The following equation was derived to predict the appropriate conditions for the initial set of creep tests:

$$\sigma = \text{LOG}^{-1} \left[(-2.8732 \cdot \ln \left(\frac{T(\text{LOG} t_f + 20)}{1000} \right)) + 11.887 \right]$$

Use of this equation indicated that at a desired time to failure of 144 hours, the required stress would be 831.5 MPa (120.6 Ksi) at 750°C. 144 hours was chosen as a reasonable time based upon availability of creep frames and project duration, given the number of tests which were planned to be performed. In addition, it was decided at the outset that because there were few available samples for the Baseline and Modification I alloys, that the first tests would be completed on the Modification II and III alloys. By doing this, it was possible to ensure that if

the conditions turned out to be completely inappropriate, the few Baseline and Modification I samples would not be wasted. The resultant test sequence is shown in Table 3-2 (*below*):

Table 3-2. Sequence of Creep Testing.

Mod #	Sample ID	T (°C)	Stress (MPa)	Start Date	Rupture Life (hr)	Frame
II	23-2	750	831.5	26-Sep	44	1
III	39-2	750	831.5	26-Sep	55	2
II	24-2	850	448.9	27-Sep	327	4
II	25-2	750	724.0	4-Oct	174	1
III	41-1	750	724.0	9-Oct	958	2
III	40-2	850	448.9	12-Oct	801	4
B	4-10A2	750	831.5	25-Oct	25	1
B	4-10A1	850	448.9	28-Oct	123	1
I	7-1	750	831.5	6-Nov	53	1
I	12-1	850	448.9	9-Nov	122	1
B	4-10B2	950	344.8	17-Nov	12	1
II	26-1	950	344.8	24-Nov	26	2
III	43-1	950	344.8	24-Nov	46	4
I	13-1	950	344.8	30-Nov	14	1

The results of the first set of tests at 750°C on the Modification II and III alloys indicated that the conditions were satisfactory, but the rupture life was less than expected – significantly so in some cases. Upon further analysis, this was a result of the inaccuracy of the regression model used to derive the initial equation. This inaccuracy could have been caused by the small number of data points used or by the existence of a change in creep mechanism – the latter of which is frequently seen in such LMP plots. In order to respond to the short rupture life problem, the conditions were changed by extending the desired rupture life in the equation to 425 hours. When this value was used in the equation, the resultant stress – 724 MPa (105 Ksi) – was

between the value indicated by the literature data and the value used in the first set of tests. This was determined to be a numerically favorable condition, and was therefore used for the second set of tests performed at 750°C.

The rupture life of the two samples tested under these new conditions also diverged from the predicted value of 425 hours, which was expected. What was not expected was that for the Modification II alloy, the rupture life did indeed increase, but not nearly as much as was predicted. On the other hand, the rupture life of the Modification III alloy increased by a great deal more than was predicted. In fact, the Modification III sample failed just prior to the run-out time of 1000 hours, allowing rupture life to be assessed for that sample.

When the tests were completed for the each of the Modification II and III alloys at 750°C, the data for the first set of conditions (831.5 MPa) seemed to offer more consistent results than for the second (724 MPa), e.g.: samples tested at the former set of conditions exhibited similar behavior. It was therefore decided to use this set of conditions rather than the second set to test the Baseline and Modification I alloy samples. The tests for these samples were subsequently completed.

As these two tests were in progress, the test on the Modification II alloy at 850°C was completed, and the test on the Modification III alloy at 850°C was commenced. Due to the duration of the tests being performed on the Modification II alloy at 750°C/724 MPa and the Modification III alloy at 850°C/448.9 MPa, the remaining frame was used extensively to complete the tests on the Baseline and Modification I alloys at 750°C and 850°C. These were completed before the end of the aforementioned test on the Modification III alloy.

Upon completion of all testing at 750°C and 850°C, the results were plotted and assessed to determine the appropriate conditions for the final set of tests at 950°C. Only one equation had

been used to determine the predicted failure time and required conditions at the two lower temperatures. However, once the tests were completed at these two temperatures, there was enough data to merit calculating an LMP curve for each alloy – including a new curve for the Baseline alloy with the new data points added. This was done in a similar manner as that used to calculate the first equation (logarithmic regression using Excel software).

The obvious weakness of this method was that it had already proven to be somewhat inaccurate, possibly because of a low number of data points used. However, the new results indicated that there was a difference between the three alloys from an LMP plot perspective – not just between one another, but different from the Baseline alloy as well. For that reason, individual equations were used. The separate equations are as follows:

- **Baseline:** $\sigma = LOG^{-1} \left[(-2.6477 \cdot \ln \left(\frac{T(LOG t_f + 20)}{1000} \right)) + 11.149 \right]$
- **Modification I:** $\sigma = LOG^{-1} \left[(-2.3683 \cdot \ln \left(\frac{T(LOG t_f + 20)}{1000} \right)) + 10.245 \right]$
- **Modification II:** $\sigma = LOG^{-1} \left[(-2.3417 \cdot \ln \left(\frac{T(LOG t_f + 20)}{1000} \right)) + 10.210 \right]$
- **Modification III:** $\sigma = LOG^{-1} \left[(-2.3329 \cdot \ln \left(\frac{T(LOG t_f + 20)}{1000} \right)) + 10.188 \right]$

Simultaneous use of these equations resulted in the stress of 344.5 MPa (50 Ksi), which predicted a range of failure times from 13.75 hours for the Baseline alloy to 225 hours for the Modification III alloy. This range was considered reasonable, and the value of 344.5 MPa was subsequently used for the stress in the final set of tests.

The final Larson-Miller plot is shown in Figure 3-8 (*following page*), with the derived equations for each trendline displayed for comparison.

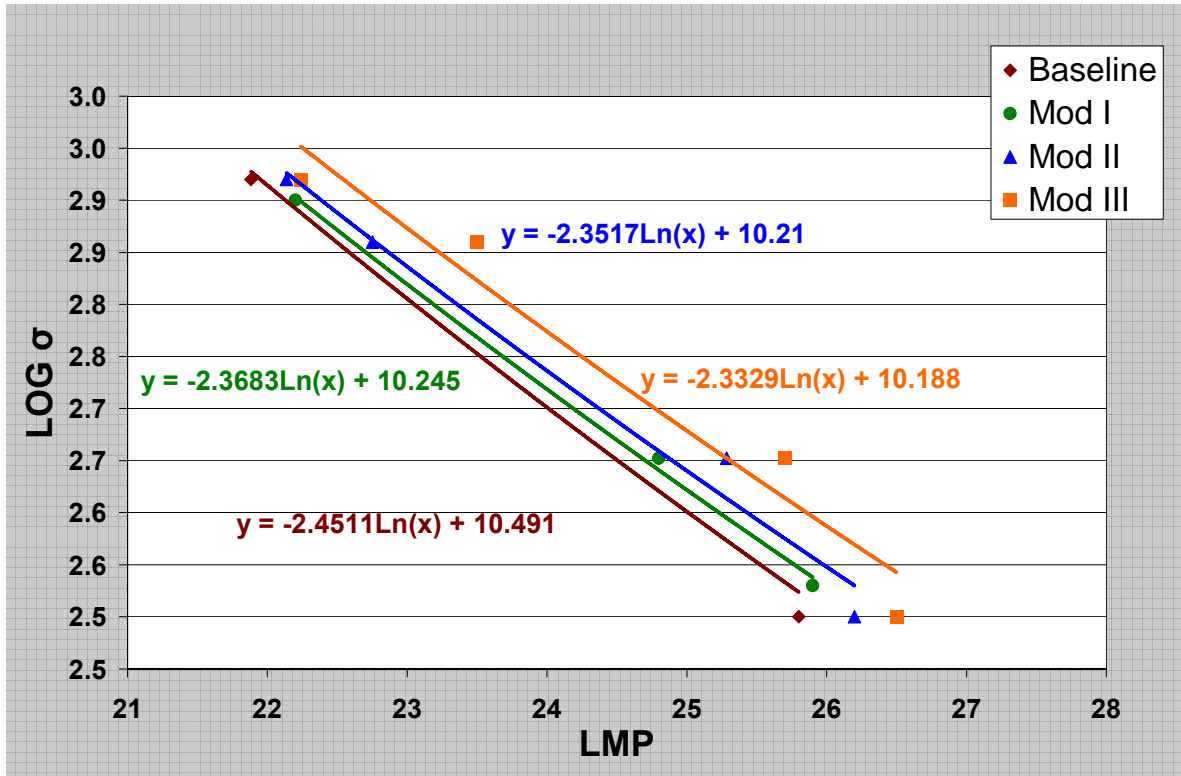


Figure 3-8. Larson-Miller Plot.

The trendlines and associated equations seen in Figure 3-8 are based on a limited number of results. As such, it is understood that many more tests would be required to meet the standards of statistically-based testing matrices. However, based on this data, additional investigation into these modifications is clearly merited.

The results of the first set of 750°C creep tests can be seen in Figures 3-9 and 3-10 (*following page*). The testing at 831.5 MPa indicates that all three modifications undergo some degree of pronounced primary creep, followed by a long period of secondary and tertiary creep. These regions are characterized by: a rapid rise in elongation initially (primary); a region of low, nearly-linear creep rate (secondary); and a region of exponentially increasing elongation to failure (tertiary). The transition between the regions of secondary and tertiary creep is not clearly evident, indicating that there may be significant overlap of the mechanisms typically dominate each region.

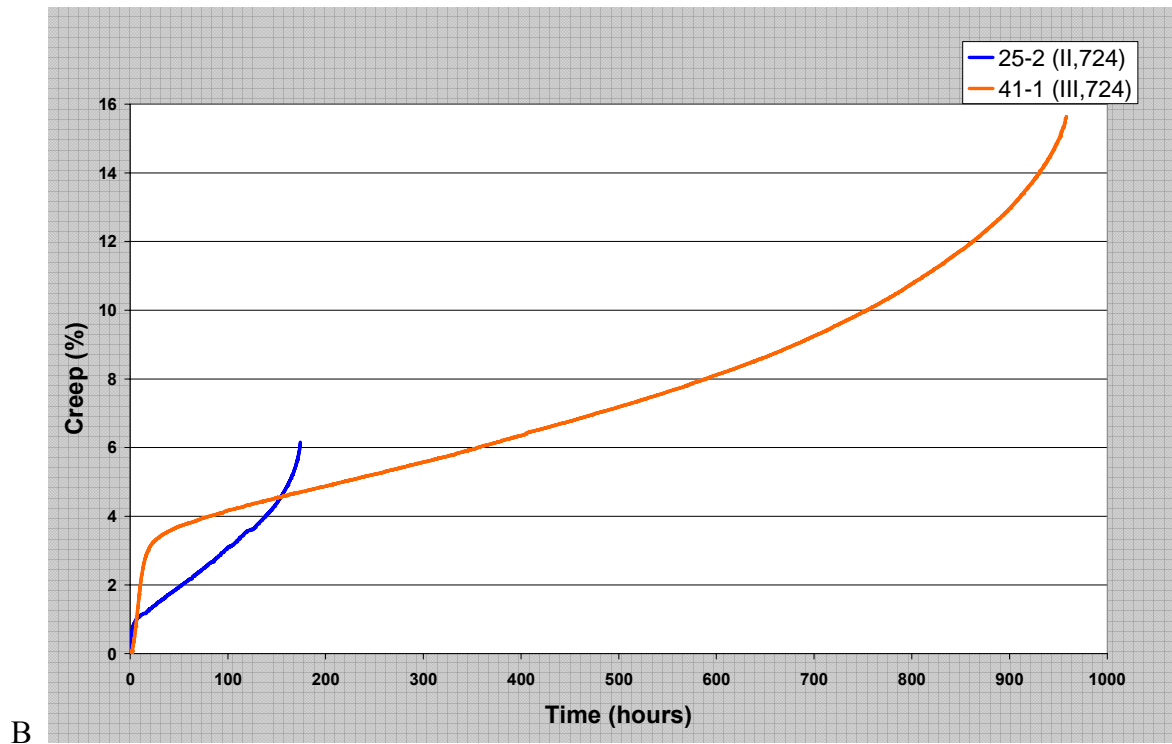
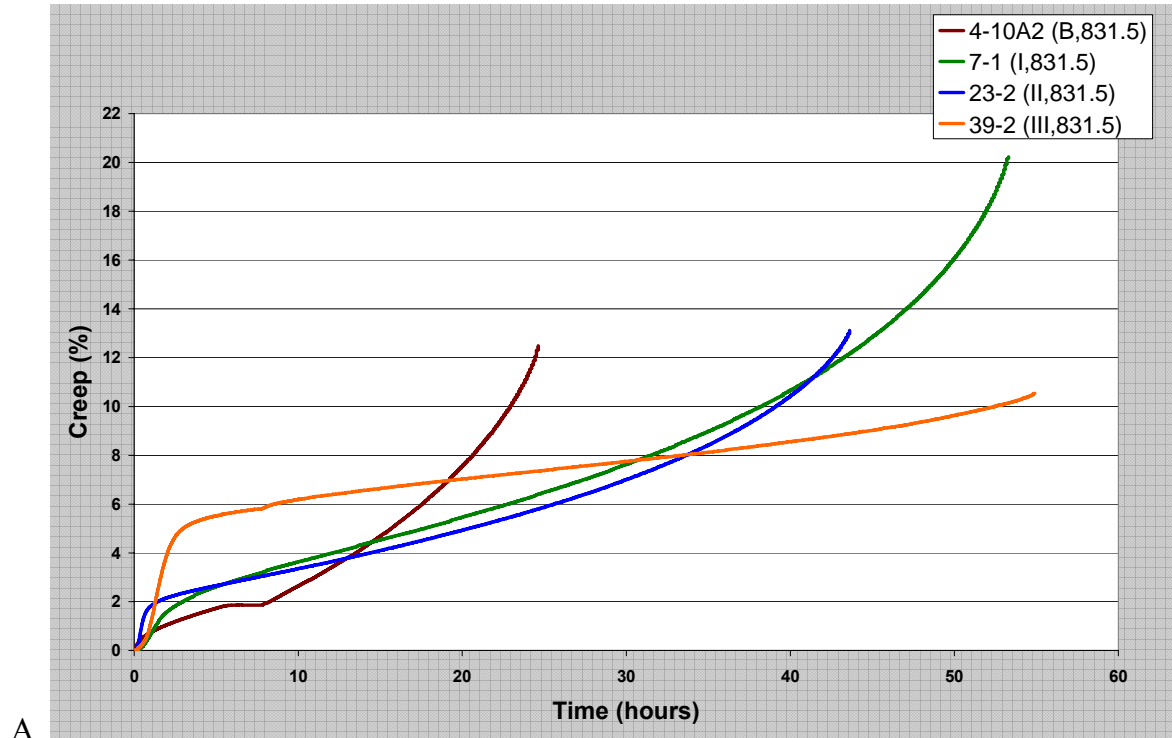


Figure 3-9. 750°C Creep Testing Results for A) 831.5 MPa B) 724 MPa.

The Baseline alloy undergoes much less primary creep than does the Modification III alloy, and about the same amount as the Modification I and II alloys. This can be seen more clearly in Figure 3-10 (*below*). There is some delay involved between the effect of primary creep on the Baseline alloy in relation to the others, but the degree is so small (only a few hours), that on the scale of the lifetime of the alloys, the difference is insignificant. Similarly, in the case of lifetimes, all three of the modified alloys outperform the Baseline alloy, but this alone is not indicative of improvement across the board.

The curves for the 724 MPa tests are shown in Figure 3-10 as well, but obviously no comparison may be made between the Baseline and the Modification II and III alloys at that stress level. These are provided in the graph to show the difference in the primary creep behavior exhibited by the same alloy at a lower stress condition.

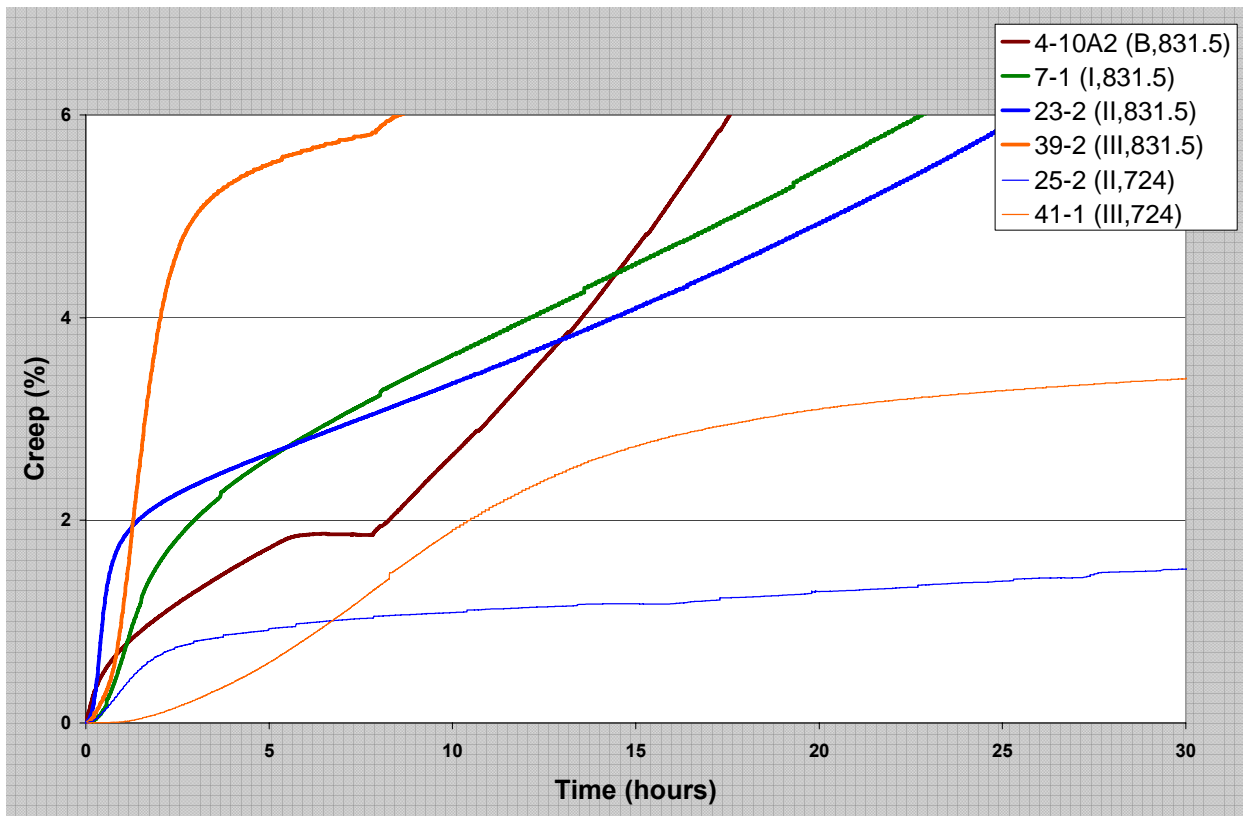


Figure 3-10. Magnified Portion of Creep Testing Curves at 750°C.

The results of the 850°C creep tests can be seen in Figure 3-11 (*below*):

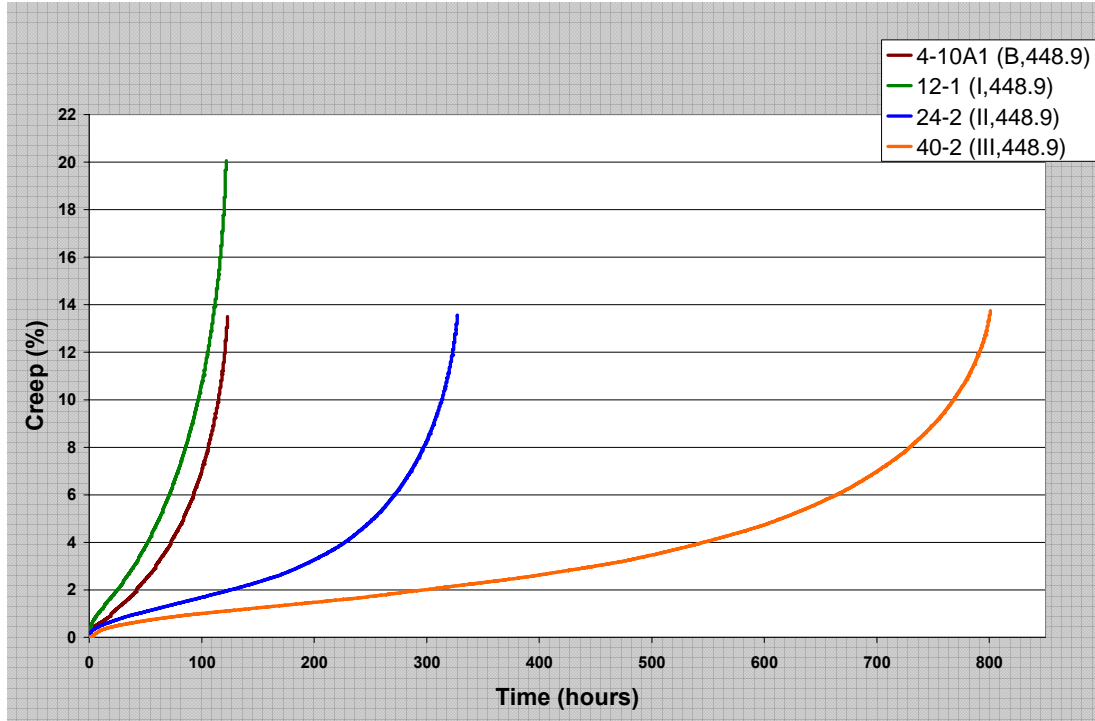


Figure 3-11. 850°C Creep Testing Results.

The results for these conditions indicate that Modifications II and III exhibit improved lifetimes from that of the Baseline alloy, whereas Modification I exhibits decreased creep resistance compared to the Baseline. The improvement of the Modification II and III alloys shows significant promise, in that it represents between a 3x and 8x increase. In addition, it appears that where the Baseline alloy exhibited a slightly longer delay in primary creep than did any of the three modified alloys at 750°C/831.5 MPa, in this case, the Modification II and III alloys now have a longer delay, as can be seen in Figure 3-12 (*following page*). Again, the difference in the delay of primary creep is insignificant on the scale of the lifetime of the alloys, but the data seems to indicate that there is at least some improvement. Again, there is no clear transition point between the secondary and tertiary regions of creep, indicating significant mechanism overlap as before.

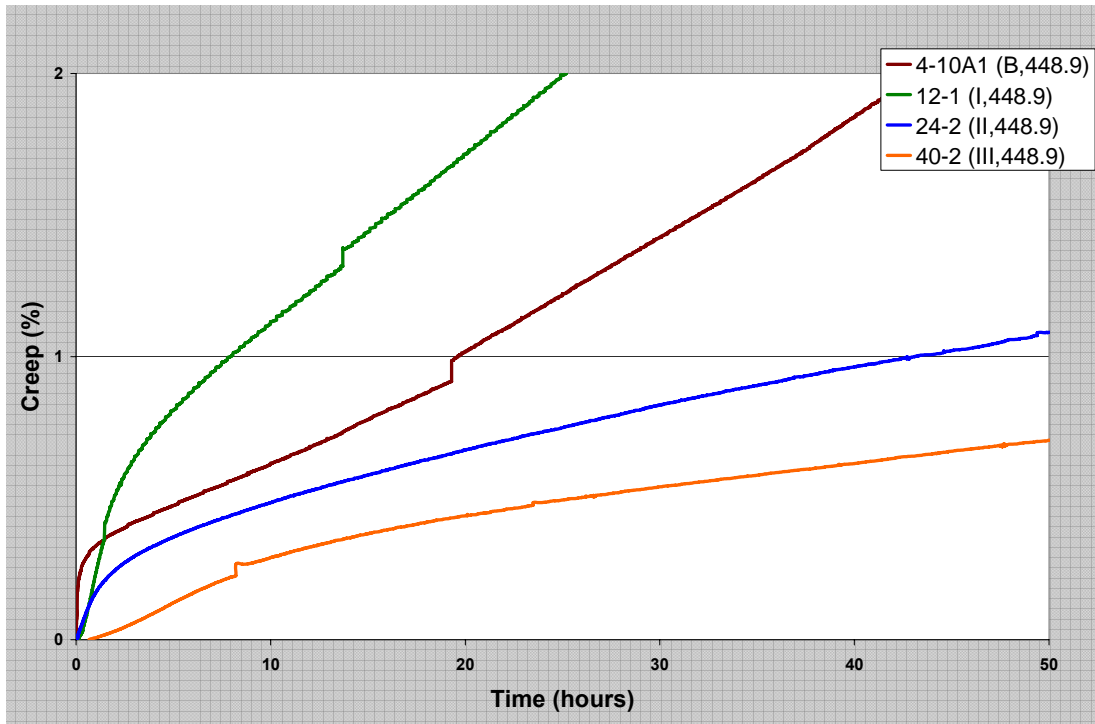


Figure 3-12. Magnified Portion of Creep Testing Curves at 850°C.

The results of the 950°C creep tests can be seen in Figure 3-13 (*below*):

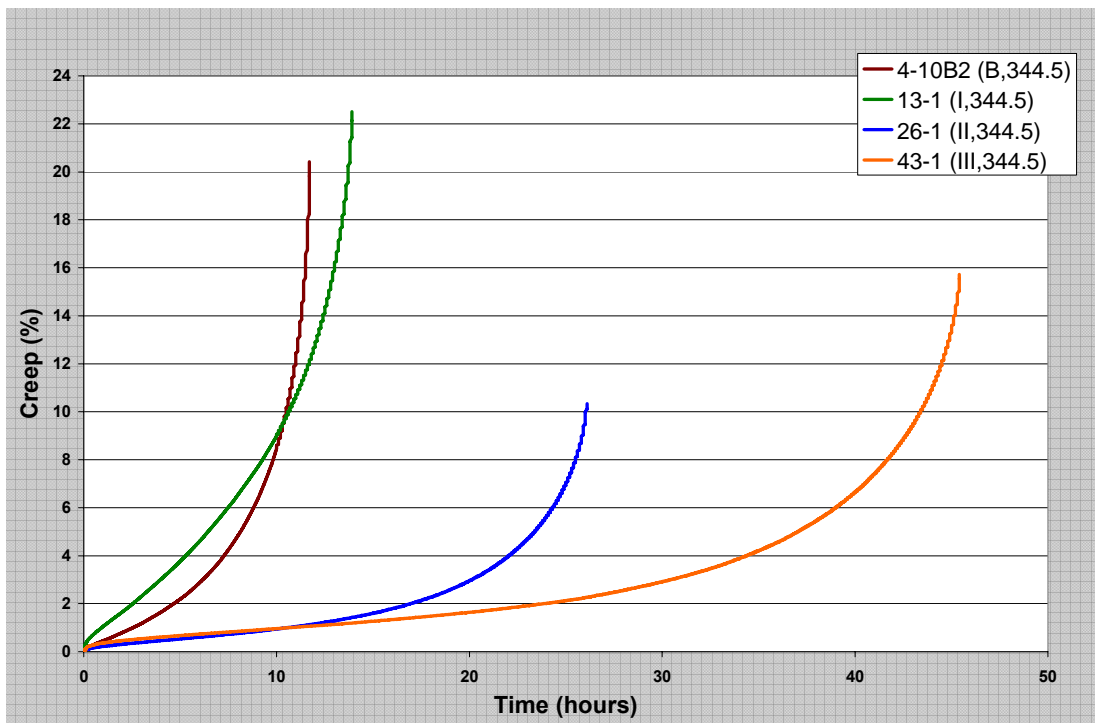


Figure 3-13. 950°C Creep Testing Results.

The data from the 950°C testing indicates that the Modification II and III alloys exhibit a much longer lifetime than the Baseline alloy, only now, the Modification I alloy shows a slight improvement in lifetime over the Baseline as well. Looking at the results of all three temperatures, the ductility of the Modification I and II alloys seem essentially unaffected by the change in conditions – exhibiting values between 20.0 and 22.5 and 10.3 to 13.1 (respectively) for the three tests. For those same three tests, the Baseline and Modification III alloys exhibit more variance – ranging from 12.5 to 20.4 and 10.5 to 15.7 (respectively).

The comparison of primary creep behavior can be seen in Figure 3-14 (*below*). The values for all three alloys are now essentially identical. In the case of the Modification I alloy, and somewhat for the Baseline alloy, it is actually of more concern that the alloys seem to go directly from primary to tertiary creep under these conditions.

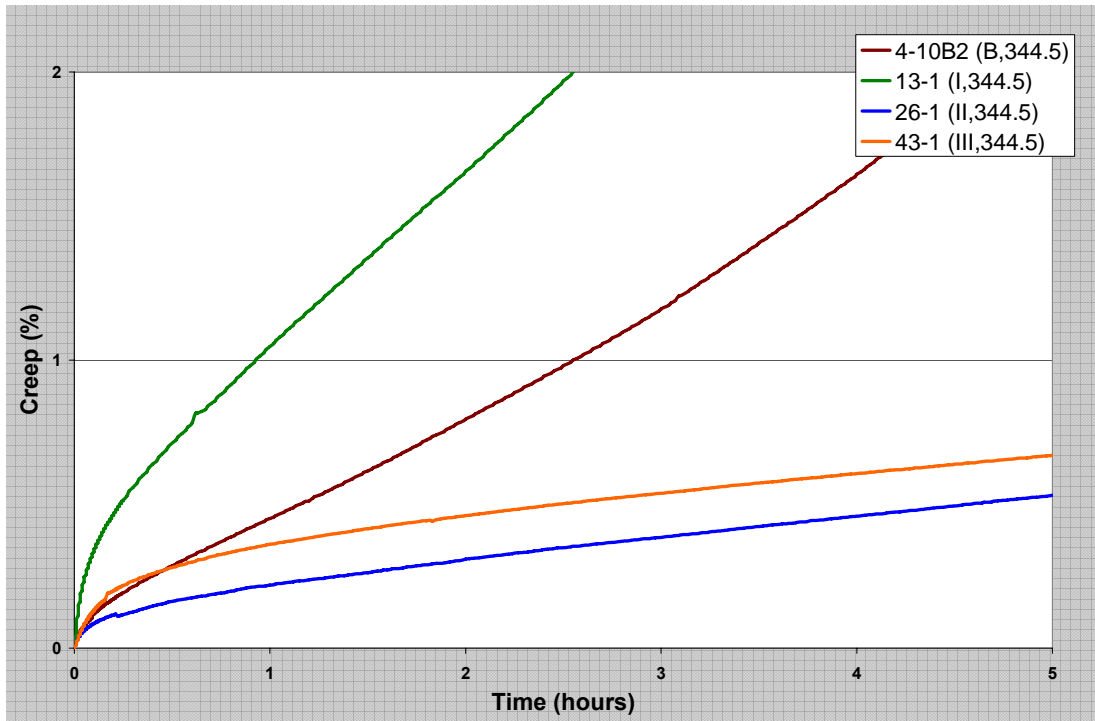


Figure 3-14. Magnified Portion of Creep Testing Curves at 950°C.

The final results of the creep testing can be seen in Table 3-3 (*following page*).

Table 3-3. Creep Testing Results.

Sample	Mod	T °C	Stress MPa	σ /YS	Time to 1% hours	Time to 2% hours	Rupture Life hours	Elongation %	E GPa	min Creep Rate /hour	LMP
4-10A2	B	750	831.5	**	1.8	8.3	24.6	12.5	71.0	-0.1145*	21.9
7-1	I	750	831.5	**	1.3	3.0	53.3	20.2	80.7	0.1853	22.2
23-2	II	750	831.5	0.89	0.5	1.4	43.6	13.1	81.2	0.1433	22.1
39-2	III	750	831.5	0.92	1.0	1.3	54.9	10.5	84.7	0.0760	22.2
25-2	II	750	724.0	0.77	6.4	52.8	173.9	6.2	78.8	0.0214	22.8
41-1	III	750	724.0	0.80	6.7	10.5	958.0	9.3	91.7	0.0077	23.5
4-10A1	B	850	448.9	**	19.6	41.9	123.0	13.5	64.7	0.0304	24.8
12-1	I	850	448.9	**	7.9	25.2	122.0	20.0	69.4	0.0557	24.8
24-2	II	850	448.9	0.46	43.1	126.0	327.0	13.6	67.6	0.0126	25.3
40-2	III	850	448.9	0.46	99.1	298.0	801.0	13.8	73.4	0.0050	25.7
4-10B2	B	950	344.5	**	2.6	4.7	11.8	20.4	51.7	0.3543	25.8
13-1	I	950	344.5	**	0.9	2.5	13.9	22.5	52.5	0.6118	25.9
26-1	II	950	344.5	0.80	10.6	17.0	26.1	10.3	60.1	0.0791	26.2
43-1	III	950	344.5	0.68	10.7	23.9	45.5	15.7	70.0	0.0589	26.5

*The negative value seen here is likely an effect of the software used to collect the data rather than an actual indication of material response.

**No tensile testing was conducted for the Baseline or Modification I alloys at these temperatures, therefore σ /YS ratios could not be calculated.

Characterization

Upon completion of mechanical testing on each sample, the sample was prepared for imaging and stored in a protective container. In terms of sequencing, all of the tensile testing and most of the creep testing was completed for all samples prior to performing these imaging analyses. This methodology was followed such that the instruments used for the imaging would be in a similar condition for the entirety of each process, e.g.: the instrument would not be overhauled or go through some major repair in the middle of the process, changing the appearance of the images relative to that seen prior to the repair. Since the images are being used comparatively, the desire was to maintain as much continuity in conditions as possible, such that any differences seen would be a result of differences in the material itself.

Fracture Surface Analysis

Fracture surfaces of all samples were analyzed using a JEOL JSM 6400 SEM at 15KV accelerating voltage. An image was taken at of each sample at 25x to show the general character of the fracture surface. Then a series of images was taken at various magnifications on a high point and a low point for each sample. The images of the high and low points were taken for comparison, both to each other as well as to those from other samples. The entire fracture surface of each sample was then viewed to ensure that the images at the high and low point were representative of what was seen throughout the fracture surface. These series of images were taken at 100x, 500x, 1000x and 5000x. For microstructurally significant features, EDS spectra were taken and analyzed as well. Since the emphasis of comparison between these images is between like samples (i.e.: tensile to tensile; creep to creep), the imaging for each is discussed separately.

Tensile Samples

An example series of the tensile sample fracture surfaces can be seen in Figure 3-15 (A-E) (*below*). An arrow is provided on the 25x image to show the location of the other micrographs.

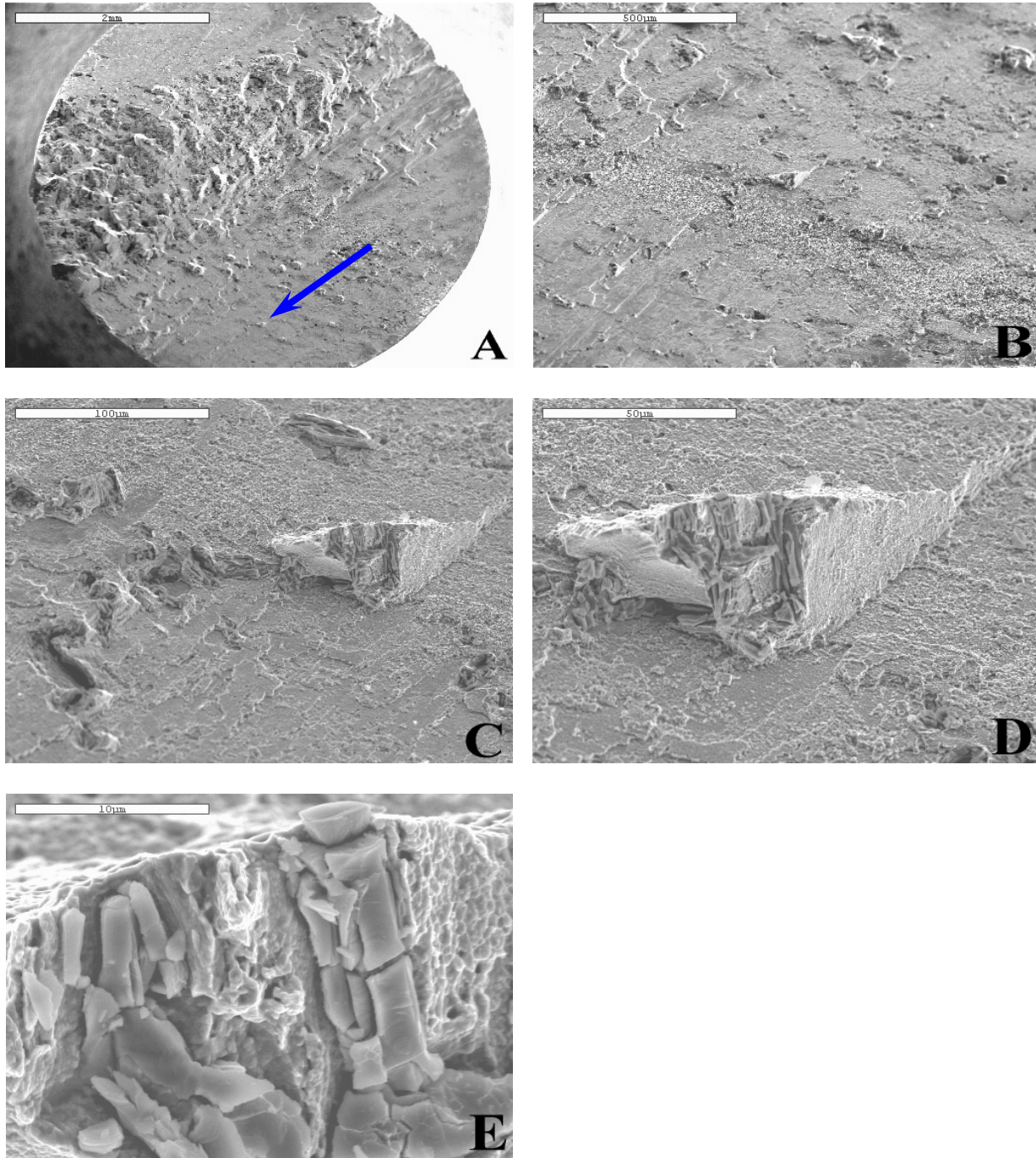


Figure 3-15. Fracture Surface of Tensile Sample (40-1; *Modification III*) at A) 25x B) 100x C) 500x D) 1000x E) 5000x.

The features seen in these images are typical of those seen on all the fracture surfaces of the tensile samples. These will be discussed in greater detail later, but in general, the fracture surfaces of the tensile samples exhibited the following:

- All surfaces contained mixed character deformation – a combination of cleavage-like fracture with some areas of more ductile-type deformation. There was no consistent quantitative split between the percent cleavage-like vs. the percent ductile areas. The cleavage-like regions were clearly dominant, on the order of approximately 90%.
- In some samples, casting porosity and voids were noted, but it appears these had little effect on the character of the surrounding fracture area.
- All surfaces exhibited a mixture of carbide structures. The majority of these carbides had been cleaved through as the fracture occurred, but there were also some which remained intact on the surface. There was also evidence that some carbides appeared to have been ‘ripped free’ from the surrounding γ/γ' material.
- The carbides observed on the fracture surfaces were of the MC type. No secondary carbides were noted, as expected. EDS indicated a high level of Ta and Ti in the carbide, whereas the surrounding material had increased levels of Ni, Cr and Co. Representative EDS spectra of the features shown in Figure 3-15 (E) can be seen in Figure 3-16 (A-B) (*following page*). A quantitative analysis of the two spectra is shown in Table 3-4 (*below*) for comparison.

Table 3-4. Quantitative Analysis of Features in Figure 3-15 (E)*.

Modification III alloy, Sample ID: 40-1							
Carbide				Surrounding area			
element	MW (g/mol)	Atomic %	Weight %	element	MW (g/mol)	Atomic %	Weight %
C	12.011	12.54	3.22	C	12.011	14.92	4.36
O	15.999	44.48	15.20	O	15.999	32.77	12.76
Al	26.982	1.24	0.71	Al	26.982	2.18	1.43
Ti	47.9	15.16	15.51	Ti	47.9	4.48	5.22
Cr	51.996	2.50	2.78	Cr	51.996	6.46	8.17
Co	58.933	1.95	2.45	Co	58.933	5.96	8.55
Ni	58.71	9.31	11.67	Ni	58.71	28.90	41.29
Mo	95.94	0.39	0.80	Mo	95.94	0.37	0.86
Ta	180.95	12.33	47.65	Ta	180.95	3.94	17.35
Total			100	Total			100

*Elements which are dominant in the EDS spectra of each feature are in bold.

**The Carbide scan was taken as a spot sample on the carbide itself. The Surrounding Area scan was taken for the entire area shown in Figure 3-15 (E). Values are shown to exhibit that there was a difference between the compositions of each area.

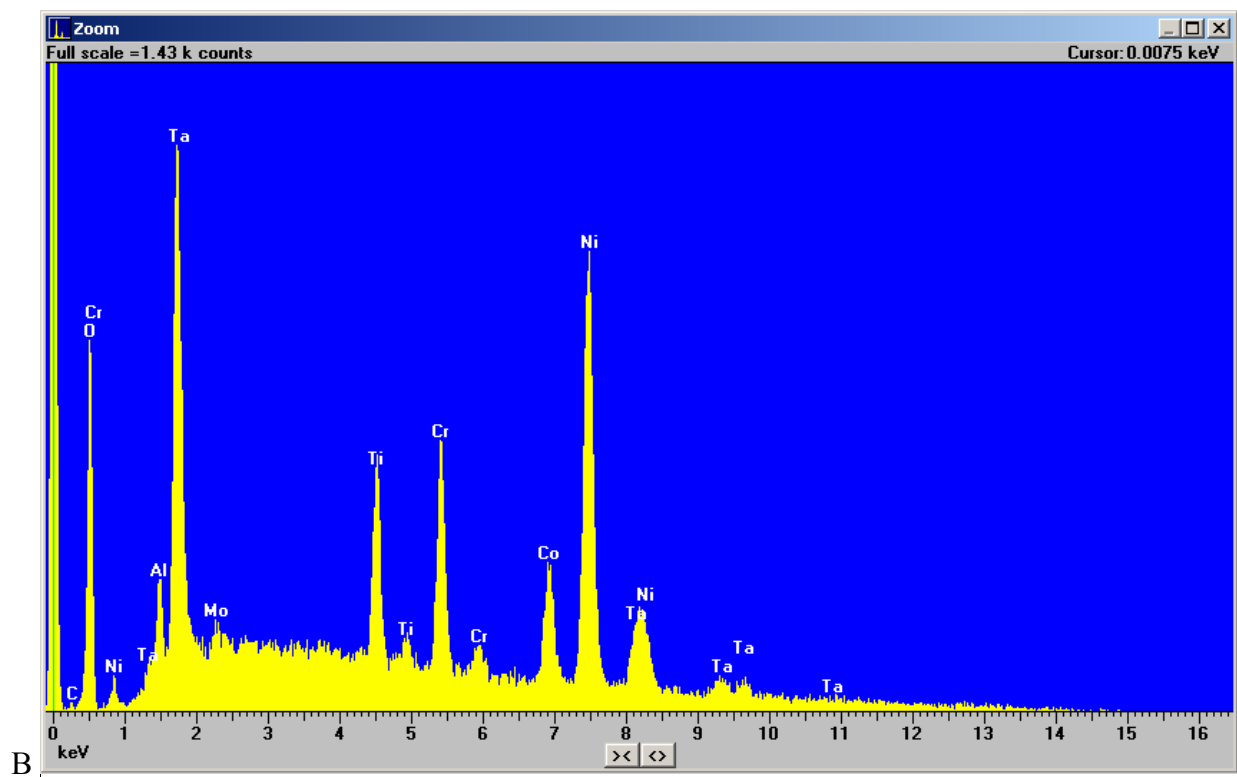
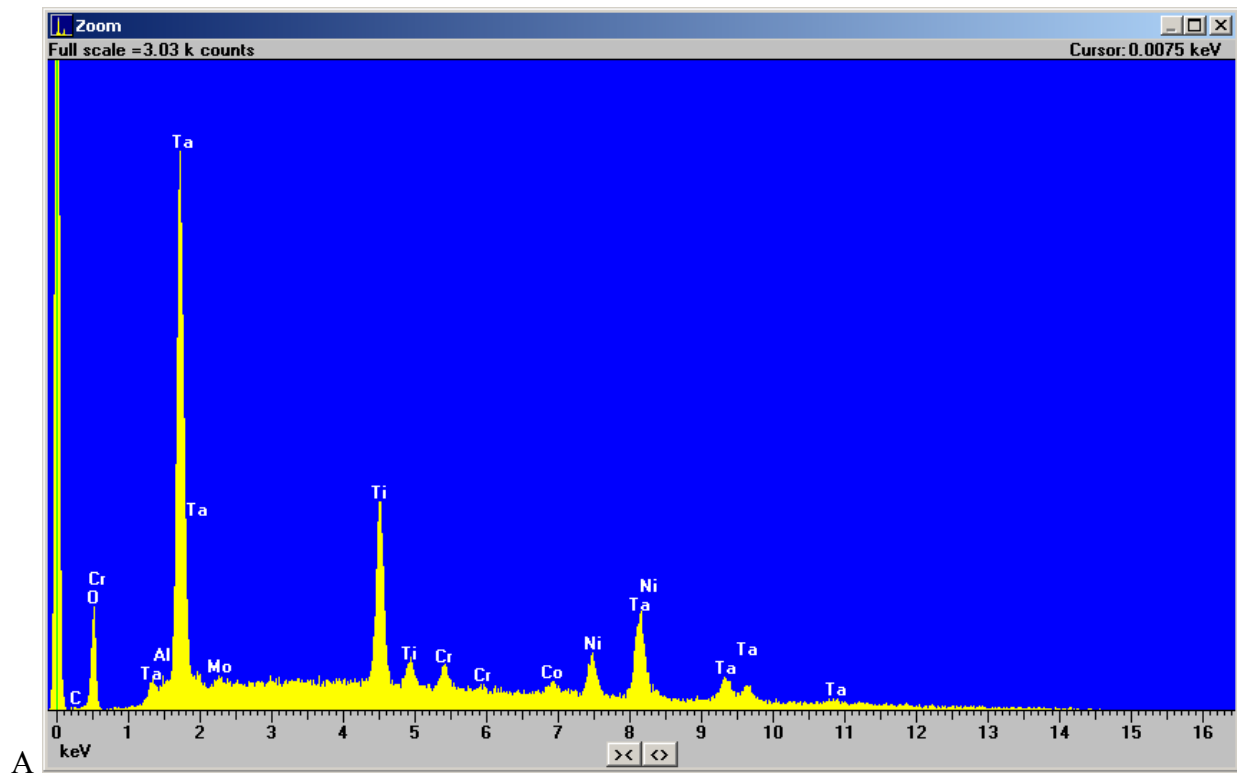


Figure 3-16. EDS Spectra of Sample 40-1 features: A) Carbide B) Surrounding Area.

The tensile samples exhibited mixed-character deformation at all temperatures. This was dominated by quasi-cleavage and cleavage-like fracture on the order of 90%. Evidence of ductility in all samples was present, but remained approximately 10% of the fracture surface in all cases. At low magnifications (25x, 100x) the surface sometimes appeared to be the result of a ductile-type failure, as seen in Figure 3-17 (A-B) (*below*):

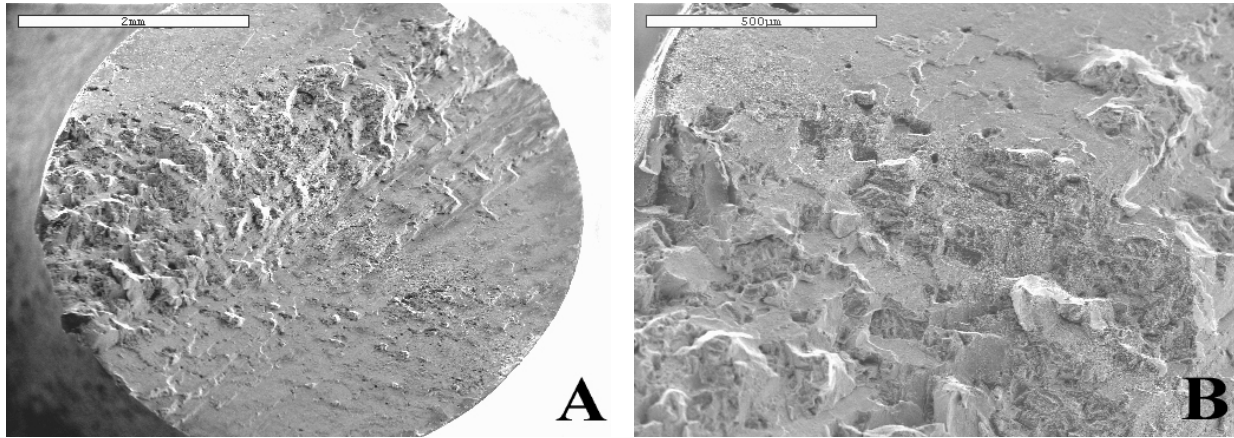


Figure 3-17. Fracture Surface of Tensile Sample (40-1; *Modification III*) at A) 25x B) 100x.

At higher magnifications (500x, 1000x) it can be seen clearly that this is not ductility at all, but rather quasi-cleavage on a large scale. Examples of this are shown in Figure 3-18 (A-B) (*below*).

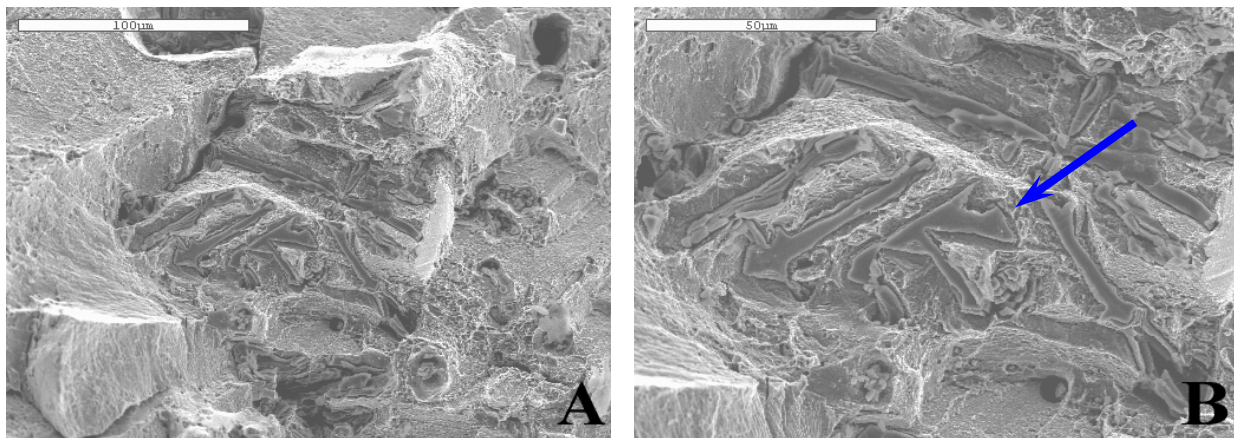


Figure 3-18. Fracture Surface of Tensile Sample (40-1; *Modification III*) at A) 500x B) 1000x.

The image at 500x clearly shows the regions of cleavage, as well as those of quasi-cleavage. A blue arrow on Figure 3-18 (B) is provided to show the location of the image in Figure 3-19.

At the highest magnification (5000x) the character is evident, seen in Figure 3-19 (*below*).

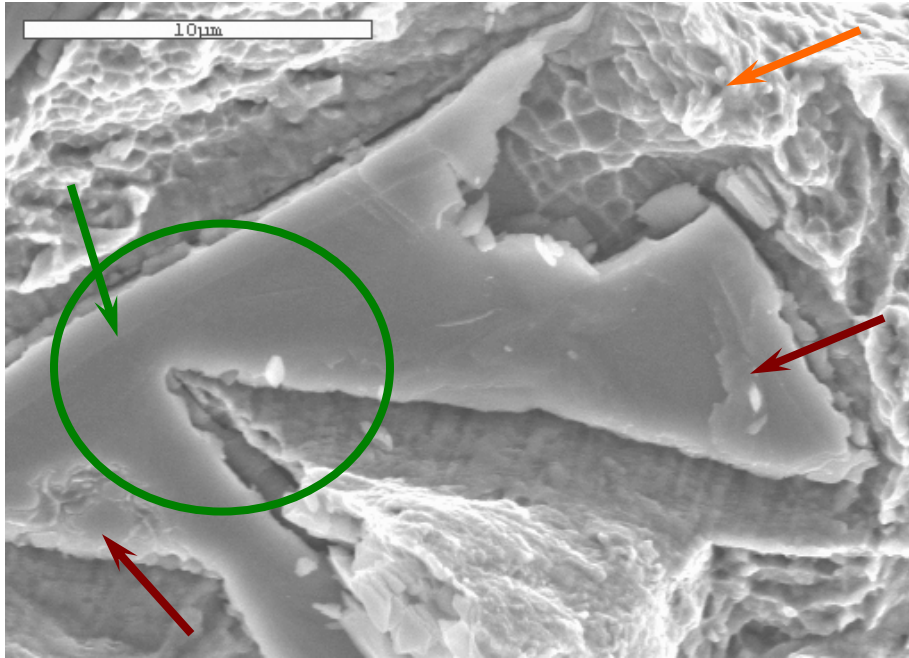


Figure 3-19. Fracture Surface of Tensile Sample (*40-1; Modification III*) at 5000x.

The area identified by the orange arrow is evidence of the dimples and microvoids typical of ductile failure, but it can be seen that this makes up a very small portion of the surface.

The features of the carbide – the large structure in Figure 3-19 – raised some question as to whether or not the carbide was indeed cleaved in the fracture process. The very fine features evident in the carbide – shown by the dark red arrows in Figure 3-19 – indicate that these areas were not cleaved, and that the original morphology had been maintained in these areas.

Conversely, the smooth, featureless area – shown by the green arrow and circle in Figure 3-19 – indicates that the carbide was fractured. It was determined that the carbide was oriented such that the shearing took place on a plane where both features would be seen. This was confirmed by comparison with many other images of carbides on the fracture surfaces, and it was noted that the carbides were only cleaved in this manner in the lower temperature tensile samples.

The carbides on the surfaces of samples tested at higher temperatures exhibited no evidence of any kind of fracture – no smooth, featureless areas whatsoever. The features of these carbides appeared to be completely like that of the original morphology of the carbide as it was formed. Carbide morphology itself is not well understood, from a perspective of its effect on physical properties of the alloy. As such, this morphology became a point of interest during the evaluation of the creep samples, but that will be discussed later. An example of a fracture surface carbide from a test at 850°C can be seen in Figure 3-20 (*below*). The reasoning behind the determination of shearing at lower temperatures should make more sense when Figures 3-19 and 3-20 are compared and contrasted.

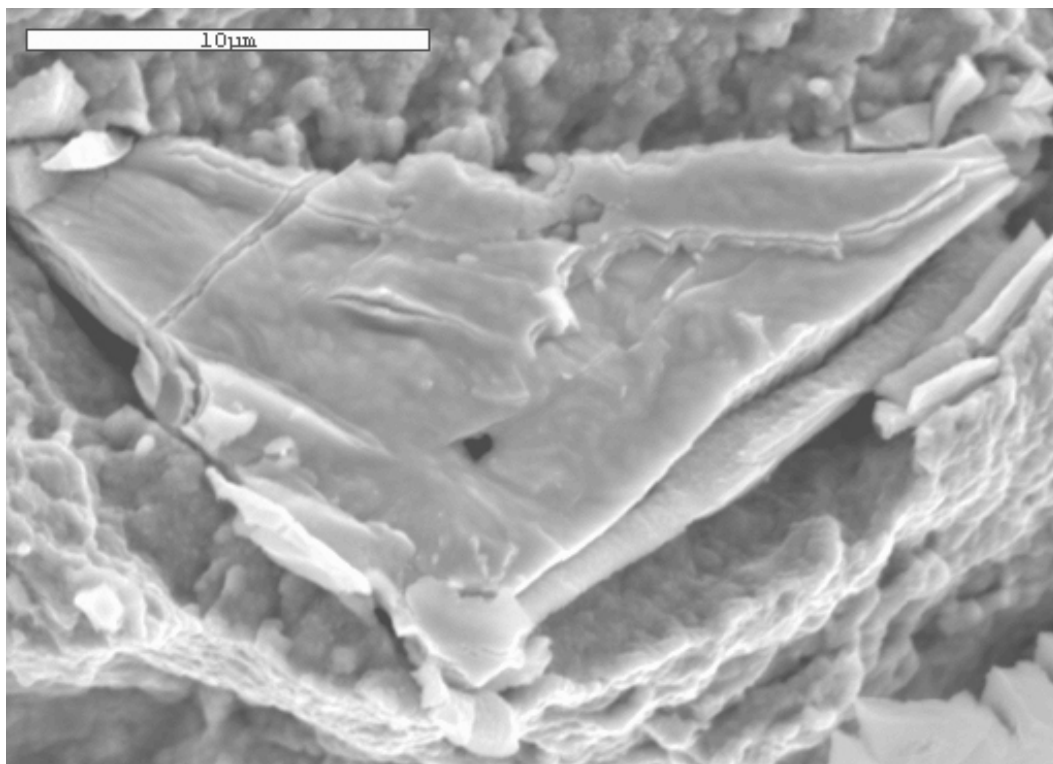


Figure 3-20. Fracture Surface of Tensile Sample (24-1; *Modification II*) at 5000x.

From images such as these, what is known about these higher temperature samples is that the fracture propagated in such a manner that it bypassed the carbides, rather than fracturing them.

Another feature was noted in similar fashion, but this feature occurred on a much less frequent basis: on some samples, it was observed that the carbides appeared to have been ‘ripped’ away from the surrounding matrix. An example can be seen in Figure 3-21 (*below*):

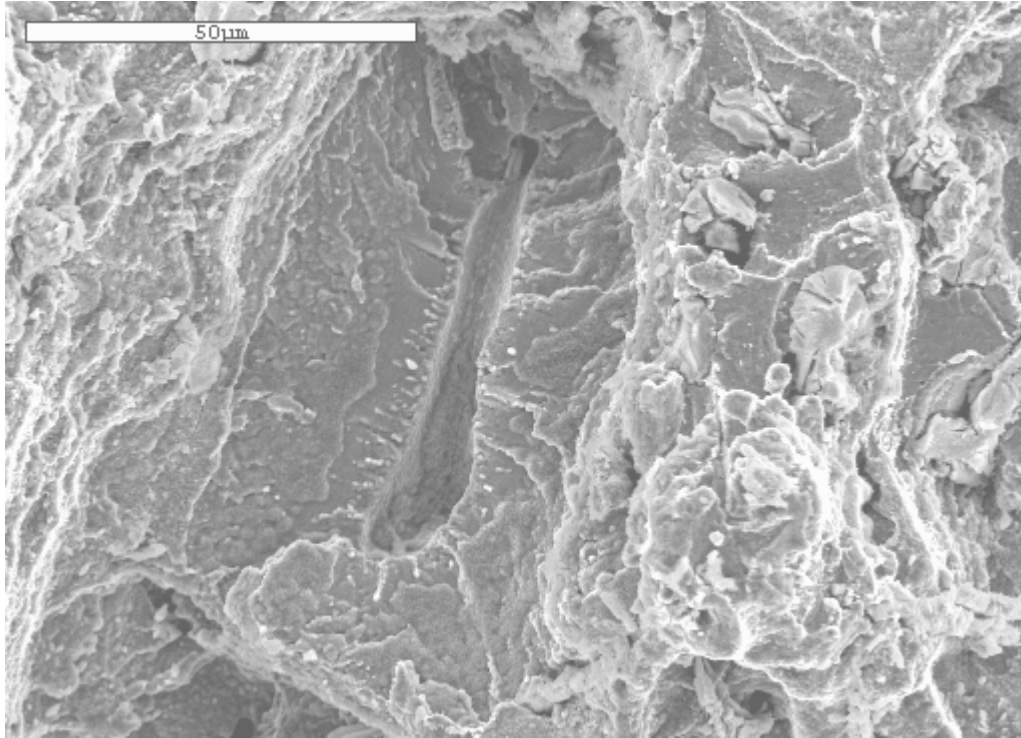


Figure 3-21. Fracture Surface of Creep Sample (*41-1; Modification III*) at 1000x.

It stands to reason that if there are many carbides apparent on a given surface that perhaps there are the residual cavities from such carbides on the opposing surface. Recall from the description in Chapter 2: these fracture surfaces all came from the ‘short’ end of the creep rupture sample. What can be gleaned from this is that it is possible that the surface of the ‘long’ end of the creep rupture samples exhibits the opposite of what is seen on these samples – a higher frequency of ‘ripped out’ carbide cavities and a lower frequency of carbides. However, from a failure analysis point of view, this offers little in the way of explanation of behavior, so it is pointed out here merely as observation.

Creep Samples

An example series of the creep sample fracture surfaces can be seen in Figure 3-22 (A-F) (*below*). An arrow is provided on the 25x image to show the location of the other micrographs.

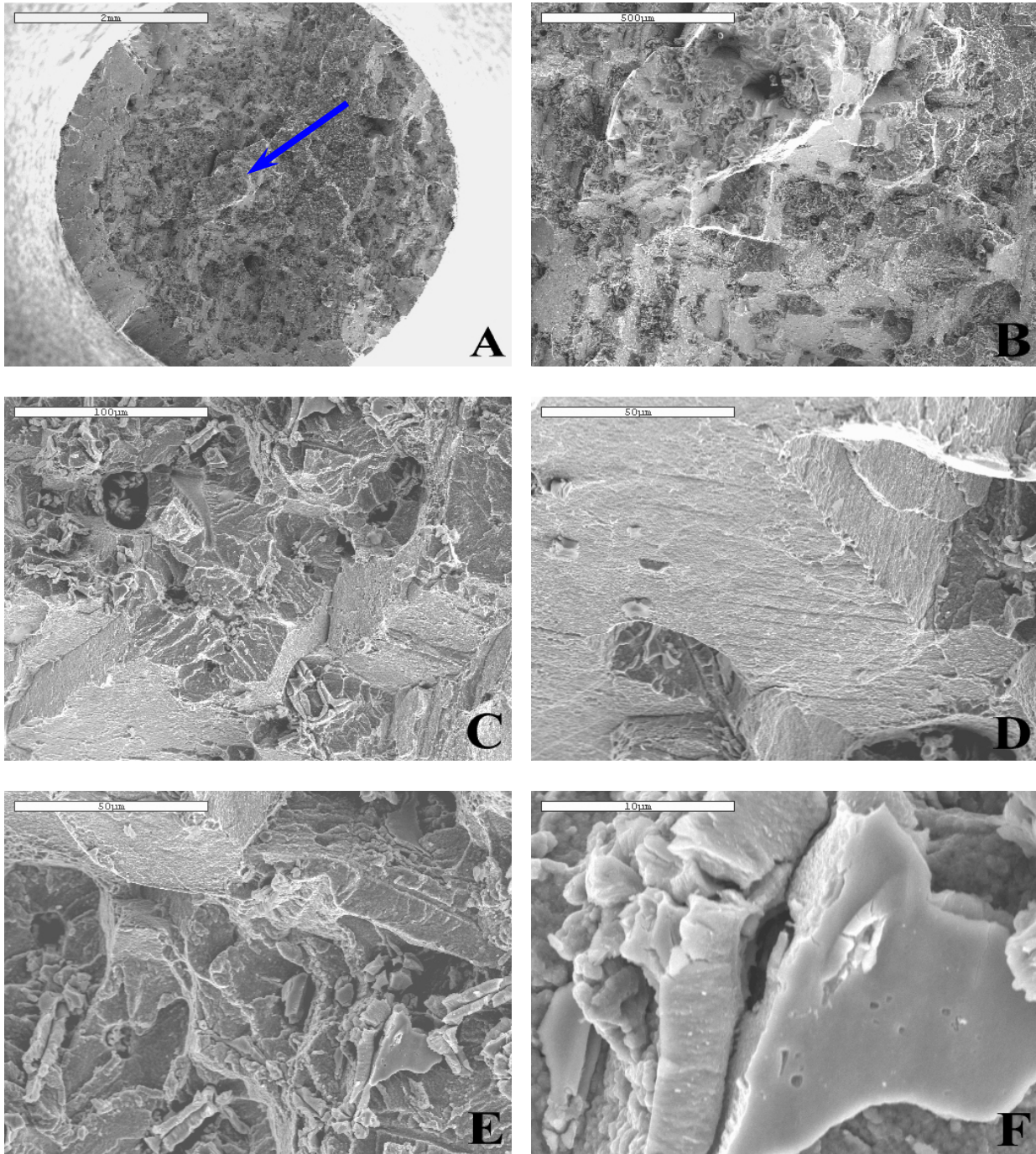


Figure 3-22. Fracture Surface of Creep Sample (39-2; *Modification III*) at A) 25x B) 100x C) 500x D) 1000x E) 1000x F) 5000x.

The features observed in the fractographic characterization of the creep samples were similar to those seen in the tensile samples. These will be discussed in greater detail later, but in general, the fracture surfaces of the creep samples exhibit the following:

- All surfaces contained mixed character deformation – a combination of cleavage-like fracture with some areas of more ductile-type deformation. There was no consistent quantitative split between the percent cleavage-like vs. the percent ductile areas. The ductile-type deformation was clearly dominant, on the order of at least 70%, and often more.
- In some samples, casting porosity and voids were again noted, and it again appeared that these features had little effect on the character of the surrounding fracture area.
- Surfaces exhibited two kinds of carbide structures. Virtually none of the carbides had been cleaved through as the fracture occurred, but nearly all remained intact on the surface. Similar to the tensile samples with such structures, there was evidence that some appeared to have been ‘ripped free’ from the surrounding γ/γ' material.
- These carbides were again of the MC type. No secondary carbides were noted, as expected. EDS indicates a high level of Ta and Ti in the carbide, whereas the surrounding material has increased levels of Ni, Cr and Co. Representative EDS spectra of the features shown in Figure 3-22 (F) can be seen in Figure 3-23 (A-B) (*following page*). A quantitative analysis of the two spectra is shown in Table 3-5 (*below*) for comparison.

Table 3-5. Quantitative Analysis of Features in Figure 3-22 (F)*.

Modification III alloy, Sample ID: 39-2							
Carbide				Surrounding area			
element	MW (g/mol)	Atomic % **	Weight % **	element	MW (g/mol)	Atomic % **	Weight % **
C	12.011	88.08	50.29	C	12.011	91.90	69.10
O	15.999	-----	-----	O	15.999	-----	-----
Al	26.982	-----	-----	Al	26.982	0.23	0.38
Ti	47.9	5.73	13.04	Ti	47.9	0.73	2.18
Cr	51.996	0.71	1.75	Cr	51.996	0.99	3.24
Co	58.933	0.50	1.41	Co	58.933	1.31	4.82
Ni	58.71	1.61	4.49	Ni	58.71	4.50	16.55
Mo	95.94	-----	-----	Mo	95.94	-----	-----
Ta	180.95	3.37	29.02	Ta	180.95	0.33	3.73
Total			100	Total			100

*Elements which are dominant in the EDS spectra of each feature are in bold.

**The Carbide scan was taken as a spot sample on the carbide itself. The Surrounding Area scan was taken for the entire area shown in Figure 3-22 (F). Values are shown to exhibit that there was a difference between the compositions of each area.

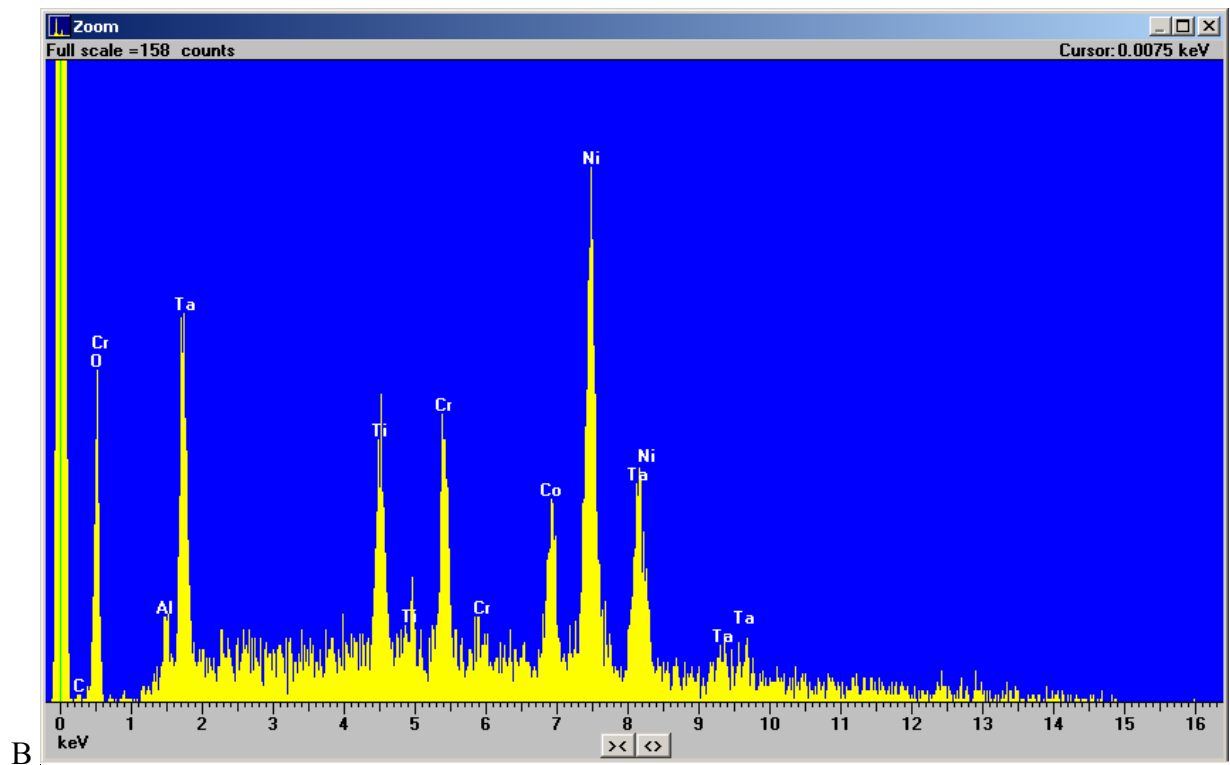
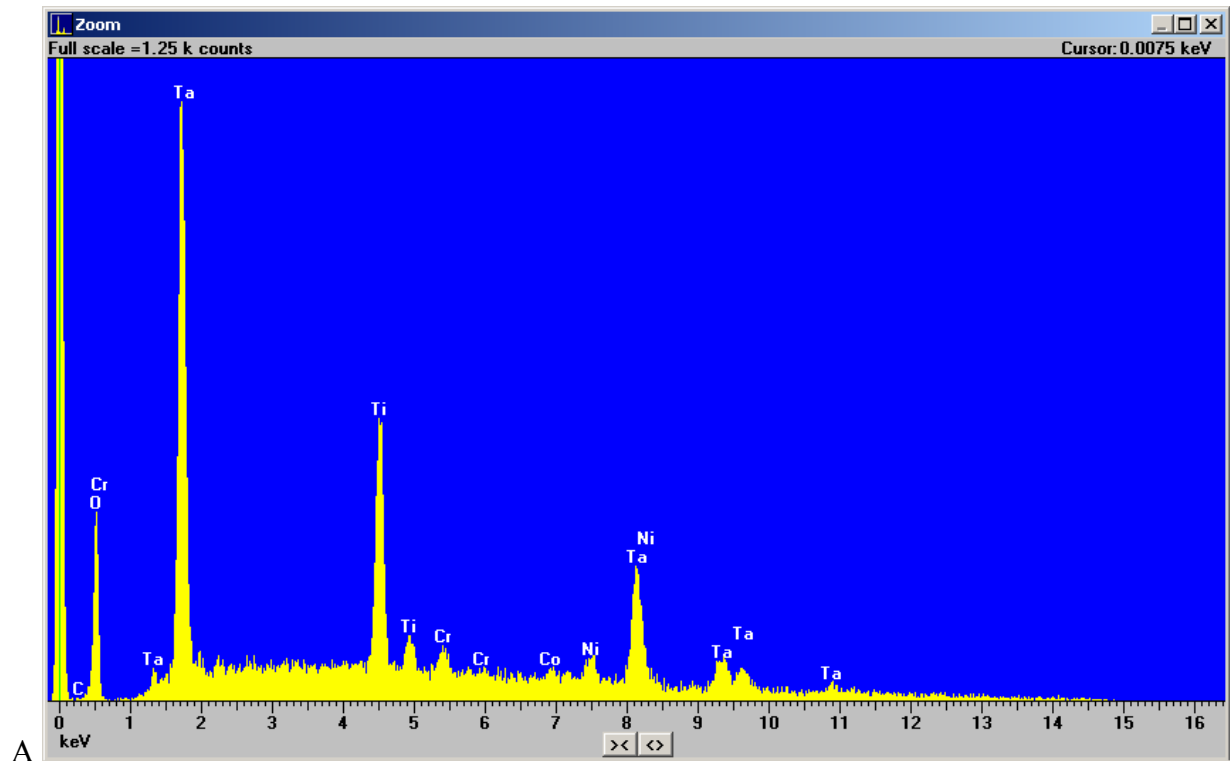


Figure 3-23. EDS Spectra of Sample 39-2 features: A) Carbide B) Surrounding Area.

While the quantitative analyses differ greatly between the creep sample and its tensile counterpart seen previously, the spectra shown in Figure 3-23 (A-B) indicate that the features nearly identical to those exhibited previously in Figure 3-16 (A-B). In fact, the spectra for the carbides in the two samples are nearly identical. Therefore it seems as though something in the area surrounding the carbide itself is what is causing the difference in oxygen concentration. The importance of this as it pertains to the material properties will be discussed further in Chapter 4.

Unlike the analysis results of the fracture surfaces from the tensile testing samples, no simple grouping of features exists, with few exceptions. The carbides which decorated these fracture surfaces were of the same type as those seen in those of the tensile samples – MC carbides only, with no instances of secondary carbides. In addition, no topologically closed-packed (TCP) structures were noted. For each carbide image taken at 5000x, an EDS spectrum was taken and analyzed quantitatively – 38 spectra for the creep sample surfaces alone. The resultant spectra could almost be superimposed upon one another with nearly no evidence of difference, and the same was true for the spectra taken of the areas surrounding each carbide. Ti and Ta were dominant in the composition of the carbides, and the surrounding areas had increased levels of Ni, Co and Cr, along with some quantities of Ti and Ta as well. It got to the point where the differences in composition from the spectra were more a function of the area fraction of carbide-to-surrounding-area than an indication of different carbides. This is not to say that there were no differences in carbide structure, but this will be discussed momentarily.

Examples of two different morphologies of carbides with their respective spectra are shown in Figures 3-24 (A-B) and 3-25 (A-B) (*following page*):

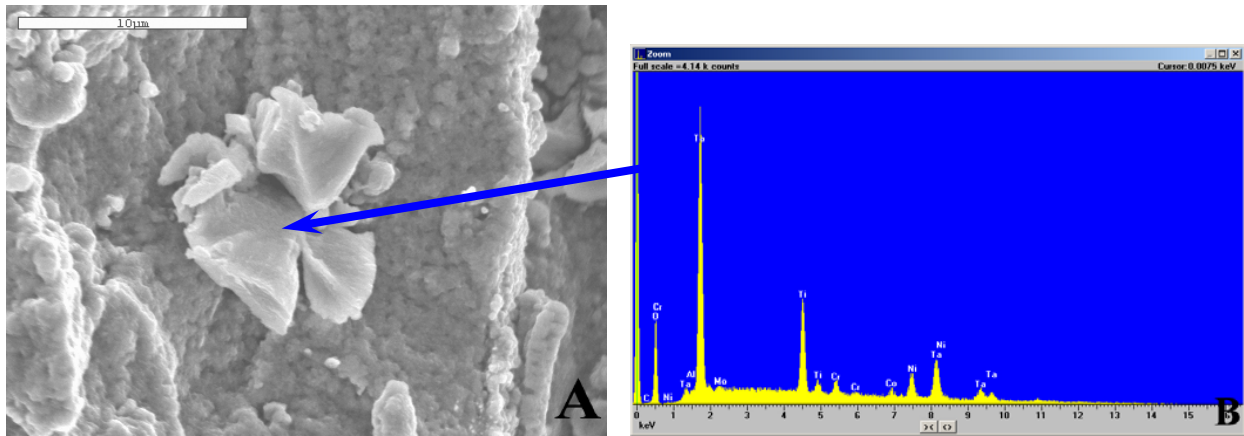


Figure 3-24. Carbide A) Morphology B) EDS Spectrum on Fracture Surface of Creep Sample (40-1; Modification III) at 5000x.

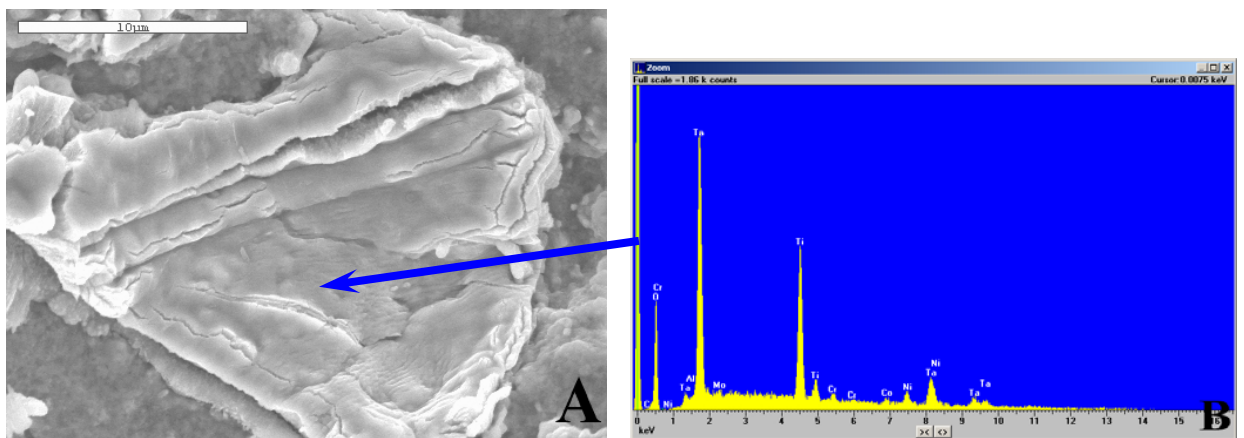


Figure 3-25. Carbide A) Morphology B) EDS Spectrum on Fracture Surface of Creep Sample (13-1; Modification I) at 5000x.

The spectra are small, and it is understood that the specific element identified by each peak may be difficult to see, but they are provided here for comparison rather than identification. The dominant peaks are as stated numerically in Tables 3-4 and 3-5, and as shown previously in Figures 3-16 (A) and 3-23 (A). From these figures alone, it is evident that composition has no noticeable effect on either size or morphology of these MC carbide particles. The latter morphology has been termed *script* or *script-like* in the literature, likely because of the appearance of its cross section – which, in this picture, would be normal to the page. The former morphology could also be described as script or script-like as a result of a 2D cross-section, but

will be referred to here as a *flowery* structure, due to the petal-like appearance which seems to sprout out of a central point. There were many such flowery carbides evident throughout the creep sample fracture surfaces, as was the case for the script carbides as well.

For the most part, the deformation character exhibited on these fracture surfaces were of two general types. First, there was evidence of areas of deformation which is dominated by cleavage-type fracture, as was previously shown in Figure 3-22 (E). Second, there was evidence of areas of a quasi-cleavage-type failure, with large, undulating surfaces like those shown in Figure 3-26 (*below*):

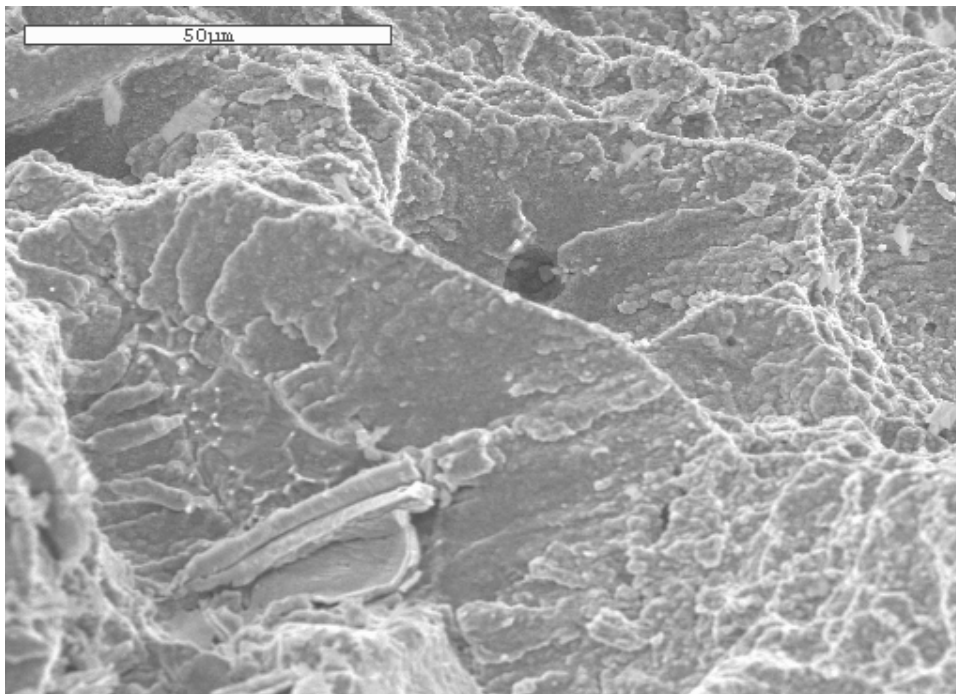


Figure 3-26. Fracture Surface of Creep Sample (40-2; *Modification III*) at 1000x.

Both of these types of surfaces had carbides scattered throughout – sometimes in clusters and sometimes not. Varied instances of casting porosity were evident on the surfaces, as shown in Figure 3-26 previously and again in Figure 3-27 (*following page*), but these appeared to have had little effect on the deformation of the surrounding area.

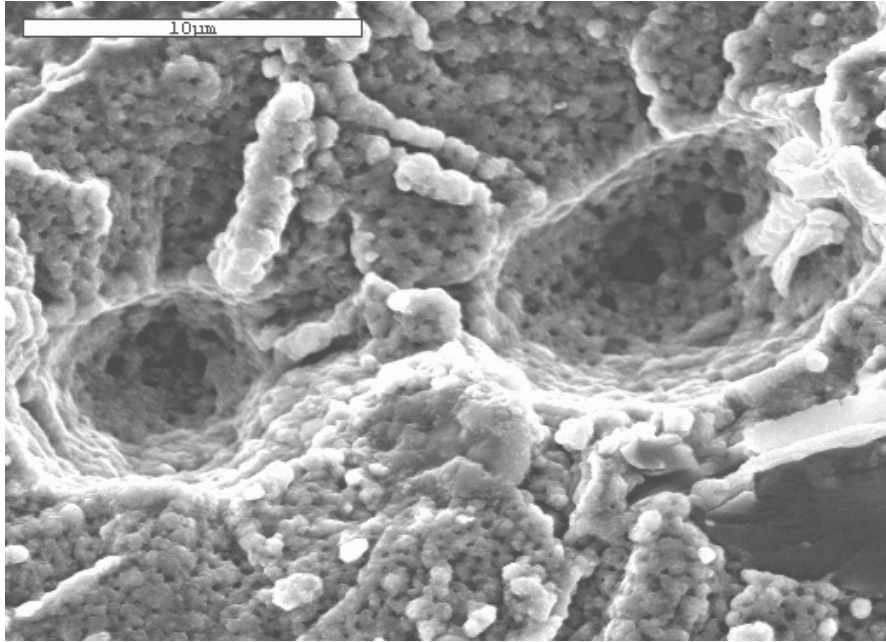


Figure 3-27. Casting Pores on Fracture Surface of Creep Sample (7-1; *Modification I*) at 5000x.

Cross-Section Analysis

Each of the samples tested in creep were mounted, sectioned, polished and etched such that an evaluation could be made on these cross-sections. The purpose of this analysis was to investigate possible microstructural differences which could help to explain the results of the creep testing itself. For this reason, the tensile samples were not analyzed, because the very short duration of the tensile tests as compared to the creep tests allow for little microstructural change to occur that is not associated directly with the deformation and fracture. Due to the much shorter duration of the tensile test, there is no reason to suspect that microstructural changes would occur, much less that any changes would affect the results of the tensile tests.

For the analysis of the creep samples, there were two methods used. As these differ slightly, they are described separately here.

Optical Imaging

The polished samples were analyzed optically using a LECO Neophot Model 21 microscope at 50x. Images were taken such that a portion of the sample – from the fracture

surface to approximately 3 mm (0.12 in) from the fracture surface – could be analyzed. To do this using the 50x magnification, a manual technique was used. This technique was borrowed from a commercially available software package. This type of software package has a function which controls a drive unit on the microscope stage such that a series of images can be taken at a given magnification and then ‘sewn-together’ to make a composite image. Performing this manually involved the use of the 4 individual images taken at the 50x magnification along with the standard Microsoft Paint program.

An example of this technique is shown in Figures 3-28 (*below*) and 3-29 (*following page*).

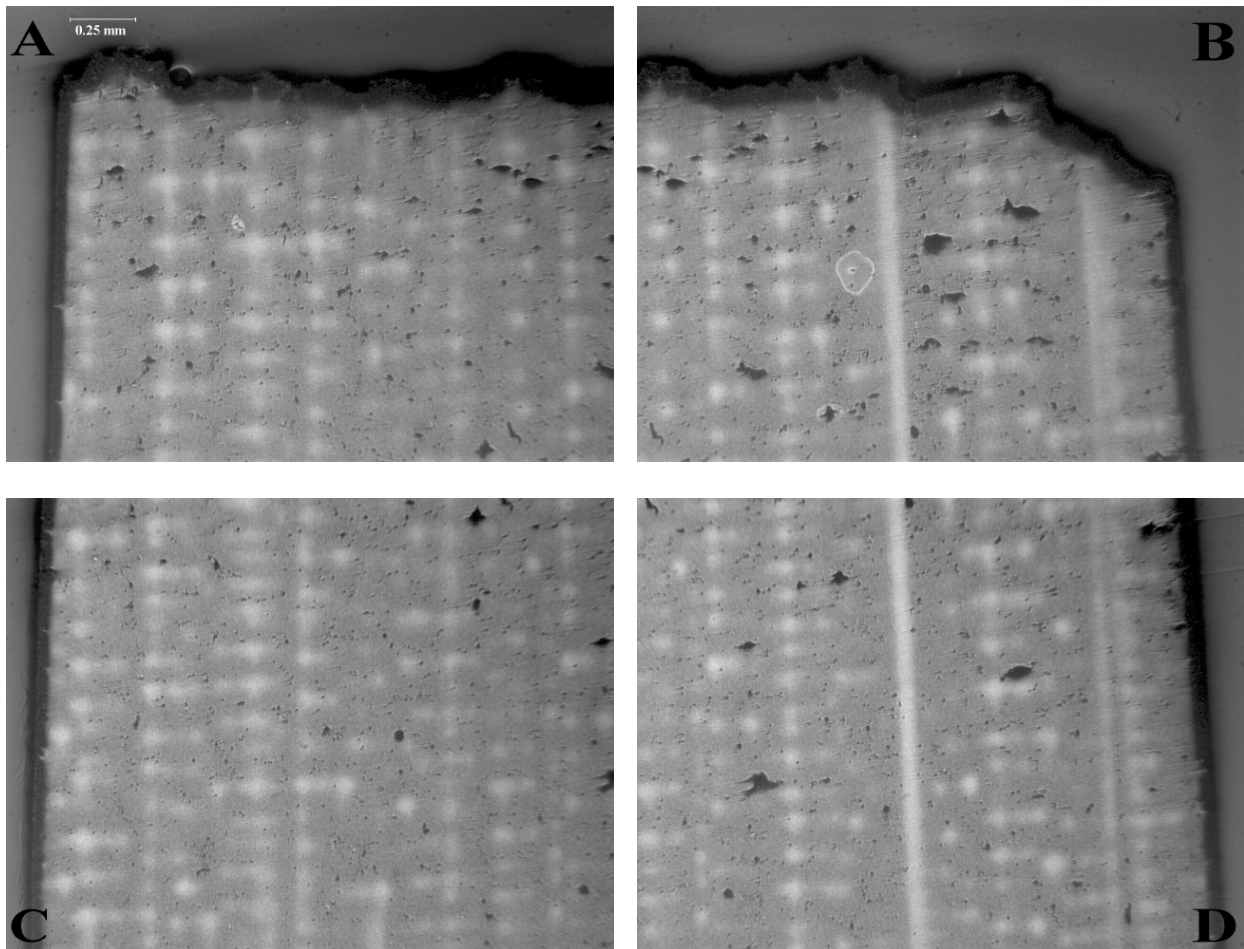


Figure 3-28. Cross-Section of Creep Sample (7-1; *Modification I*) A) Upper Left B) Upper Right C) Lower Left D) Lower Right.

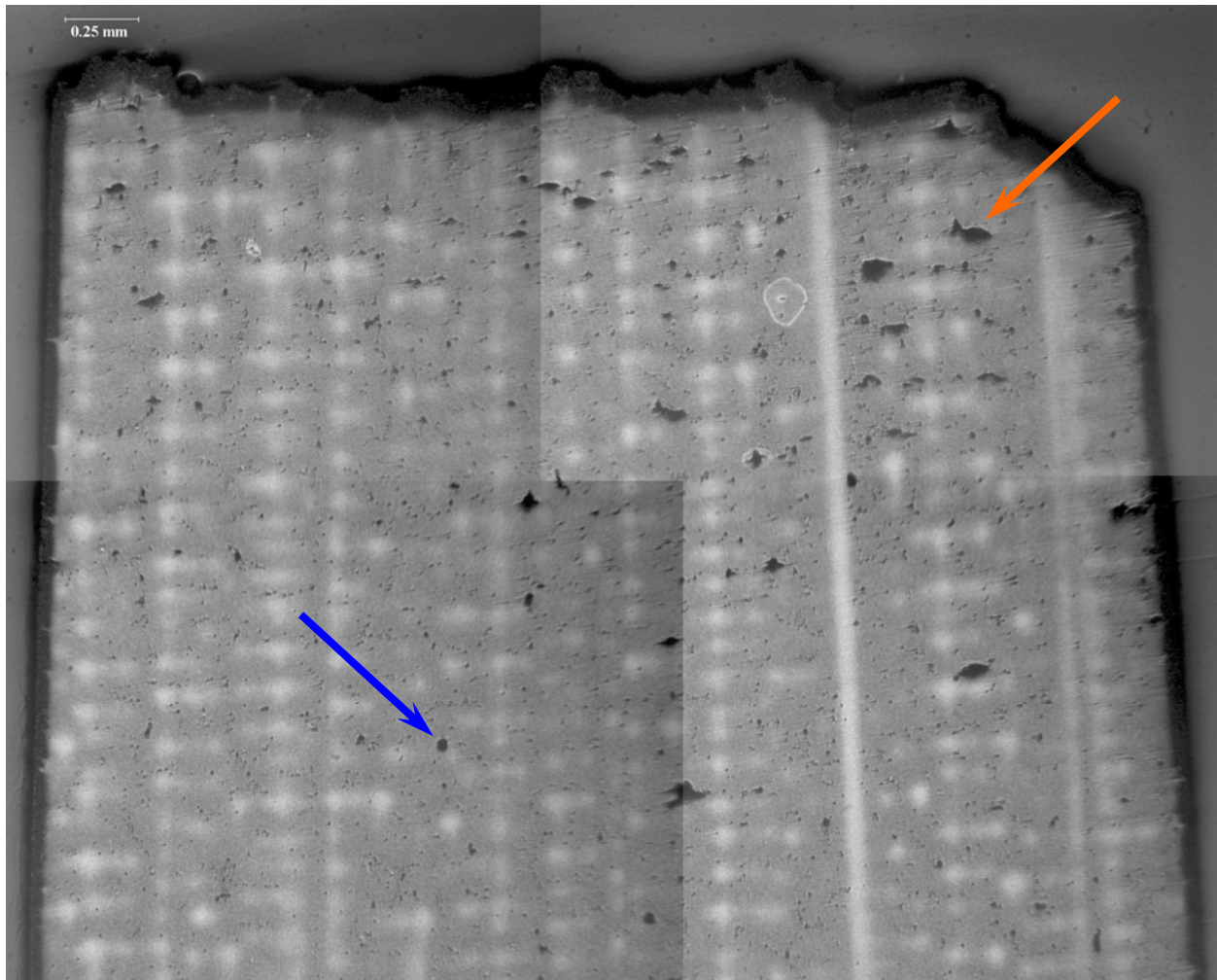


Figure 3-29. Composite Cross-Section of Creep Sample (7-1; Modification I).

This composite image is thus created with a better resolution than it would have if only one such image were taken of the entire sample, offering the ability to zoom in with standard imaging software for subsequent analysis. The usefulness of such a composite image is primarily for clarity in presentations and oral discussions. Rather than having to shift back and forth between several images, one image can be used and magnified as necessary to illustrate a point. However, the point intended to be illustrated by this particular set of optical analyses can be seen quite clearly even in this document.

First, it should be evident that there is some degree of casting porosity which exists in the sample. One instance of this is indicated by the blue arrow on Figure 3-29. This is seen to some degree in all of the samples. In addition, the existence of cracks – which have begun to develop – can be seen. An example of one is indicated by the orange arrow on Figure 3-29. These sub-surface cracks seem to occur frequently near the fracture surface itself. It should be noted that the fracture did not necessarily occur in the middle of the hot zone. While the influence of kinetic effects upon microstructure is certainly part of this study, no immediate inference may be made from these optical images alone.

The dendritic appearance of the cross-sections was first thought to be indicative of an incomplete heat treatment – or even worse, a heat treatment that was somehow inadvertently omitted prior to machining. Fortunately, all heat treatments were performed as designed, prior to machining, and the structure seen here is due to the nature of the residual carbides and carbide networks which are formed during solidification – specifically the Ta-rich MC carbides seen throughout the samples. A detailed discussion has been reported by Al-Jarba [22].

SEM Imaging

The SEM images of the cross-sections were taken much in the same manner as the SEM images previously taken for the fracture surfaces. The JEOL JSM 6400 SEM was utilized with an accelerating voltage of 15KV for all samples. One major difference was that – since the samples were mounted in epoxy – conductive carbon paint from SPI Supplies[®] was used to provide a conduction path from the sample to the SEM mounting hardware. This paint was applied along one edge of the sample, and as close as possible without touching the other edges so as to allow imaging to be accomplished right up to each remaining edge. The effect of charging prevented detailed imaging at the edges, but at lower magnifications, imaging was completed successfully with portions of the fracture surface itself included in the image.

As described in Chapter 2, a series of images were taken of these cross-sections in the following manner:

- Images at 200x to show the general character of the sample beneath the fracture surface, such as development of sub-surface cracks and concentration of carbides.
- Images at 1000x, 2500x and 5000x. An image at each of these magnifications was taken for the following points:
 - ✓ **F**: Just below the fracture surface along the vertical axis of the sample.
 - ✓ **C1**: 1 mm (0.04 in) below the fracture surface along the tensile axis.
 - ✓ **L1 & R1**: 1 mm (0.04 in) below the fracture surface at the left and right edges of the sample.
 - ✓ **C2**: 2 mm (0.08 in) below the fracture surface along the tensile axis.

This is illustrated in Figure 3-30 (*below*):

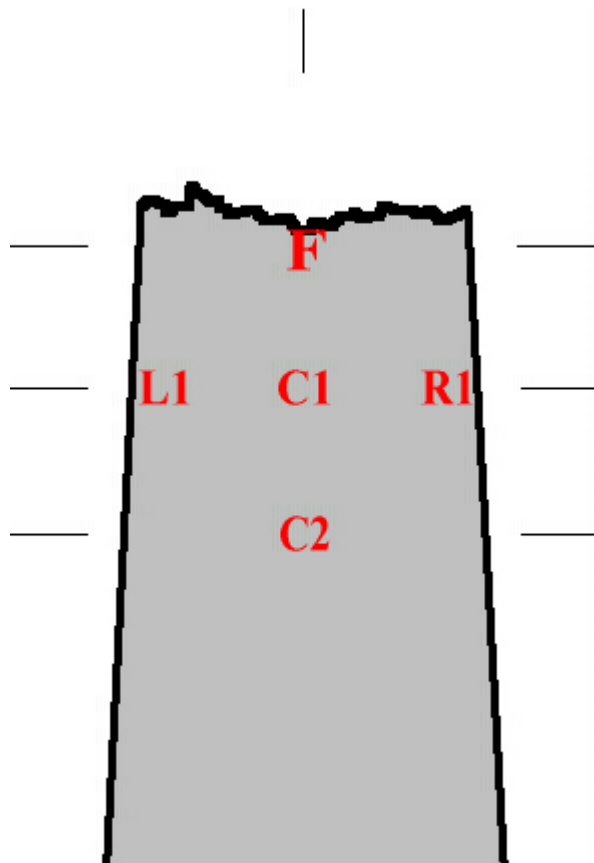


Figure 3-30. Imaging Points for SEM Analysis of Cross-Section Samples.

An example of one full set of these images is shown in Figure 3-31 (A-E) (*below*):

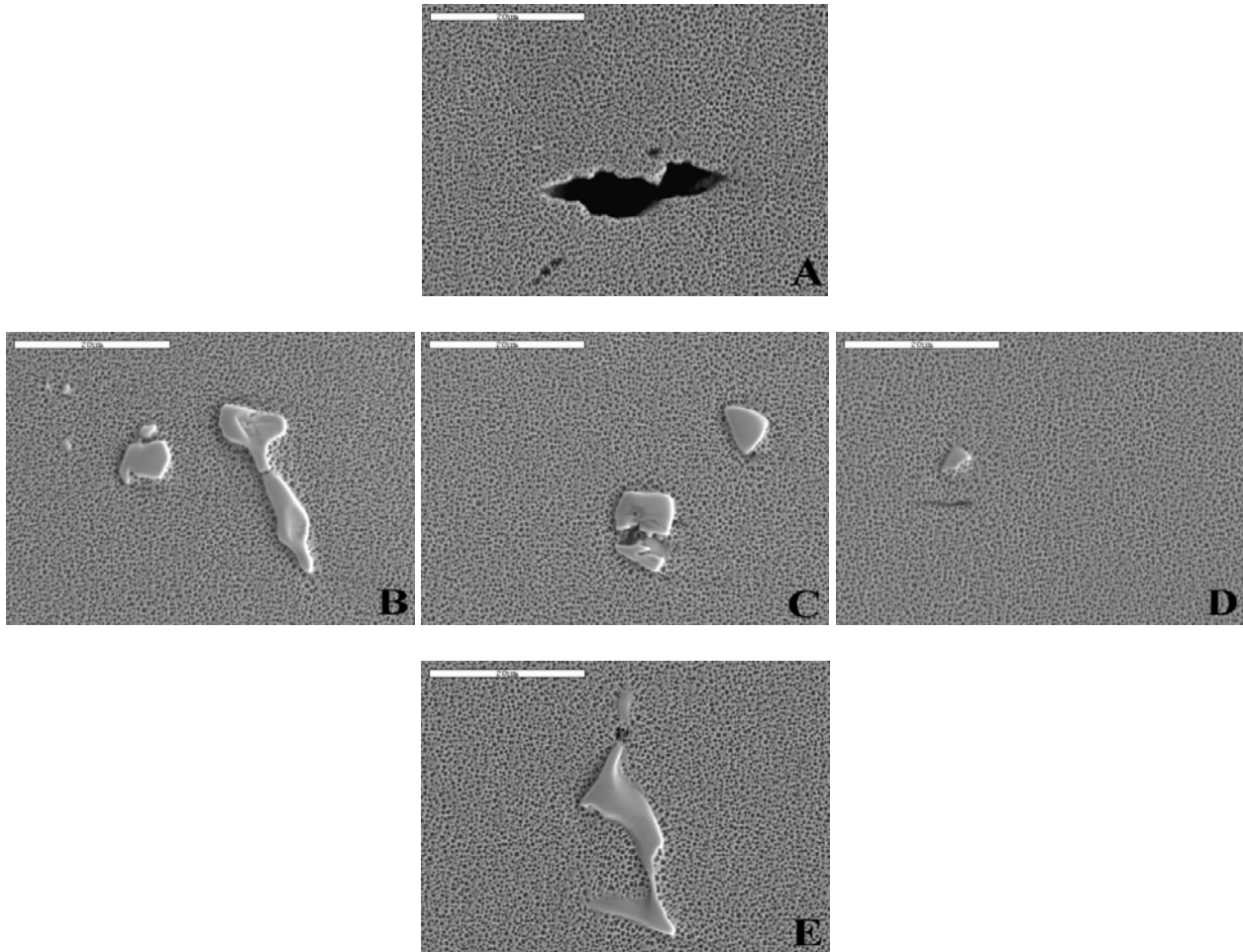


Figure 3-31. Imaging Points for Cross-Section of Creep Sample (7-1; *Modification I*) A) **F** B) **L1** C) **C1** D) **R1** E) **C2**.

This particular set of images was taken at original magnification of 2500x. This process was completed for every sample for all magnifications other than 200x, which was taken only once per sample.

The nature of this series approach with similar image points was to provide comparison not only between points on one sample, but between all samples. In this manner, every point was compared with the other 4 points on the sample, as well as each identical point on all other samples for the same original magnification. The results are discussed in detail in Chapter 4.

CHAPTER 4
DISCUSSION

Casting

Since the casting process is the one of the fundamental properties upon which the choice of alloy was based, it only makes sense to begin the discussion of results of this project with casting. While the casting data on the modified alloys is not extensive, what little exists has proven to be valuable, especially in light of data developed in other areas as the project continued. The results of the casting process evaluation are shown again in Table 4-1 (*below*):

Table 4-1. Defects found in cast alloy samples.

Alloy	Multi-grain	Sliver	Low-Angle Grain Boundary
Modification I	15 (<i>3 usable</i>)	0	0
Modification II	0	4 (<i>4 usable</i>)	0
Modification III	0	2 (<i>2 usable</i>)	2 (<i>2 usable</i>)
Modification I blade	Yes	No	No
Modification II blade	Yes	No	No
Modification III blade	No	No	Yes (<i>start</i>)

The goal of the project was to develop an alloy which would maintain the original properties of castability and corrosion resistance while improving upon the strength, such that it could be used in IGT applications. From the casting results, it is apparent that the Modification I alloy started out lagging the others where that goal was concerned. A 20% yield in casting would be considered low even by the standards of less-castable alloys, and this analysis doesn't even take into account other defects such as freckles, which would possibly decrease the yield even further. The fact that such a large number of samples from the Modification I alloy were rejected suggests that there is something in the composition itself that is causing the decreased castability.

Table 4-2. Compositions of Baseline and modified samples of PWA 1483*.

Alloy	Ni	Cr	Co	Mo	W	Re	Ta	Al	Ti	C
Baseline	Bal.	12.8	9.0	1.9	3.8	0.0	4.0	3.6	4.0	0.07
Mod I	Bal.	12.5	9.0	1.9	3.8	0.0	6.2	4.6	2.5	0.07
Mod II	Bal.	10.0	12.0	0.6	4.9	3.0	3.9	3.5	3.9	0.07
Mod III	Bal.	10.0	12.0	0.6	4.9	3.0	6.0	4.5	2.4	0.07

*Elements with adjusted levels from Baseline are shown in bold. All values in weight %.

Revisiting the compositional differences between each alloy – provided again in Table 4-2 (*above*) for convenience – the following reasoning applies:

- The addition of the γ' formers (Ta, Al, Ti) has resulted in the development of multi-grain defects in every Modification I sample.
- Additions of these γ' formers were made in almost identical quantities to the Modification III alloy, which had no incidence of multi-grain defects.
- The Modification II alloy bars also exhibited no incidence of multi-grain defects, but it did exhibit sliver defects. It did not have the raised level of γ' formers. It did have increased levels of solid solution strengtheners (Re, W) and an increased level of microstructural stabilizers (Co).
- The Modification III alloy also had these increased levels of Re, W and Co.

The conclusion which can be made is that the γ' formers are adversely affecting the single crystal solidification process – more than likely by affecting the nucleation process at areas of the mold with rapidly-changing dimensions, which then interrupts existing single crystal grain growth with the growth of new grains. The structural stabilizer (Co) offsets this effect and decreases segregation [25,26], somehow suppressing the nucleation of new grains as the growth process continues. It is possible that the solid solution strengtheners are also contributing to the suppression of nucleated grains by thermo-solutal convection. In general, the data suggests that the types and amounts of additions associated with each alloy have some influence over the type and frequency of defects which occur. This is to be expected, and further discussion regarding such effects is certainly of interest at some point for future development of the alloy. Finally,

with the limited amount of data, these few conclusions should be considered a starting point for comparison in future work.

Mechanical Testing

In this work, the goal was to develop an alloy of higher creep strength than its baseline counterpart for the temperatures being tested – temperatures which mimic those expected in IGT applications. To that end, it was not just the rupture strength which is important, but the entire behavior of the alloy to each set of conditions. Alloy modifications were intended to result in an alloy which undergoes a limited amount of primary creep, has a relatively low and long-lasting minimum creep rate and a long rupture life. As such, each of these will be assessed as part of the discussion of the mechanical properties of the modified alloys.

Tensile Testing

The focus of this project was on the improvement of creep strength, and so the majority of the samples were dedicated to that purpose. But it was deemed important to establish a set of tensile data as well, not just as a comparison to existing data, but also as a benchmark for comparison between the properties and behavior of the modified alloys. Due to the limited number of Baseline and Modification I samples, the majority of this testing was performed on the Modification II and III alloys with similar results.

The tensile testing indicated the following:

- At RT, all three alloys (Modifications I, II and III) were of comparable YS, UTS and ductility. Modification I had the highest UTS, while Modification III had the highest YS and ductility.
- At 750°C, 850°C and 950°C, the Modification II and III alloys were again of comparable YS and UTS, but the ductility of the Modification III alloy was far superior to that observed in the Modification II alloy. In each of these tests, both alloys exhibited similar behavior: an elastic region, followed by a moderate to large degree of work hardening, followed by a dropoff in strength prior to failure – an indication of necking, evidenced not only on the stress-strain curves, but on the samples as well.

- At 750°C, 850°C and 950°C, the Modification II and III alloys exhibited an inflection point along the elastic portion of the curve, possibly indicating some sort of change in deformation mechanism at that point. The root cause of that mechanism change remained somewhat a mystery, but is discussed further in the Imaging section later on.
- The Baseline alloy was not tested, but results for the other three alloys indicated a comparable value to existing data, if not a slight improvement in some cases.

Creep Testing

Analysis of the creep results was divided into three essential portions: primary creep behavior, length of time spent in secondary creep and finally rupture life. Creep testing was performed at the same temperatures as were used for tensile testing (750°C, 850°C, 950°C). In general, an alloy for an IGT application must take into account the first and third of these as critical design criteria. Clearly, designing a blade which exceeded the close tolerances in the engine after only a relatively short time would not be prudent. Similarly, it would be a waste of time to design a blade which remained within those tolerances for its entire lifetime, but only lasted a few hours under those conditions.

At 750°C, all three modified alloys were less creep resistant where primary creep was concerned. While the Modification I and II alloys did exhibit about the same quantity of primary creep, they did so in less time than the Baseline alloy. However, this time difference was only a few hours. But the improvement of the Modification I and II alloys was in their rupture lifetimes, both of which were more than double that of the Baseline. The Modification III alloy was significantly stronger than the other alloys, exhibiting close to a 3x increase in the amount of primary creep as compared to the other alloys, but also showing a longer rupture lifetime and a much lower rate of secondary creep than the Modification I and II alloys. The second set of tests – under lower stress at 750°C, on just the Modification II and III alloys – revealed similar results, although in this case, the Modification III alloy had a significantly longer rupture life than did the Modification II alloy.

However, at 850°C and 950°C, the Modification II and III alloys exceeded the Baseline and Modification I alloys in all testing. This was not as pronounced in the primary creep values as it was in the rupture lifetimes. Taking the creep behavior into account – along with the knowledge that Modification I seems to be problematic at best for casting purposes – it is obvious that if the Modification I alloy is to be developed further, then additional alloying modifications should be considered.

Characterization

To gain a better understanding of the results of the mechanical testing, it was necessary to investigate the microstructure of each sample. Through this process, a much better assessment could be made of each alloy – not just from a performance standpoint, but from a compositional and structural perspective as well.

Fracture Surface Analysis

The fracture surfaces of all the samples mechanically tested were analyzed by SEM at 25x, 100x, 500x, 1000x, and 5000x. The 25x images were taken to show the general character of the surface, while the remaining images were taken as comparison points between the various samples. Although some features were seen that were common to both types of mechanical test, the emphasis was on making a correlation to the results from the mechanical tests. As such, the comparisons are limited to each type of testing, i.e.: tensile to tensile and creep to creep.

Tensile Samples

Carbides found on the fracture surfaces of the tensile samples were sheared or otherwise fractured in some manner. Unfortunately, the shearing of the carbides provides little in the way of explanation of the behavior of these alloys. Carbides are generally thought of as strong, brittle particles that afford little in the way of strengthening, but rather act as crack initiation and propagation sites. The results of this study appear to indicate similar behavior.

These higher temperature tensile tests were marked by a milder yield point, followed by what appeared to be an immediate work hardening, and then a dropoff in strength until failure. This smooth yield point was previously referred to as an inflection point on the elastic portion of the curve. One possible explanation for this is that the inflection point indicates some change in elastic behavior, rather than strictly a work-hardening mechanism.

A work-hardening condition is generally exhibited by a curved appearance in the stress-strain curve after yielding, but these inflection points connect two portions of the curve which appear quite linear – indicating a possible change in modulus. The carbides are strong, but have limited ability to withstand elastic strain. When the strain reaches a critical value, the carbides fracture and the modulus of the material becomes strictly that of the γ/γ' structure with little or no influence from the carbides themselves. The inflection points occurred at nearly the same strain value, but with differing stress values, further promoting this theory.

There is some work hardening which occurs at higher temperatures due to the increase in YS of the γ' precipitates, but it is difficult to determine the exact point on the stress-strain curves where this begins to have a noticeable effect. It is possible that some combination of the two mechanisms – carbide fracture resulting in lower bulk modulus and increased YS of the γ' precipitates resulting in more work hardening – are occurring concurrently. This has not been studied previously and therefore merits further investigation.

There is information in the literature that the decrease in strength seen in such high temperature tests is due to the interruption of dislocation networks by various precipitated particles throughout the microstructure [27]. This – along with the necking exhibited on the samples themselves – serves as a good explanation for the post-UTS behavior of the high-temperature samples.

Creep Samples

The importance of the carbides was not so much in their individual appearance, but rather the way that they interacted with the surrounding matrix leading up to and during the failure itself. Given the features on the surface, it seems evident that the path of the cracks went around such carbides, as absolutely no sheared carbides were found on any creep sample fracture surface.

However, there were many instances of carbide clusters found near cleavage surfaces, as seen in Figure 4-1 (*below*).

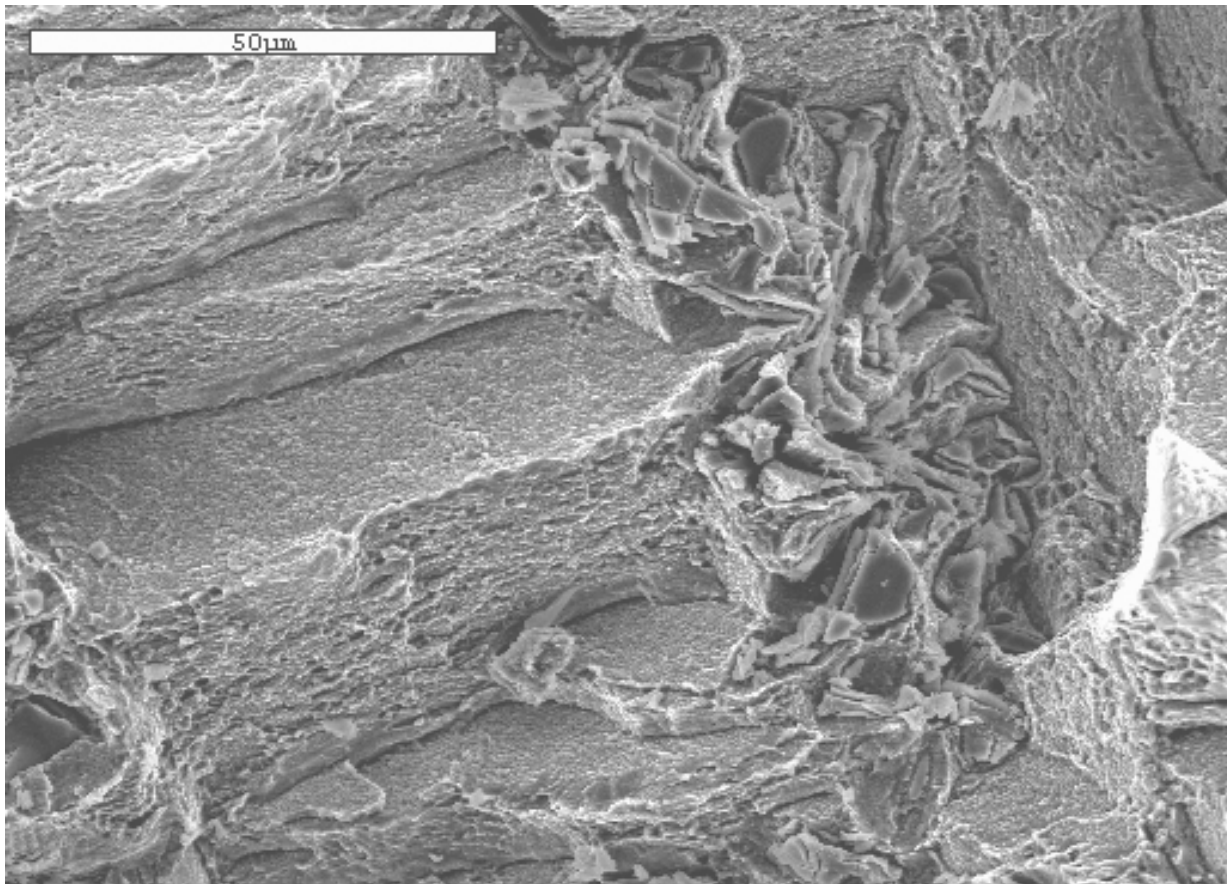


Figure 4-1. Fracture Surface of Creep Sample (7-1; *Modification II*) at 1000x.

The incidence of these carbide clusters seemed to indicate that they were indeed acting as crack propagation or initiation sites, as reported in the literature [28,29]. Again, because this was the

case to a lesser or greater degree for every creep sample fracture surface, it did not help resolve any behavioral differences either.

The incidence of cavities (Figure 3-21) gives a good indication of the way that the carbide separated from the surface. Higher magnification images in Figure 4-2 (A-B) (*below*) provide useful information on the mechanism of the carbides separating from the matrix.

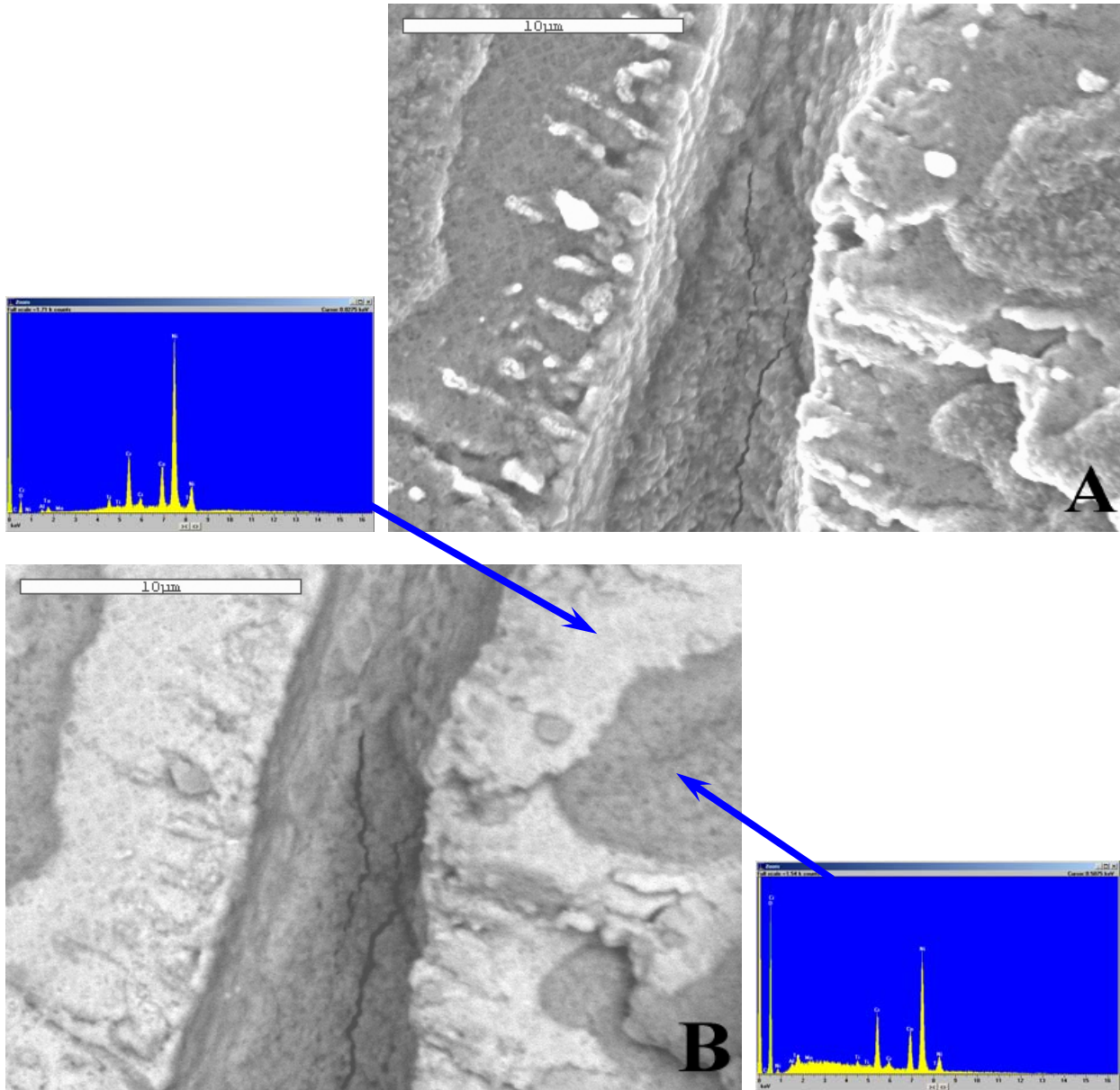


Figure 4-2. A) SE B) BSE Image of Carbide Cavity on Fracture Surface of Creep Sample (41-1; *Modification III*) at 5000x.

The spectra associated with the ‘white’ and ‘gray’ areas on the BSE image do not appear to be very different from one another, especially at the size presented here. But the quantitative analysis shown in Table 4-3 (*below*) indicates that there is a difference.

Table 4-3. Quantitative Analysis of Features in Figure 4-2 (B)*.

Modification III alloy, Sample ID: 41-1							
‘White’ area				‘Gray’ area			
element	MW (g/mol)	Atomic %	Weight %	element	MW (g/mol)	Atomic %	Weight %
C	12.011	67.55	30.10	C	12.011	18.26	6.79
O	15.999	-----	-----	O	15.999	41.16	20.38
Al	26.982	0.15	0.15	Al	26.982	0.39	0.33
Ti	47.9	0.42	0.74	Ti	47.9	0.37	0.55
Cr	51.996	3.04	5.86	Cr	51.996	5.25	8.45
Co	58.933	4.84	10.58	Co	58.933	7.70	14.05
Ni	58.71	23.95	52.17	Ni	58.71	26.65	48.43
Mo	95.94	0.00	0.00	Mo	95.94	0.08	0.24
Ta	180.95	0.06	0.41	Ta	180.95	0.14	0.78
Total			100	Total			100

*Elements which are dominant in the EDS spectra of each feature are in bold.

The first thing which should be noted is that the oxygen Ka peak is so close to the Cr La peak that these often appear to be the same peak on the EDS spectra. But the quantitative analysis shows that there is actually some difference in oxygen concentration between the two areas. The existence of oxygen seems unlikely to have occurred during the casting process or the heat treatments since these were conducted under vacuum conditions, so this is probably the result of interaction with the air around the sample just after failure while the sample was cooling from the 750°C test temperature. This is, after all, one of the key reasons for the addition of Cr to such alloys in the first place – to promote the formation of a protective Cr₂O₃ layer on the surface of the alloy at high temperatures. With only the slight difference in Cr levels, it is impossible to explain why this reaction might have occurred in one area and not the other.

Even without further data, the difference speaks to the possible impact on the carbide separation mechanism. Oxides tend to be very brittle, and as such, if the white area – the area which seems to make up the majority of the surface adjacent to where the carbide was – had been oxide, it would stand to reason that this region fractured at lower strain, exposing the material earlier in the test. However, it is the gray area which is high in oxygen content, not the white, so regardless of when the oxide formed, it is unlikely that it had anything to do with the separation.

What does seem to point directly to the mechanism is the existence of microcracks seen in the cavity itself. These cracks appear to have preferentially formed in the area of the cavity, as they are not seen anywhere else in the images. It is likely that these microcracks propagated in the area near the carbide and that when they reached the carbide, they propagated either through or around the carbide (or both). The carbide more free and had less connection to the surrounding matrix. The fact that the cavity contains very detailed features indicates that there could not have been a strong bond between the carbide and the surrounding matrix in the first place. As further proof of this, the detailed features of the cavity do not seem to match the morphology of the carbides seen in previous images. Using all of this information, the conclusion was made that it was unlikely that this carbide separation had much of an effect on the behavior of the alloys.

The detailed features of the carbides did bear some further investigation in the SEM analysis of the fracture surfaces. The flowery carbides were such that detailed features were unlikely a foundation for any kind of explanation of creep behavior or failure mechanism, but the features seen on the script carbides were of more interest. In addition, it was originally thought that some carbides were of a third type – referred to as *stringers* or *stringer carbides*.

The reasoning for the choice of nomenclature should be clear from Figure 4-3 (*below*):

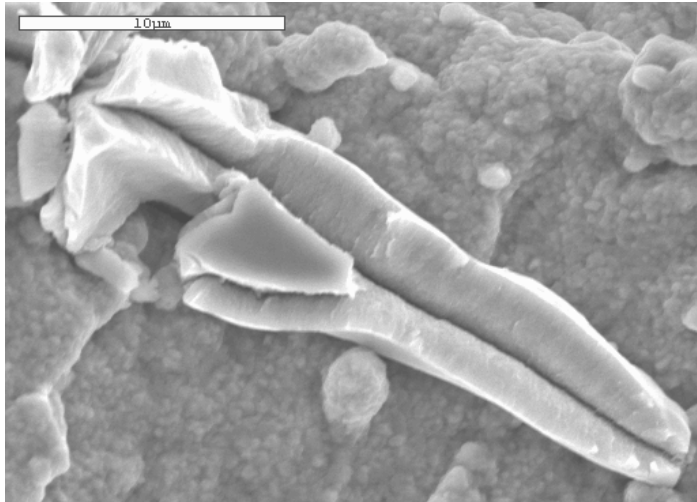


Figure 4-3. *Stringer Carbide on Surface of Creep Sample (12-1; Modification II) at 5000x.*

Carbides with this appearance were evident on every fracture surface analyzed, but it was not until certain views of the script carbides were seen that it was determined that all of these carbides were script carbides. One such view of the script carbide is shown in Figure 4-4 (*below*):

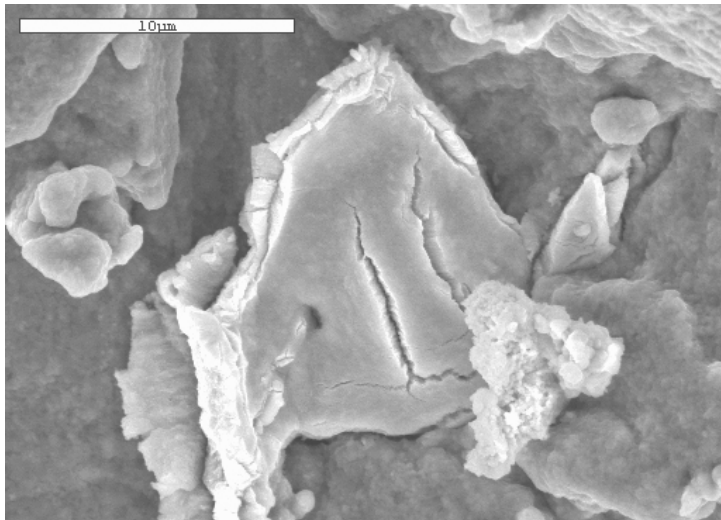


Figure 4-4. *Script Carbide on Surface of Creep Sample (43-1; Modification III) at 5000x.*

The edges of the script carbide shown in Figure 4-4 closely resemble those seen in the stringer carbide seen in Figure 4-3. Reviewing the images of both types, it was determined that

these so-called stringer carbides are likely also script carbides, viewed from a different perspective.

The reason this came to light is because there was an attempt to make a correlation between the appearance of these carbide edges with possible failure mechanisms. One such postulation was that the failures were initiated in the carbides. It was thought that this occurred by the delamination of the carbides along a path parallel to their sheet-like faces. The cracks which are seen on face of the carbide in Figure 4-4 indicate that this is unlikely the case, and that the appearance of the edges is simply one of original morphology. The cracks on the carbide face were of some interest as well. It was noted that these cracks developed in carbides like these on all of the surfaces, but that the morphology was more developed in those seen from higher temperature tests. A comparison between these can be seen in Figure 4-5 (A-B) (*below*):

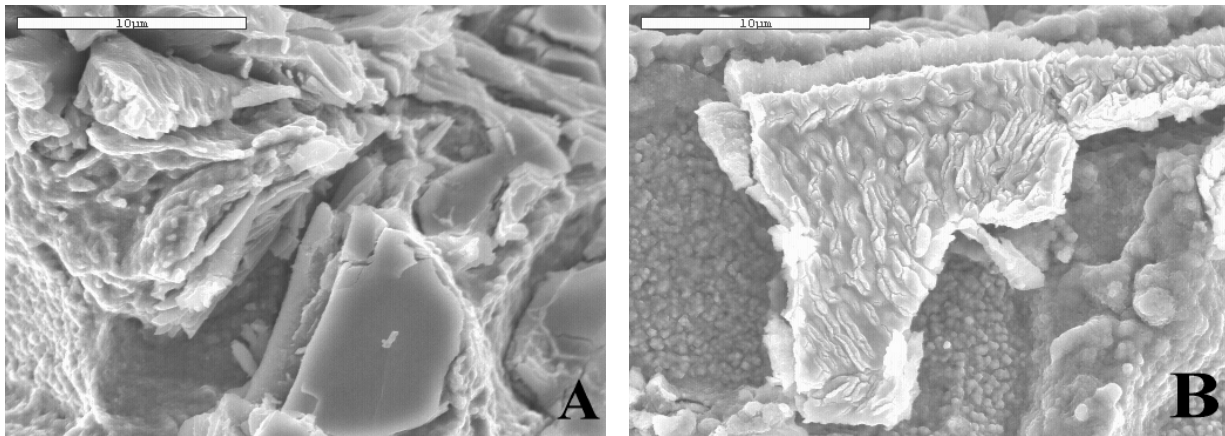


Figure 4-5. Carbide Surface Morphology for A) 750°C Creep Test (7-1; *Modification I*) B) 950°C Creep Test (26-1; *Modification II*).

The small, bumpy features to the left and right of the carbide in Figure 4-5 (B) are likely fine γ' precipitates which have coarsened due to the temperature. The nature of the cracks seen on the faces of these carbides – like those in Figure 4-5 (B) – remains a question which needs further investigation.

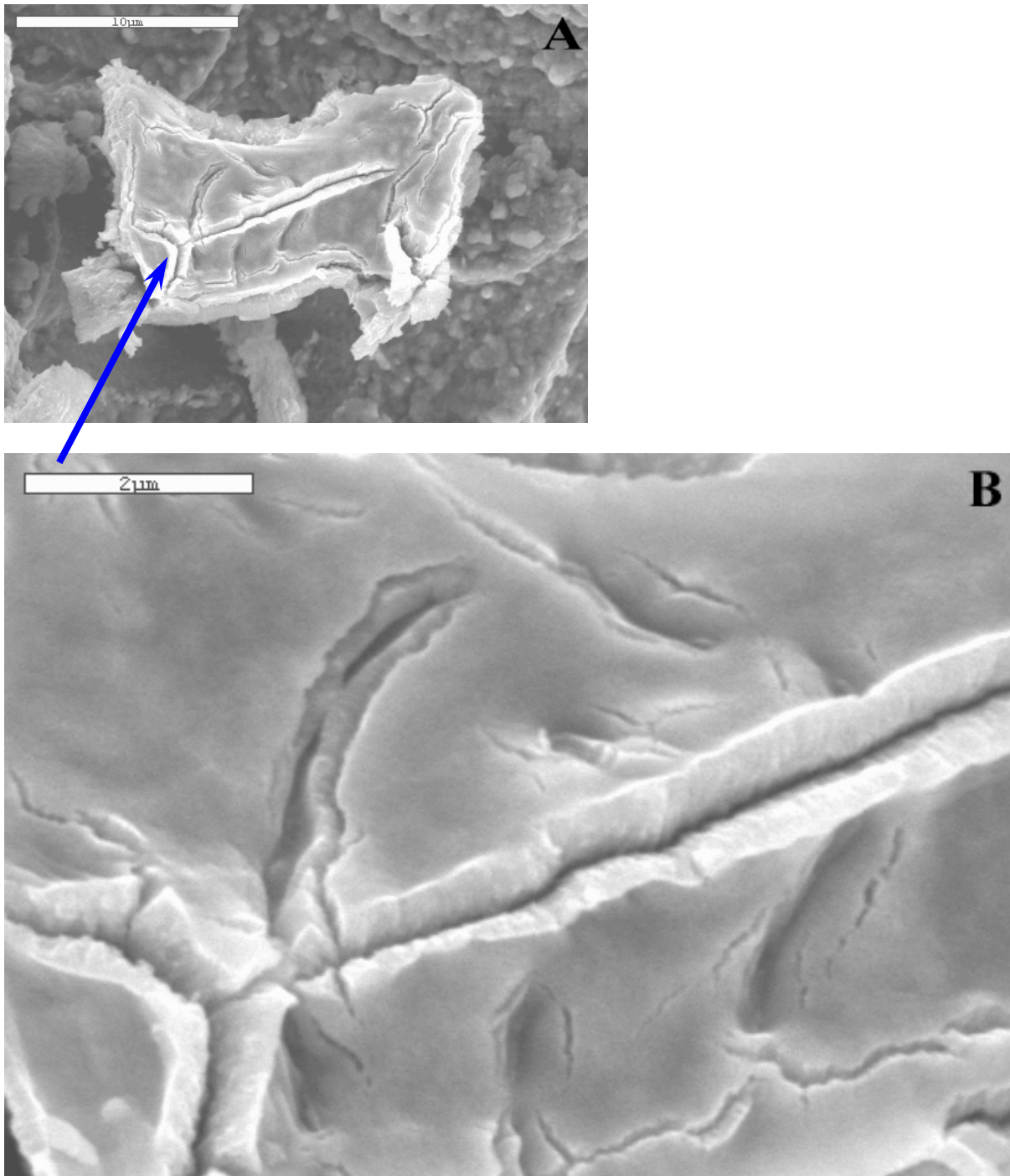


Figure 4-6. Carbide Face Crack Morphology (*43-1; Modification III*) at A) 5000x B) 15000x.

At higher magnification, the appearance of the cracks in the carbides is nearly identical to that of the edges of the carbides seen previously. Since these appear to become more prevalent

and widen as temperature increases, it can be concluded that the appearance is not strictly from original morphology alone after all.

This project is not a study of carbide morphology, and therefore further discussion is not warranted here. The subject is not one which is well-known as yet and while further investigation is certainly of interest, it diverges from the goal of the project. What is important for the purposes of these modified alloys and their properties is that the carbide morphology still seems to have little to do with the creep behavior exhibited by the alloys.

Cross-Section Analysis

While imaging of the fracture surfaces did not provide much in the way of explanation of the effect of the alloy modifications on the creep behavior, additional information was obtained by examining the cross-section of the fractured samples.

Optical Imaging

The first thing that was noted from the optical imaging process was that there were small differences between the residual dendritic structures of the alloys. This had been evident previously, but was of more importance here because of the impact upon the location and dispersion of carbides and casting porosity throughout the samples. The composite images generated from the optical imaging process showed the following general features:

- Some casting pores were evident throughout the gage section. In some cases, these appeared to be as large as about 40 – 50 μm in diameter, but most were smaller than this – more on the order of 10 μm , like those shown previously in Figure 3-27. As expected, these were dispersed in the interdendritic regions, as evidenced by the residual carbide structure.
- Many sub-surface cracks were evident. These were generally in a direction normal to the tensile axis, and they occurred frequently near the fracture surface itself. The concentration of these sub-surface cracks was generally centered around the fracture, rather than in the middle of the gage length. From this, it can be concluded that the fracture occurred on a path where the highest concentration of these sub-surface cracks developed, which did not always occur in the center of the gage section.

These general features are shown in Figures 4-7 through 4-9 (*below and following page*). The blue arrows designate casting porosity, while the orange arrows designate sub-surface cracks.

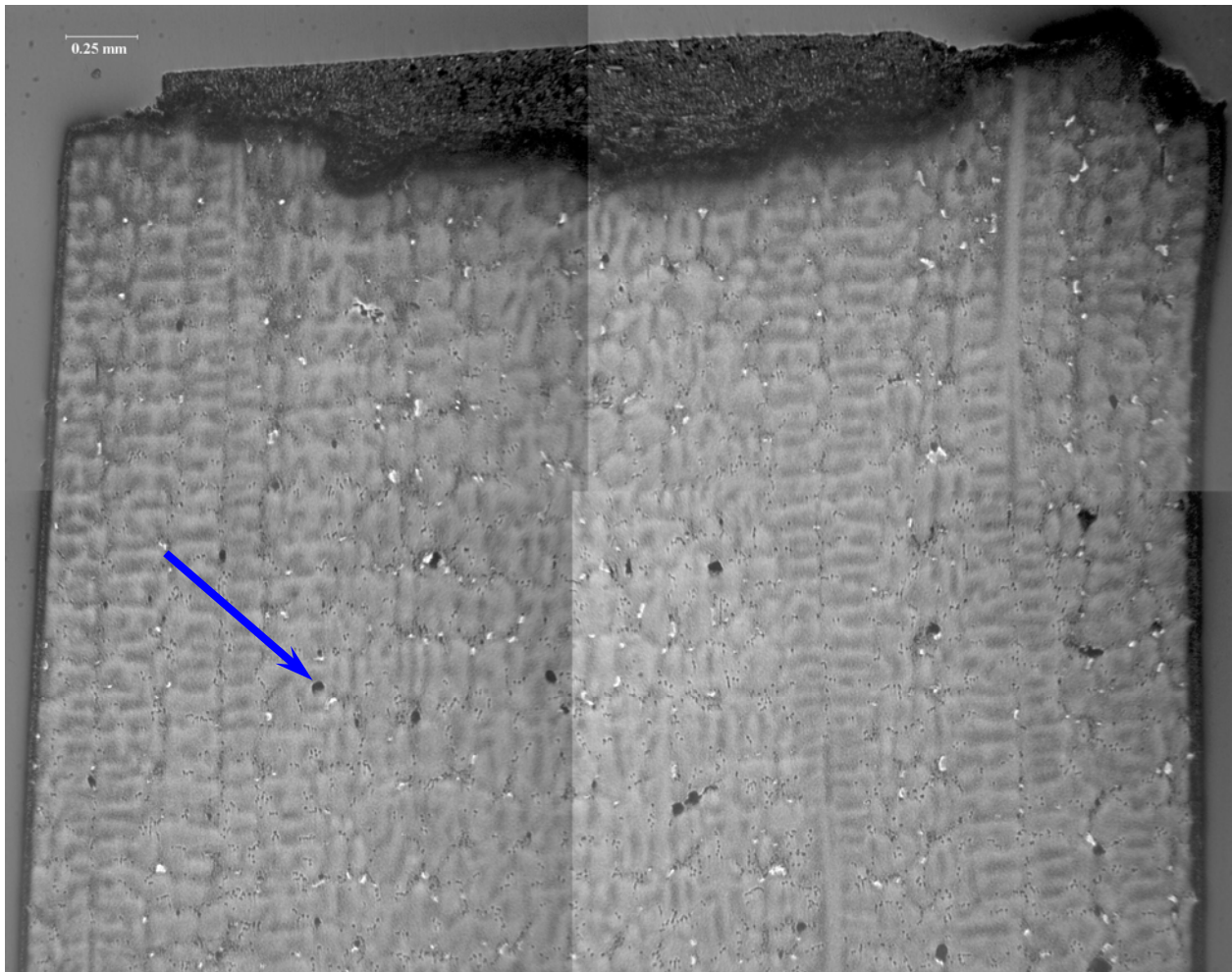


Figure 4-7. Composite Cross-Section of Creep Sample (*4-10A2; Baseline*).

The samples in Figures 4-7 through 4-9 were all examples of those tested at 750°C/831.5 MPa. It is important to note, however, that the similarity of the cross-sections may be a function of the damage required to cause failure under those conditions, rather than an indication of differences in how each alloy responds to them. However, it should be noted that these samples exhibited different rupture lifetimes and elongations in the process of failure.

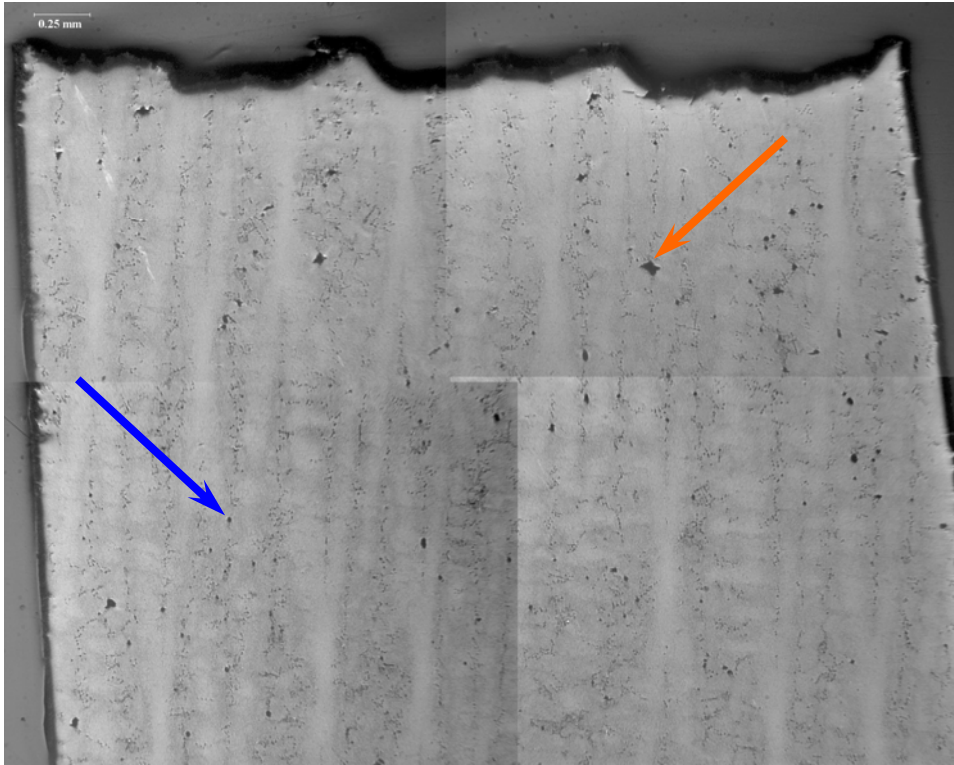


Figure 4-8. Composite Cross-Section of Creep Sample (23-2; *Modification II*).

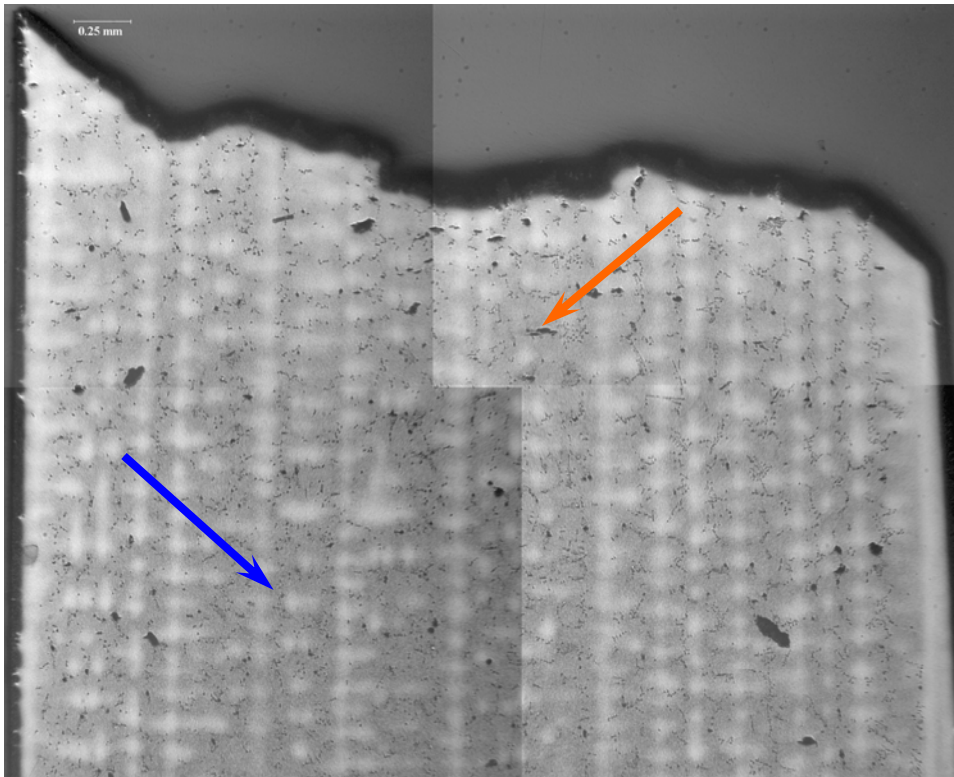


Figure 4-9. Composite Cross-Section of Creep Sample (39-2; *Modification III*).

In all three samples shown – along with the sample shown from the same set of conditions for the Modification I alloy in Figure 3-29 – there are some common features that can be noted. First, the degree of sub-surface cracking is not significant. Second, casting porosity is generally very small, usually appearing in small groups or a nearly-linear series of pores. These decorate the edges of the residual dendritic structure throughout the sample. This is difficult to see in Figures 4-7 through 4-9, so Figure 4-10 is provided (below) as a better example. The casting porosity is indicated by the blue arrow.

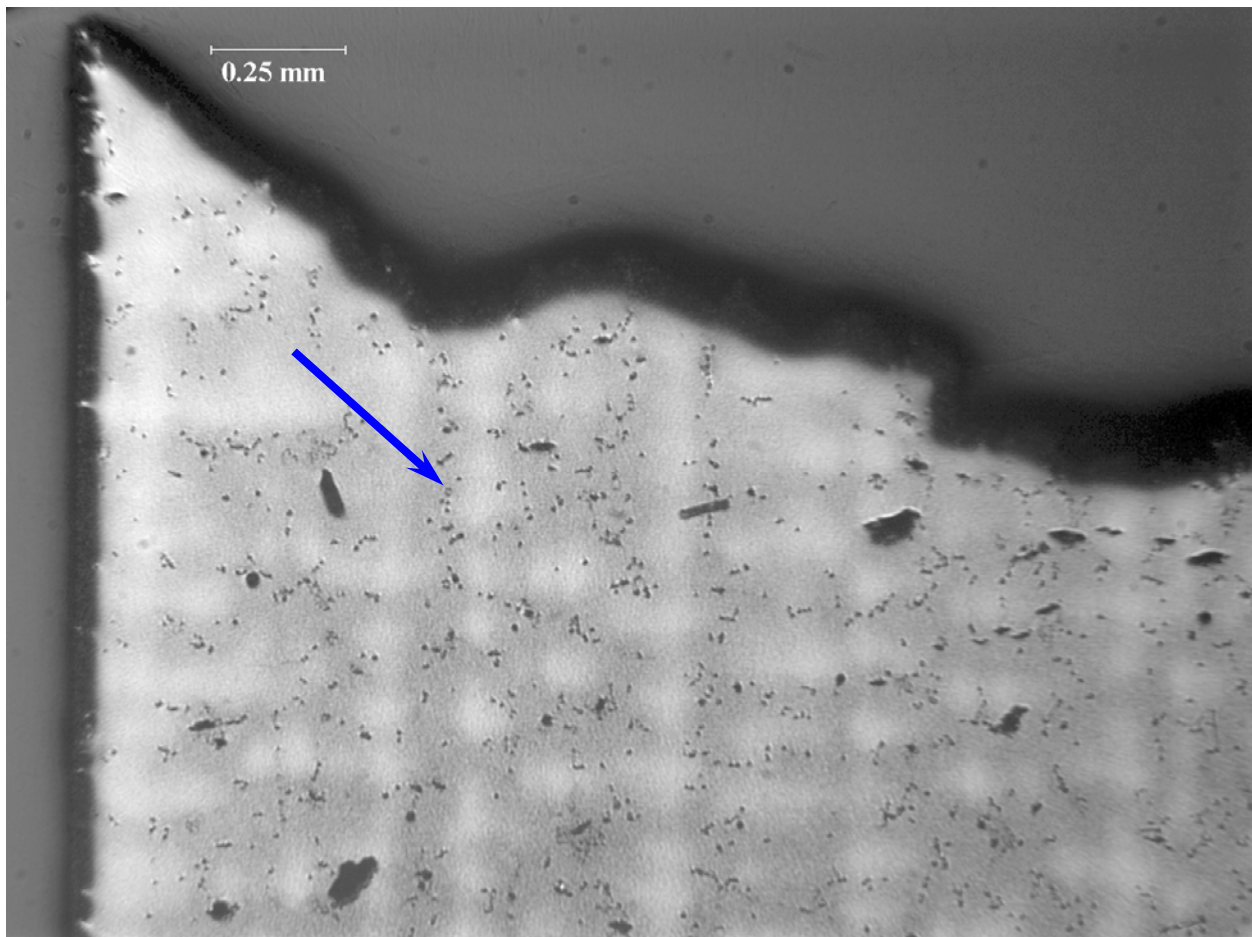


Figure 4-10. Cross-Section of Creep Sample (39-2; *Modification III*) – Upper Left Portion.

Under the 850°C/448.9 MPa and 950°C/344.5 MPa conditions, there was a significant amount of sub-surface cracking evident.

An example of a sample at each condition can be seen in Figures 4-11 and 4-12 (*below*).

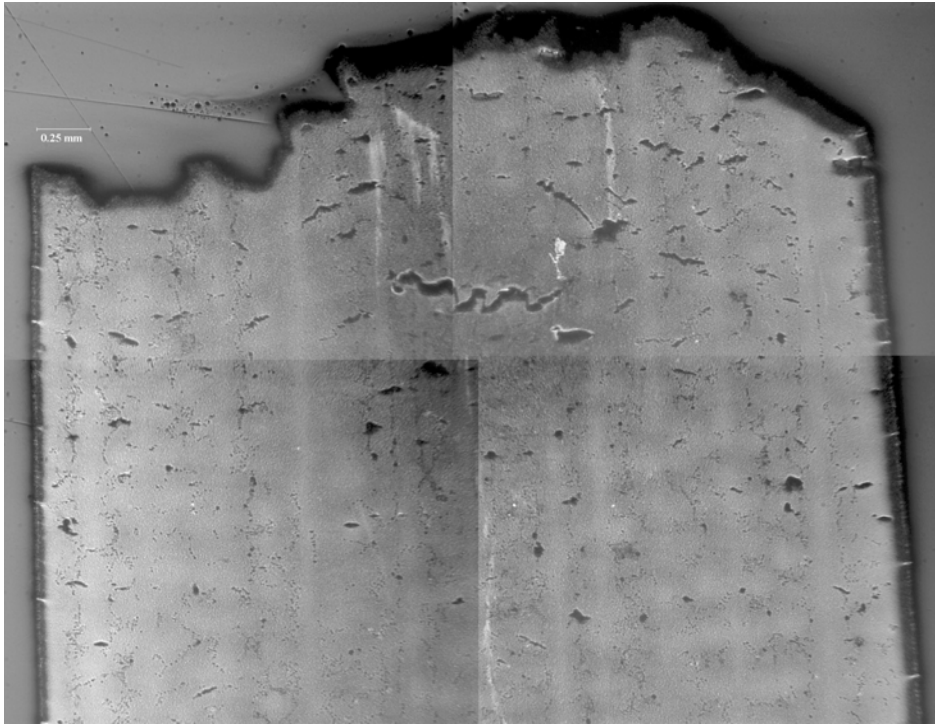


Figure 4-11. Composite Cross-Section of Creep Sample (*24-2; Modification II*).

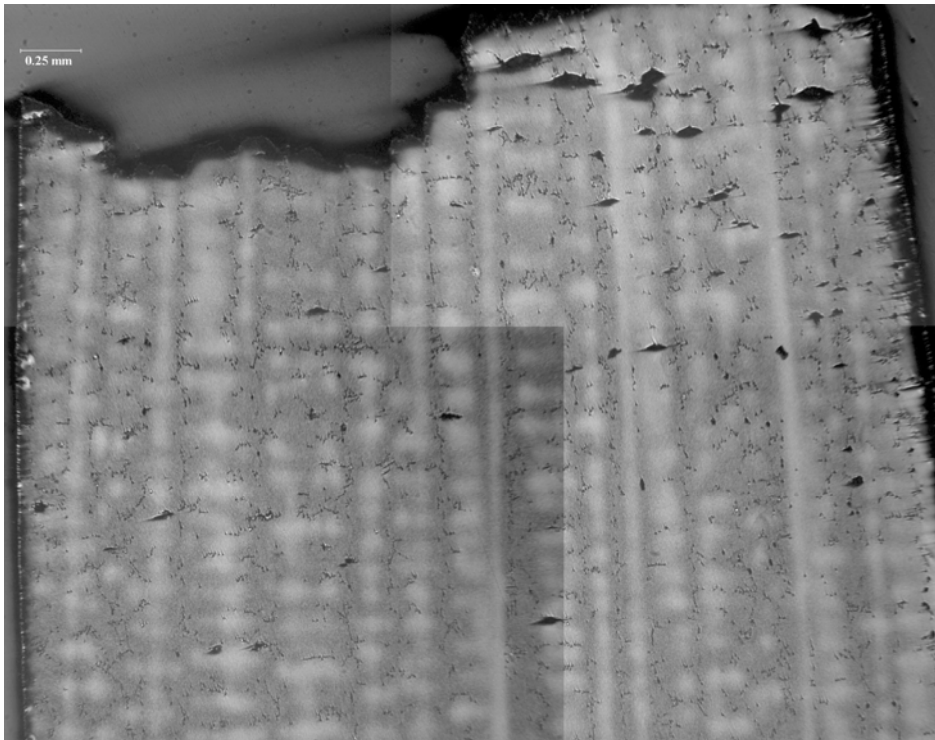


Figure 4-12. Composite Cross-Section of Creep Sample (*13-1; Modification I*).

Looking at these images, one might theorize that at the higher temperatures, the cracks formed throughout the material more rapidly than at lower temperatures. However, these last two samples exhibited similar amounts of sub-surface cracking, but they did so with very different rupture lifetimes. The sample shown in Figure 4-11 failed in 327 hours, whereas the one shown in Figure 4-12 failed in only 13.9 hours. Therefore, neither crack propagation rates nor the microstructures which appear in these optical images can provide a definitive answer on the role of casting porosity and carbides on the fracture process.

SEM Imaging

Since the resolution available on the optical microscope did not afford the opportunity to show the possible differences in microstructure that were affecting the creep behavior of the samples, SEM techniques were applied. As a reminder, the images were taken at various magnifications on each sample as shown in Figure 4-13 (*below*):

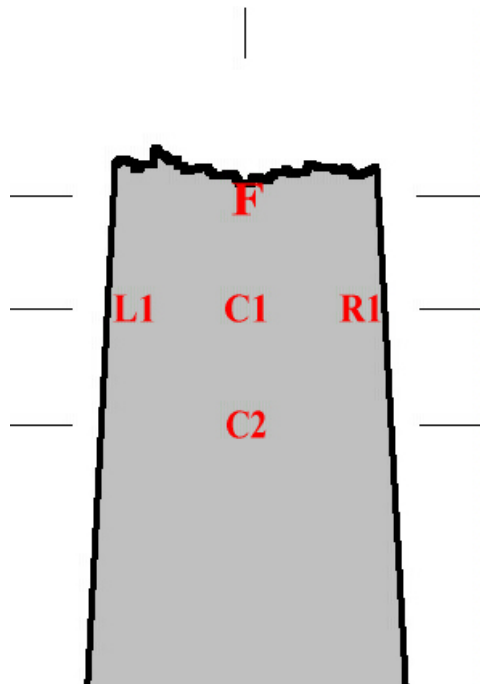


Figure 4-13. Imaging Points for SEM Analysis of Cross-Section Samples.

A set of images was taken at 200x just below the fracture surface, but these were comparable to the composite images generated in the optical imaging analysis and provided only a limited amount of additional information. The only real difference between optical and electron imaging was that the small increase in magnification allowed the carbides to be more clearly identified. The SEM images taken at 1000x provided views of cracks and carbides in much better detail than in the optical or 200x SEM images, but only just barely started to resolve the γ/γ' microstructure. The images taken at 2500x and 5000x were of great value, and will be used throughout the remainder of the discussion. Some EDS spectra were also taken for a few of the carbides seen on the surface, as well as one to analyze the composition of the very small amount of γ/γ' eutectic which remained even after solutioning. The compositions measured for these phases were similar to previous results in this study.

One point which should be made here is that the use of a limit of a 2mm distance from the fracture surface was based upon the observation that further away from the fracture surface, hardly any sub-surface cracks were noted. In fact, quite often these cracks were not found further than 1mm from the fracture surface. It was thought that comparison between microstructures at these locations might provide the best correlation between the crack locations and the behavior exhibited by the alloys.

That having been said, there was no discernable difference in the γ/γ' microstructure compared at any two points on the same sample – neither in size, shape nor orientation. The only evidence of differences in this microstructure were those of the γ' shape between samples – with the Baseline and Modification II samples having irregular/rectangular γ' , the Modification I samples having spherical γ' and the Modification III samples having cuboidal γ' . An example of this difference is shown in Figures 4-14 and 4-15 (*below*). These images are both from the C2

points so as to avoid any possible impact of anomalies from the fracture misrepresenting the actual structure in either. The spherical shape of the γ' in the Modification I alloy and the irregular/rectangular shape of the γ' in the Baseline and Modification II alloys are evident.

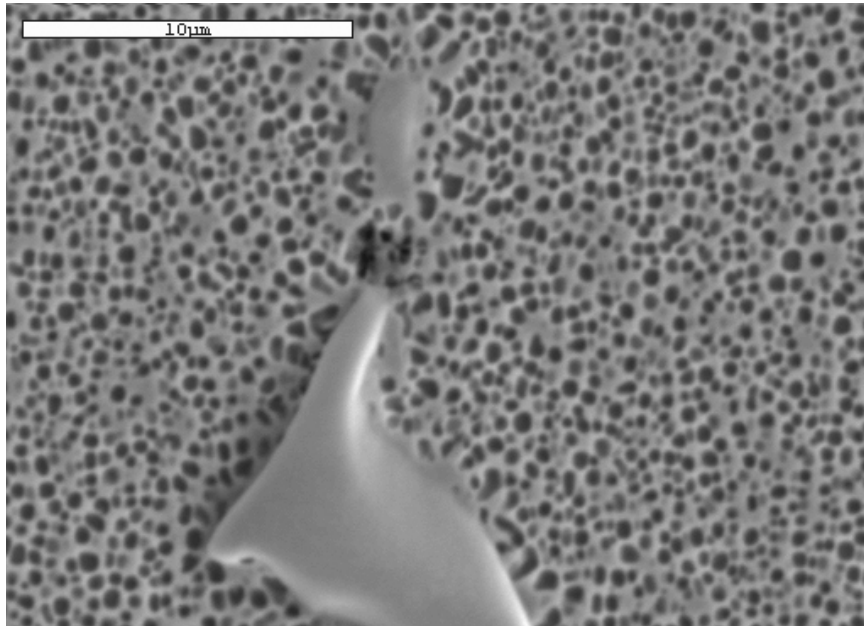


Figure 4-14. **C2** Image Point of Creep Sample Cross Section (7-1; *Modification I*) at 5000x.

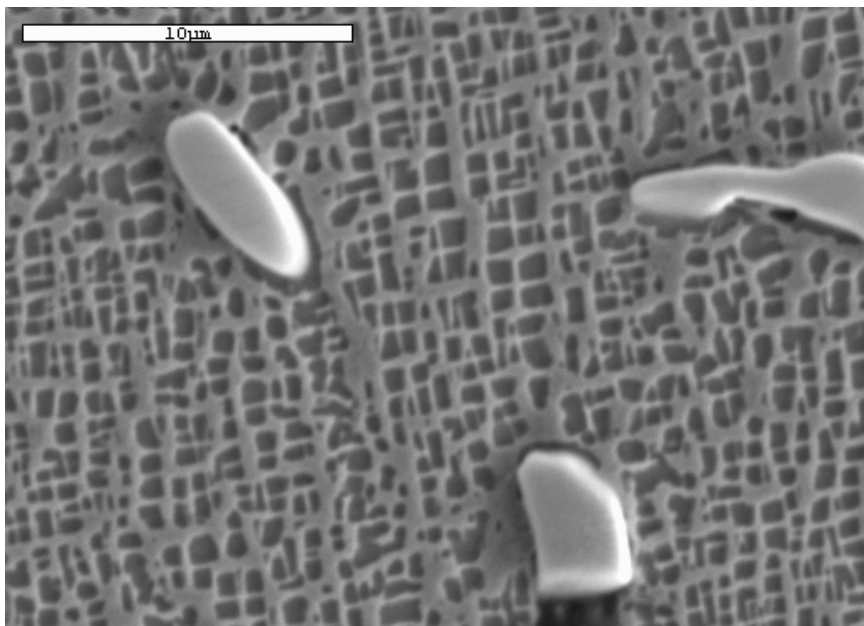


Figure 4-15. **C2** Image Point of Creep Sample Cross Section (23-2; *Modification II*) at 5000x.

The difference in γ' morphology is significant in terms of mechanical properties. It has been known for some time that alloys with cuboidal γ' morphology have improved strength properties over those with spherical γ' morphology [30]. The cuboidal structure is typical of Re-bearing alloys, and this has been of key importance in the development of second- and now third-generation Ni-based superalloys. This morphology is affected by composition, and the misfit between the γ matrix and γ' precipitates, which is described by the following equation:

$$\delta = 2 \left(\frac{a_{\gamma'} - a_{\gamma}}{a_{\gamma'} + a_{\gamma}} \right)$$

where δ is the γ/γ' misfit and a_{γ} and $a_{\gamma'}$ are the lattice parameters of the γ matrix and γ' precipitates (respectively).

The importance of this misfit is described in the following manner [8,9]: in order to minimize interfacial energy, coarsening of the γ' precipitates occurs, with a concurrent change from spherical to cuboidal geometry. As shown in Figures 4-14 and 4-15 – the largest spherical precipitates are approximately 0.5 μm whereas the smallest rectangular (irregular cuboidal) precipitates are approximately 1 μm in size. The size of the γ' precipitates observed in all samples was similar. The value of the misfit (negative or positive) can also affect the occurrence and direction of rafting of the γ' precipitates [31,32].

As stated previously, misfit is largely affected by compositional changes, and while Re addition is one method used to generate cuboidal γ' precipitates, it is not the only method. It was thought that the change in Al/Ti ratio and the increase in Ta content in the Modification I alloy would promote the cuboidal geometry of the γ' , but this was not the case, as evidenced by the microstructure seen in Figure 4-14.

There is another noticeable difference between the structures shown in Figures 4-14 and 4-15: the area around the carbide particles exhibits a less-orderly γ/γ' structure in the Modification II alloy. No such breakdown in the structure near the carbides was noted in the Modification I image, as the brick-wall structure continued up to the particle. This breakdown in the orderly γ/γ' structure near the carbides was noted in the Baseline, Modification II and Modification III alloys – those without the spherical γ' structure. It is not as pronounced in the Modification III alloy, which has a cuboidal γ' structure typical of Re-bearing alloys. For the 750°C tests, there was no obvious correlation between the strength of the alloys and the microstructural continuity near the carbides. However, for the 850°C and 950°C tests, there is a notable difference: Modification I exhibits more primary creep and a less-pronounced region of secondary creep than the other alloys. In some cases, the regions around carbides where the brick-wall structure became less regular seem to repel the propagation of the crack, as shown in Figure 4-16 (*below*).

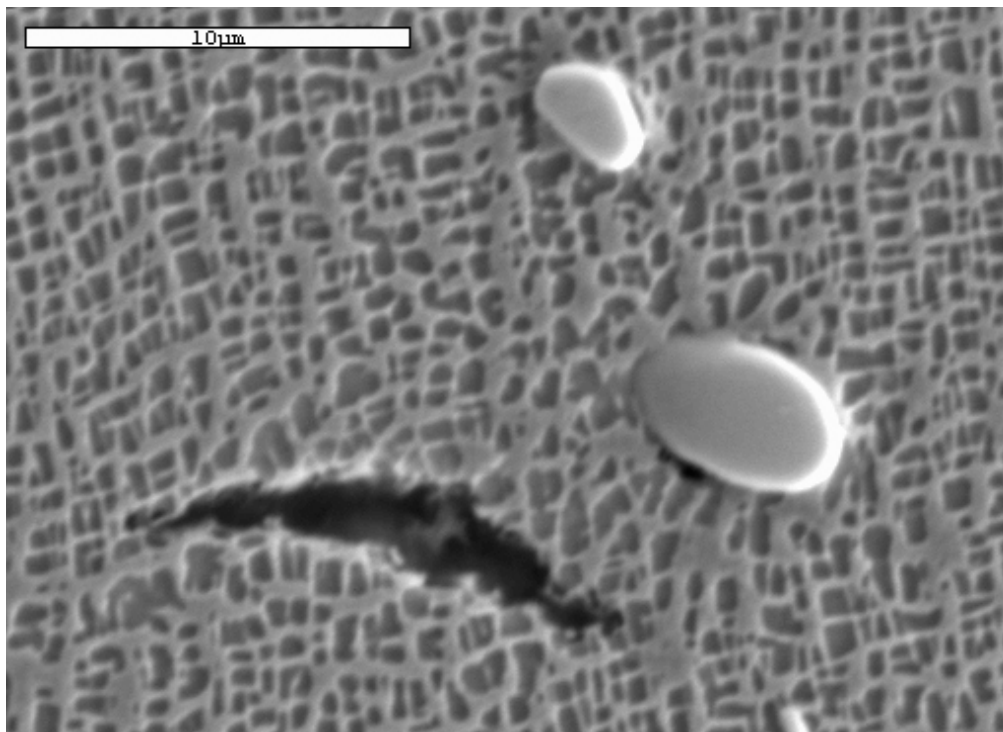


Figure 4-16. Crack Propagation around Irregularity in Brick-Wall γ/γ' Structure on Creep Sample Cross Section (23-2; *Modification II*) at 5000x.

In this example, the crack appears to propagate toward the carbide, but it is difficult to know what the 3D state of stress is in each area without further investigation. In most cases though, the cracks propagate right through to the particles.

As for propagation and initiation of cracks at these carbide particles, two different behaviors were observed. First, there were many examples of carbides which appeared to have been fractured by the proximity of a crack, or which initiated the crack themselves. An example of this is shown in Figure 4-17 (*below*), where it can be seen that the crack is clearly in the process of going through the carbide, identified by the blue arrow. In this image, it can also be seen that the cracks could easily propagate along the carbide-matrix interface as well.

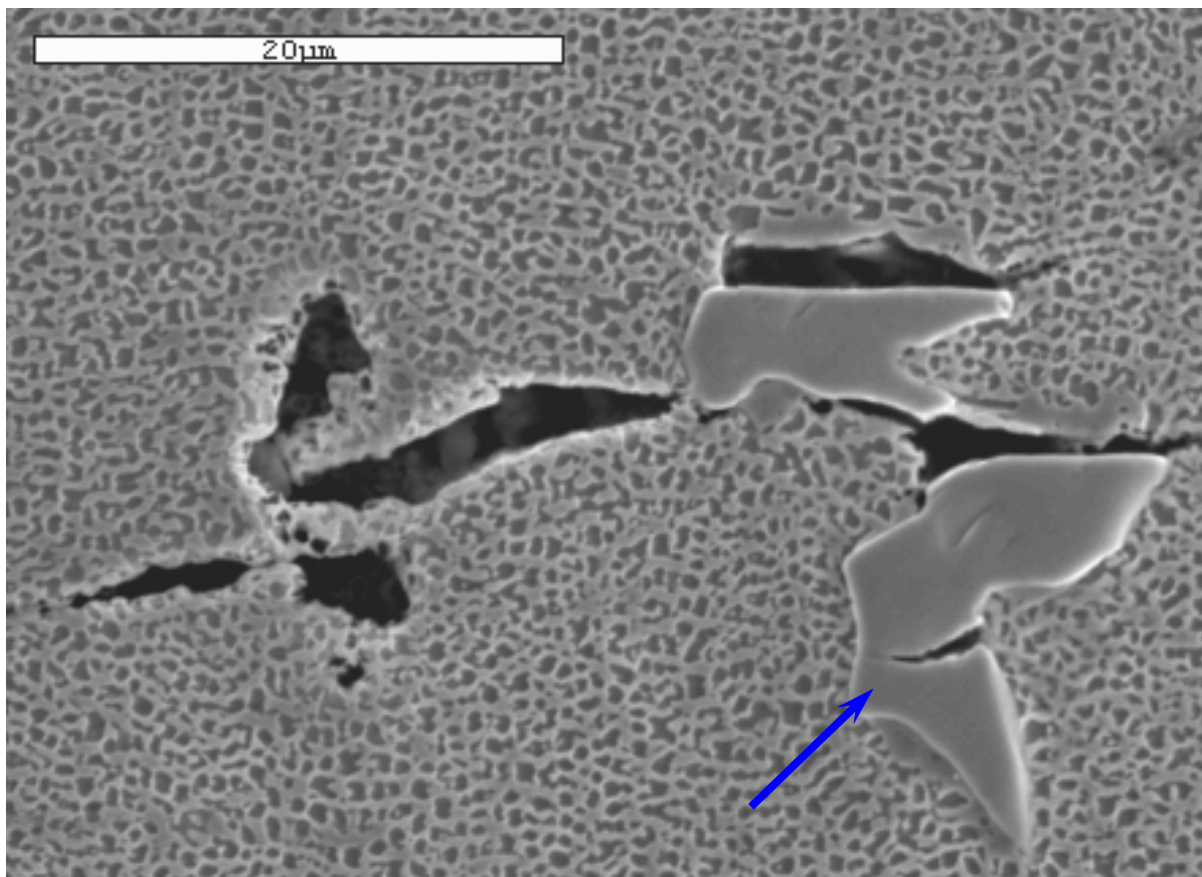


Figure 4-17. Crack Propagation on Creep Sample Cross Section (*43-1; Modification III*) at 2500x.

However, examples can be seen where the fracture of the carbide had no apparent impact upon the surrounding microstructure, such as those shown in Figure 4-18 (A-B) (*below*).

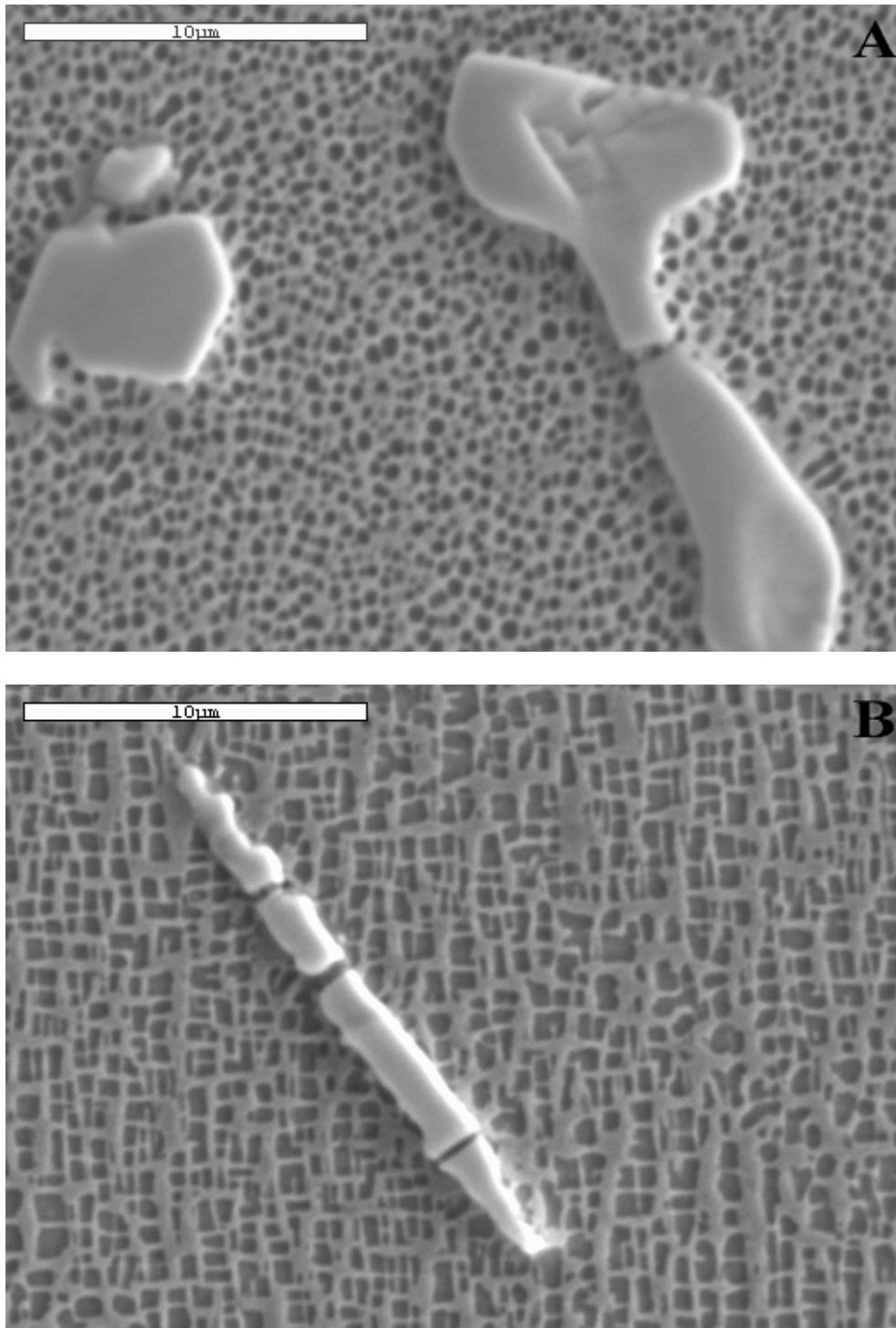


Figure 4-18. Cracks in Carbide Particles on Creep Sample Cross-Sections A) (7-1; *Modification I*) B) (25-2; *Modification II*).

Previously, it was noted that pores rarely appeared to affect the surrounding microstructure on the fracture surfaces. Evidence of this was even illustrated in Figures 3-26 and 3-27. However, images taken of the cross-sections of these samples suggest otherwise. The pores in Figures 4-19 and 4-20 (*below*) clearly serve as crack initiation sites and/or propagation sites.

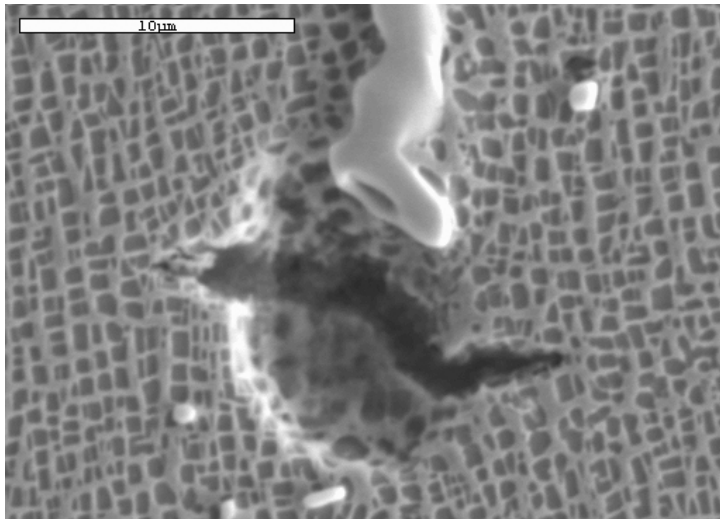


Figure 4-19. Cracks in Casting Pore on Creep Sample Cross Section (23-2; *Modification II*) at 5000x.

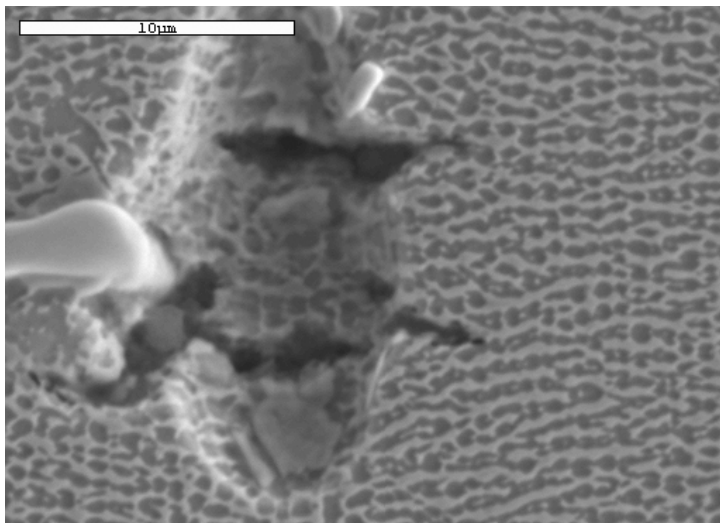


Figure 4-20. Cracks in Casting Pore on Creep Sample Cross Section (26-1; *Modification II*) at 5000x.

Based upon information in the literature [33], it is more likely that these are crack initiation sites. Sinha noted that the 3D stress state near certain detailed features on the surface of the pore

creates the conditions necessary for a crack to form and begin to propagate. The geometry of the cracks shown in Figures 4-19 and 4-20 exhibit similar features. While both of these images come from Modification II samples, this behavior was evident in all of the cross-sections analyzed except Modification I. The reasons for the differences between the Modification I and II alloys were not obvious.

However, as noted previously: the matrix surrounding the pores in the Modification I alloy exhibited a spherical γ' structure, whereas that of the remaining alloys all exhibited either irregular/rectangular or cuboidal γ' . In the latter structures, geometry alone suggests that high values of stress could exist at corners of the γ' precipitates, whereas in the spherical γ' , no such stress concentrators are present. This alone could possibly explain the behavior differences described earlier – where the Modified I alloy displayed more primary creep and a greatly reduced failure time under the same conditions at higher temperatures as the other alloys.

Detailed explanation of creep and the associated mechanisms has already been presented by many authors [11,13,14,19,34-36] and will not be reviewed here. It is not the purpose of this project to develop a full understanding of creep itself, but to formulate a foundation upon which it is possible to continue to develop an alloy appropriate for IGT applications.

What can also be seen in the microstructures of the samples shown in Figures 4-19 and 4-20 is the evolution of the γ' within the structure. This is also referred to as rafting, although what is seen in these two images is not complete rafting by any means. In both cases, it is evident that the cracks are propagating along the γ matrix, and going through the γ' which is not completely rafted. Examining other samples, a more developed rafting structure is noted, as shown in Figures 4-21 and 4-22 (*following page*):

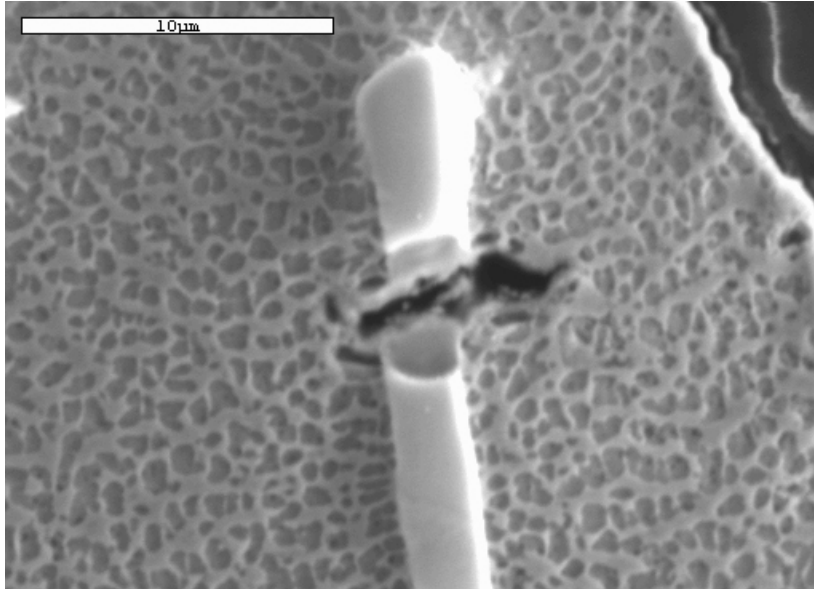


Figure 4-21. Partially Rafted Structure at **F** Image Point of Creep Sample Cross Section (4-10B2; *Baseline*) at 5000x.

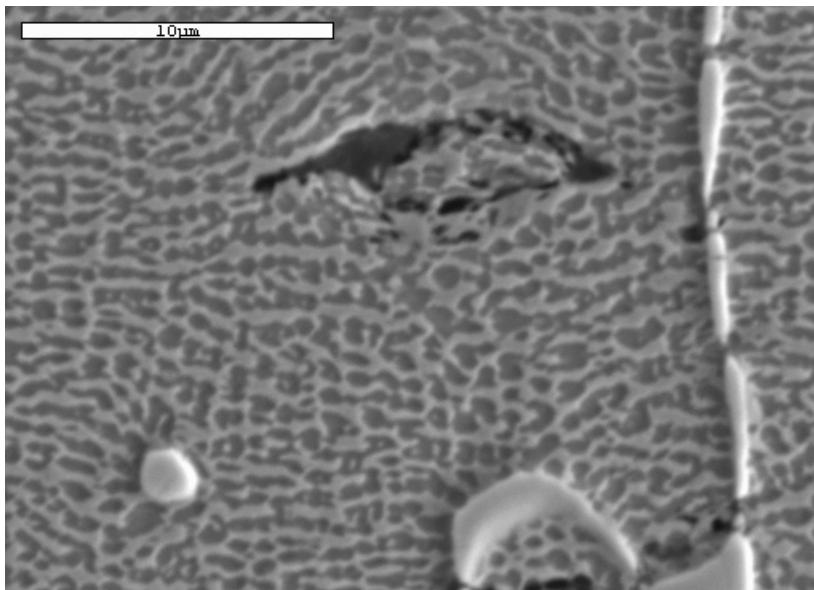


Figure 4-22. Partially Rafted Structure at **F** Image Point of Creep Sample Cross Section (26-1; *Modification II*) at 5000x.

Clearly, the rafted structure is not as fully developed in the Baseline sample, but this could be a function of not only its composition and misfit, but the fact that the exposure time was nearly double for the Modification II sample. However, the exposure time for both samples was relatively low (11.8 and 26.1 hours, respectively). It is known that rafting is a feature developed

as a result of temperature, applied stress and resultant strain [31,32], so a combination of these is probably represented better in samples which lasted longer. Microstructures of just such samples are seen in Figures 4-23 and 4-24 (*below*).

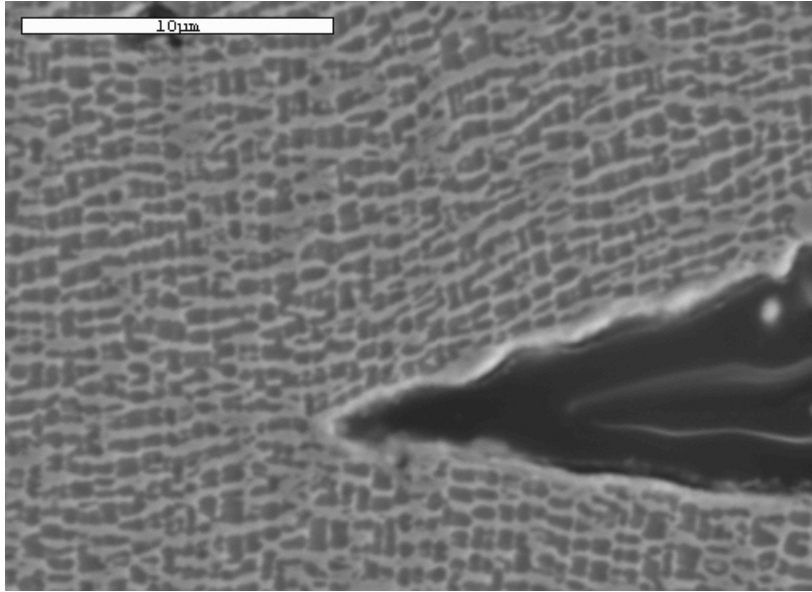


Figure 4-23. Partially Rafted Structure at **F** Image Point of Creep Sample Cross Section (24-2; *Modification II*) at 5000x.

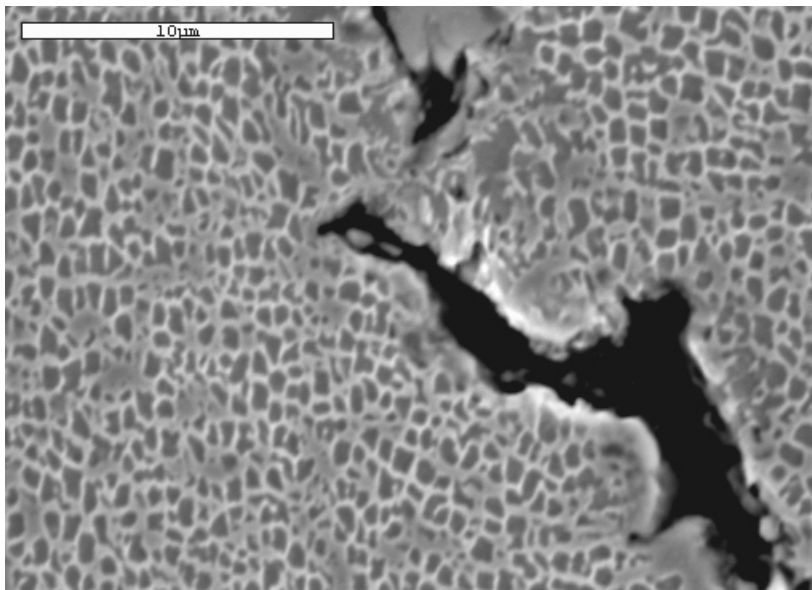


Figure 4-24. Structure at **F** Image Point of Creep Sample Cross Section (40-2; *Modification III*) at 5000x.

The samples shown in Figures 4-23 and 4-24 had rupture lifetimes of 327 hours and 801 hours (respectively) and the behaviors were otherwise very similar. From these images, the partially rafted structure in the Modification II alloy may be allowing cracks to propagate at a slightly higher rate than in the Modification III alloy, where there is no evidence that even the onset of rafting has occurred.

It is unknown exactly why this is the case, and there are many theories put forth in the available literature [32,37,38], but what seems clear is that the effect of the compositional changes made to develop the Modification III alloy have had a positive effect on suppressing the rafting process and this has led to the improvement of creep properties.

Conclusions

The purpose of this project was to investigate the possibility of strengthening PWA 1483 through alloying modifications. The following conclusions were made:

- Additions of γ' formers (Al, Ti, Ta) alone essentially destroyed the castability of the alloy, as evidenced by an 80% rejection rate. The mechanical properties of the alloy with these additions were often comparable at lower temperatures, but were significantly reduced at higher temperatures. Since this alloy is being developed for IGT application, this does not seem to be a viable alloying method.
- Additions of solid solution strengtheners (Re, W) with a concurrent increase in structural stabilizers (Co) proved to be a better method where casting was concerned. In addition, these proved to be more appropriate for the IGT application, as a marked improvement in creep properties was exhibited over that of the baseline alloy at higher temperatures. This was evidenced by a 3x increase in time to 1% elongation and a 2x increase in rupture life over the baseline alloy (averaged between 850°C and 950°C results).
- A combination of additions from the first two modifications proved to be roughly equal in castability to that of the second modification, but the creep properties of this modification were the best of all three, and significantly exceeded those of the baseline alloy in many cases. As compared to the baseline, this modification exhibited a 5x increase in time to 1% elongation and a 5x increase in rupture life (averaged between 850°C and 950°C results).

The process of evaluating the reasons for these conclusions involved the mechanical tests themselves (tensile testing and creep testing) and imaging, which utilized both optical microscopy as well as scanning electron microscopy techniques.

Based upon these evaluations, the following observations were made:

- All fracture surfaces – from both tensile and creep tests – were of mixed character deformation. The tensile samples were dominated by cleavage-type fracture, while the creep samples were dominated by quasi-cleavage type fracture.
- All fracture surfaces exhibited the presence of two different morphologies of carbides: flowery carbides, so named for their petal-like appearance, and script carbides. All of these carbides were of MC type only. No TCP phases were observed in any sample.
- Carbide composition was universally rich in Ti and Ta, while the surrounding matrix was rich in Ni, Ta, Cr, Co and Ti.
- Creep sample damage exists as sub-surface cracks, which seem to have a gradient nature centered around the fracture surface. This gradient is almost fully dissipated approximately 2mm from the fracture surface. Samples tested at lower temperatures had significantly fewer sub-surface cracks than those tested at higher temperatures.
- Casting porosity is observed in all samples. Size is sometimes up to about 50 μm in diameter, but most are in the 5-10 μm range. These decorate the interdendritic regions, which are seen even after solutioning as a result of residual carbides.
- The microstructure of the first modified alloy was made up of spherical γ' . This is consistent with the shape seen in other Re-free alloys. The microstructure of the second modified alloy consisted of irregular/rectangular γ' . The microstructure of the third modified alloy consisted of cuboidal γ' .
- Partially rafted structures were evident in those alloys with irregular/rectangular γ' (baseline and second modification). No such structures were seen in the other alloys.

From these observations two further conclusions were made:

- Existence of these carbides in clusters is believed to be a fracture initiation site, as many were observed in the regions adjacent to cleavage facets. Single carbides can act as either a fracture initiation site as well as a propagation site. Cleavage of carbides only occurs at lower temperatures. Cracks propagate around carbides at high temperatures.
- Something about the composition in the third modified alloy resulted in a suppression of the rafting process, and this led to the improvement of creep properties.

Future Work

This project is certainly to be considered a first step in the process of developing an improved version of PWA 1483 for IGT applications. It has been proven here that at least two alloying methods work to improve the strength of the alloy. The future work implied by that statement alone is that perhaps there are more methods to improve strength. Even if these were the only two alloying methods which improved the alloy, a deeper investigation as to why these had the effects they did is merited, along with a study to see if these additions can be refined, to improve upon the strength even further. Such investigation would almost certainly involve the use of transmission electron microscopy (TEM) techniques, which could answer questions as to the role of dislocation density in the deformation mechanism seen here.

But, there is also the matter which must be studied to effectively close out this portion of the project. To do this, a study on the corrosion resistance of the modified alloys is warranted, and it would only be prudent to take this step prior to further efforts to refine or change the alloying content.

At the same time, it would be recommended to perhaps run a few more samples on these modifications. While the results contained in this document are certainly promising, it is also understood that the data was developed through testing of very few samples – so few, in fact, that the data itself almost demands that it be confirmed with more testing. Once these results have been made statistically relevant with a higher confidence level, the work suggested above could begin.

LIST OF REFERENCES

- [1] National Business Aviation Association, Principles of Aeronautics, Aeronautics Internet Textbook, Web Hosting by The National Business Aviation Association, <http://wings.avkids.com/Book/Propulsion/Images/trbfan.jpg>, last accessed on February 8, 2007.
- [2] R. Viswanathan and S.T. Sheirer, Materials Technology for Advanced Land Based Gas Turbines, EPRI Technical Report, 2003.
- [3] M. Konter and M. Thumann, Materials and Manufacturing of Advanced Industrial Gas Turbine Components, Journal of Materials Processing Technology, 117, 2001, pp. 386-390.
- [4] R.H. Badgley, GE LM2500 Gas Turbine, <http://emcon-systems.com//images/GE.LM2500.Gas.Turbine.jpg>, last accessed on February 8, 2007.
- [5] I. Gökalp and E. Lebas, Alternative Fuels for Industrial Gas Turbines (AFTUR), Applied Thermal Engineering, 24, 2004, pp. 1655-1663.
- [6] G.L. Juste, Hydrogen Injection as Additional Fuel in Gas Turbine Combustor: Evaluation of Effects, International Journal of Hydrogen Energy, 31, 2006, pp. 2112-2121.
- [7] K.W. Beebe, K.D. Cairns, V.K. Pareek, S.G. Nickolas, J.C. Schlatter and T. Tsuchiya, Development of Catalytic Combustion Technology for Single-Digit Emissions from Industrial Gas Turbines, Catalysis Today, 59, 2000, pp. 95-115.
- [8] R. Bowman, Superalloys: A Primer and History, Supplement to TMS Site Dedicated to the 9th International Symposium on Superalloys, <http://www.tms.org/Meetings/Specialty/Superalloys2000/SuperalloysHistory.html>, last accessed on February 8, 2007.
- [9] H.K.D.H. Bhadeshia, Nickel Based Superalloys, <http://www.msm.cam.ac.uk/phase-trans/2003/Superalloys/superalloys.html>, last accessed on February 8, 2007.
- [10] N.S. Stoloff, Wrought and P/M Superalloys, ASM Handbook, 1, ASM International, Metals Park, Ohio, 2003.
- [11] R.C. Reed, The Superalloys: Fundamentals and Applications, Cambridge University Press, London, 2006.
- [12] C.R. Brooks, Heat Treatment, Structure and Properties of Nonferrous Alloys, ASM, Metals Park, Ohio, 1982.

- [13] G.E. Dieter, *Mechanical Metallurgy*, 3rd Edition, McGraw-Hill, Boston, Massachusetts, 1986.
- [14] M.J. Donachie and S.J. Donachie, *Superalloys*, ASM Metals Handbook, Materials Park, Ohio, 2002.
- [15] Y. Jinjiang, S. Xiaofeng, J. Tao, Z. Nairen, G. Hengrong and H. Zhuangqi, *Effect of Re on Deformation and Slip Systems of a Ni-Base Single Crystal Superalloy*, *Materials Science and Engineering A*, 2006.
- [16] L.R. Liu, T. Jin, N.R. Zhao, Z.H. Wang, X.F. Sun, H.R. Guan and Z.Q. Hu, *Effect of Carbon Addition on the Creep Properties in a Ni-Based Single Crystal Superalloy*, *Materials Science and Engineering A*, 385, 2004, pp. 105-112.
- [17] S. Wollmer, T. Mack and U. Glatzel, *Influence of Tungsten and Rhenium Concentration on Creep Properties of a Second Generation Superalloy*, *Materials Science and Engineering A*, 319-321, 2001, pp. 792-795.
- [18] K. Harris, G.L. Erickson, and R.E. Schwer, *Directionally Solidified and Single-Crystal Superalloys*, ASM Handbook, 1, ASM-International, Materials Park, Ohio, 2002.
- [19] *Creep and Stress Rupture Failures*, ASM Handbook, 11, ASM-International, Materials Park, Ohio, 2003.
- [20] S. Tin and T.M. Pollock, *Phase Instabilities and Carbon Additions in Single-Crystal Nickel-Base Superalloys*, *Materials Science and Engineering A*, 348, 2003, pp. 111-121.
- [21] A.R. Price and B.A. Mueller, *Advances in Casting Large Single Crystal Components for Industrial Gas Turbines*, 1999 TMS-AIME Fall Meeting, Cincinnati, Ohio, November 11, 1999.
- [22] K.A. Al-Jarba and G.E. Fuchs, *Effect of Carbon Additions on the As-Cast Microstructure and Defect Formation of a Single Crystal Ni-Based Superalloy*, *Materials Science and Engineering A*, 373, 2004, pp. 255-267.
- [23] L.J. Grant and E.A. Sidwell, *Modification of PWA 1483 for IGT Applications*, unpublished research report, University of Florida, Gainesville, Florida, 2005.
- [24] D.M. Shah and A. Cetel, *Evaluation of PWA 1483 for Large Single Crystal IGT Blade Applications*, *Superalloys 2000*, eds. T.M. Pollock, R.D. Kissinger, R.R. Bowman, K.A. Green, M. McLean, S. Olson and J.J. Schirra, TMS, 2000, pp. 295-304.

- [25] G.E. Fuchs and B.A. Boutwell, Modeling of the Partitioning and Phase Transformation Temperatures of an As-Cast Third Generation Single Crystal Ni-Base Superalloy, *Materials Science and Engineering A*, 333, 2002, pp. 72-79.
- [26] E.C. Caldwell, A New Method for the Modeling of Elemental Segregation Behavior and Partitioning in Single Crystal Nickel Base Superalloys, Master's Thesis, University of Florida, Gainesville, Florida, 2004.
- [27] J.T. Guo, K.W. Huai, Q.Gao, W.L. Ren and G.S. Li, Effects of Rare Earth Elements on the Microstructure and Mechanical Properties of NiAl-Based Eutectic Alloy, *Intermetallics*, 2006, pp. 1-7.
- [28] V. Kerlins, Modes of Fracture, *ASM Handbook*, 12, ASM-International, Materials Park, Ohio, 2002.
- [29] M. Marx and H. Vehoff, Propagation of Microcracks in Single Crystalline Nickel-Based Superalloys: Size Effects on the Crack Opening, *Materials Science and Engineering A*, 387-389, 2004, pp. 511-515.
- [30] A.D. Cetel and D.N. Duhl, Second Generation Nickel-Base Single Crystal Superalloy, Sixth International Symposium on Superalloys, Seven Springs, Pennsylvania, TMS, 1988, pp. 235-244.
- [31] N. Ratel, G. Bruno, P. Bastie, T. Mori, Plastic Strain-Induced Rafting of γ' Precipitates in Ni Superalloys: Elasticity Analysis, *Acta Materialia*, 54, 2006, pp. 5087-5093.
- [32] M. Kamaraj, Rafting in Single Crystal Nickel-Base Superalloys – An Overview, *Sādhanā*, 28, Parts 1 & 2, February/April 2003, pp. 115–128.
- [33] N. Sinha, Constant-Load Tertiary Creep in Nickel-Base Single Crystal Superalloys, *Materials Science and Engineering A*, 432, 2006, pp. 129-141.
- [34] R. Reed-Hill and R. Abbaschian, *Physical Metallurgy Principles*, 3rd Edition, PWS Publishing, Boston, Massachusetts, 1984.
- [35] M.V. Acharya and G.E. Fuchs, The Effect of Stress on the Microstructural Stability of CMSX-10 Single Crystal Ni-Base Superalloys, *Scripta Materialia*, 54, 2006, pp. 61-64.
- [36] C.M.F. Rae and R.C. Reed, Primary Creep in Single Crystal Superalloys: Origins, Mechanisms and Effects, *Acta Materialia*, 55, 2007, pp. 1067-1081.
- [37] T. Ichitsubo, S. Koumoto, M. Hirao, K. Tanaka, M. Osawa, T. Yokokawa and H. Harada, Rafting Mechanism for Ni-Base Superalloy under External Stress: Elastic or Elastic-Plastic Phenomena? *Acta Materialia*, 51, 2003, pp. 4033-4044.

- [38] R.C. Reed, D.C. Cox and C.M.F. Rae, Damage Accumulation During Creep Deformation of a Single Crystal Superalloy at 1150°C, *Materials Science and Engineering A*, 2006.

BIOGRAPHICAL SKETCH

Brendan C. Collins was born in August 1970 in Wheat Ridge, CO – a suburb of Denver. He graduated from Torrey Pines High School in San Diego, CA in June 1989, having also completed a semester of study abroad at the University of Paris (Sorbonne) during the summer of 1987. Upon graduation from high school, he began a 12-year career in the United States Navy. In completing the Naval Nuclear Power Training Pipeline, he earned the certification of Mechanical Operator for Naval nuclear power plants. He subsequently attended Naval Nuclear Operator Welder school, where he was certified in several different welding, brazing and cutting techniques. Having served as an operator on a ballistic missile submarine, an instructor at the Naval Nuclear Power Training Unit – where he was certified Master Training Specialist – and as an engine room supervisor on a fast attack submarine, he was granted an Honorable Discharge with the final rank of MM1/SS. He immediately enrolled as an undergraduate at the University of Florida in the Department of Materials Science & Engineering. He graduated with his Bachelor of Science degree in this department in April 2005, having completed the curriculum under the Metals discipline. He was then selected by the NASA-USRP for an internship at Los Alamos National Laboratory, which he completed in the summer of 2005. In August 2005, he returned to the University of Florida to pursue advanced education in the field of materials science & engineering. He is currently scheduled to graduate having earned a Master of Science degree in May 2007 and he will begin working for the Nuclear Regulatory Commission in Atlanta, GA shortly thereafter.